SANDIA REPORT
SAND2012-7998
Unlimited Release
Printed September 2012

X-Ray Thomson Scattering Measurements of Warm Dense Matter

James E. Bailey, Tommy Ao, Eric Harding, Stephanie B. Hansen, Michael P. Desjarlais, Raymond W. Lemke, Gregory A. Rochau, Joe Reneker, Dustin Romero

Prepared by
Sandia National Laboratories
Albuquerque, New Mexico 87185 and Livermore, California 94550

Sandia National Laboratories is a multi-program laboratory managed and operated by Sandia Corporation, a wholly owned subsidiary of Lockheed Martin Corporation, for the U.S. Department of Energy's National Nuclear Security Administration under contract DE-AC04-94AL85000.

Issued by Sandia National Laboratories, operated for the United States Department of Energy by Sandia Corporation.

Available to DOE and DOE contractors from
U.S. Department of Energy
Office of Scientific and Technical Information
P.O. Box 62
Oak Ridge, TN 37831

Telephone: (865) 576-8401
Facsimile: (865) 576-5728
E-Mail: reports@adonis.osti.gov
Online ordering: http://www.osti.gov/bridge

Available to the public from
U.S. Department of Commerce
National Technical Information Service
5285 Port Royal Rd.
Springfield, VA 22161

Telephone: (800) 553-6847
Facsimile: (703) 605-6900
E-Mail: orders@ntis.fedworld.gov
Online order: http://www.ntis.gov/help/ordermethods.asp?loc=7-4-0#online

SAND2012-7998
Unlimited Release
Printed September 2012

X-Ray Thomson Scattering Measurements of Warm Dense Matter

James E. Bailey, Tommy Ao, Eric Harding, Stephanie B. Hansen, Michael P. Desjarlais, Raymond W. Lemke, Gregory A. Rochau, Joe Reneker, Dustin Romero

Department Names
Sandia National Laboratories
P.O. Box 5800
Albuquerque, New Mexico 87185-MS1196

Abstract

Warm dense matter exists at the boundary between traditional condensed matter and plasma physics and poses significant challenges to theoretical understanding. It is also critical for applications, including z-pinch and inertial fusion laboratory experiments and in astrophysical objects such as white dwarfs and giant planet interiors. The modern generation of high energy density facilities has made it possible to create warm dense conditions in the laboratory. Creating warm dense matter is challenging, but thorough understanding also requires accurate detailed diagnostics. This report describes research aimed at combining x-ray Thomson scattering, a powerful diagnostic for warm dense matter, with extreme environments created at the Z facility. Significant advances in in-house Sandia capability have been achieved, including x-ray scattering theory, instrumentation, and experiment design, execution, and interpretation. This work has set the stage for novel x-ray scattering investigations of warm dense matter at the Z facility in the near future.

ACKNOWLEDGMENTS

The Authors acknowledge invaluable assistance by Prof. Gianluca Gregori, Oxford University.

CONTENTS

FIGURES

TABLES

NOMENCLATURE

DOE	Department of Energy
SNL	Sandia National Laboratories
LDRD	Laboratory Directed Research & Development
WDM	Warm Dense Matter
HEDP	High Energy Density Physics
ICF	Inertial Confinement Fusion
XRTS	X-Ray Thomson Scattering
Z	Z-accelerator
ZBL	Z Beamlet Laser
MHD	Magnetohydrodynamics
ALEGRA	Arbitrary Lagrangian-Eulerian Multimaterial Multiphysics Code
MITL	Magnetically Insulated Transmission Line
AK	Anode-Cathode
FSSR	Focusing Spectrometer with Spatial Resolution
XRS^3	X-ray Scattering Spherical Spectrometer
IP	Image Plate
HOPG	Highly Oriented Pyrolytic Graphite
HAPG	Highly Annealed Pyrolytic Graphite
PSL	Photo-Stimulated Luminesce
FWHM	Full-Width-Half-Max
DMP	Dynamic Material Properties
CRF	Carbon Resorcinol Formaldehyde
VISAR	Velocimetry Interferometer System for Any Reflector
SVS	Streak Visible Spectroscopy
FOA	Final Optical Assembly
LOS	Line-of-Sight
FOV	Field-of-View
EOS	Equation-of-State

This page intentionally left blank.

1. INTRODUCTION

1.1. Warm Dense Matter

Warm dense matter exists at the boundary between traditional condensed matter and plasma physics and poses significant challenges to theoretical understanding [1]. It is also critical for applications, including z-pinch [2] and inertial fusion laboratory experiments [3] and in astrophysical objects such as white dwarfs and giant planet interiors [4, 5]. The modern generation of high energy density facilities has made it possible to create warm dense conditions in the laboratory [6-10]. Creating warm dense matter is challenging, but thorough understanding also requires accurate detailed diagnostics. This project was designed to advance warm dense matter physics by combining x-ray Thomson scattering, a powerful diagnostic for warm dense matter, with extreme environments created at the Z facility. X-ray Thomson scattering uses an intense x-ray source producing quasi-monochromatic x-rays to probe matter at high density. The x-ray source is typically either a laser-produced plasma [6, 7] or an x-ray free electron laser [8], although other sources such as x-pinches or z-pinches could be considered [2]. Measurements of the spectrally-resolved scattered x-rays can determine important WDM properties such as temperature, density, and ionization [11]. These properties are related to a broad array of topics, including warm dense matter equation of state, influence of correlations on atoms in dense matter, and spectral line formation in white dwarf atmospheres.

1.2. X-ray Scattering

The properties of warm dense matter are difficult to diagnose because the temperatures are too low to excite spectral emission lines and the high densities preclude optical probes from interrogating the interior conditions. Recently-developed x-ray Thomson scattering diagnostics can resolve this dilemma because multi-keV x-rays penetrate into the plasma [12, 13]. A conceptual experiment diagram is shown in Fig. 1.1. Warm dense matter is created by either shocking or radiatively heating a planar sample. A second laser-created plasma provides a source of x-ray line radiation with 3-10 keV photon energies. These photons penetrate the plasma and the spectrally-resolved scattered x-rays are observed in either forward scattering or back scattering geometry using a high-sensitivity x-ray spectrometer. The spectral distribution of the scattered x-rays can be used to infer the density, temperature, and ionization.

It is important to understand that x-ray scattering is not monolithic. The physics that controls the scattering process depends on the details of the experiment configuration and the sample conditions that are probed. In certain cases the theory required to interpret x-ray scattering measurements is well in hand and the measurements may constitute a reliable diagnostic. In other cases the physical properties that control the scattering are themselves a topic of theoretical research. Then the scattering carries information about the theory but the information must be decoded to advance understanding. Thus, it is critical to distinguish which physical regime applies to a particular experimental measurement before determining the optimum method for learning from the data.

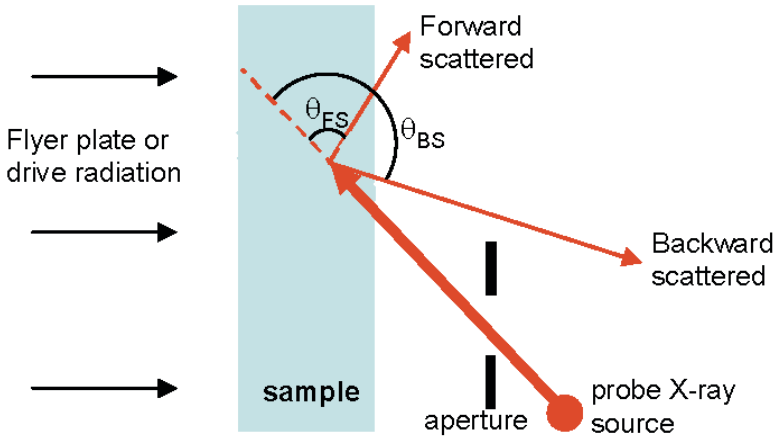

Figure 1.1. Conceptual diagram of an x-ray scattering experiment.

The scattering geometry and incident photon energy E_0 determine the scattering wave vector k = $4\pi E_0/hc$ sin $\theta/2$, where θ = the scattering angle and hc = 12,398 eV-Å. The scale length of density fluctuations that are probed is proportional to $1/k$ and the scattering parameter is defined as $\alpha = 1/k\lambda_s$, where λ_s is the screening length. In ideal non-degenerate plasma λ_s is the Debye length and in degenerate condensed matter it is the Thomas-Fermi screening length. If $\alpha < 1$, then the screening length is bigger than the fluctuation scale length and fluctuations of individual electrons dominate the signal. This is known as non-collective scattering. If $\alpha > 1$, then density fluctuations larger than the screening length are observed and the scattering is predominantly collective. This distinction is important because the physical processes that govern the scattering are different, influencing the diagnostic methods. Operating in the collective or non-collective regimes can be chosen by altering the scattering angle and incident energy. Collective scattering is favored by lower energies and forward scattering and non-collective scattering is favored by higher energy and backward scattering configurations.

The term "X-ray Thomson scattering" is used in the literature to refer to the combination of processes that contribute to spectrally-resolved scattered photon observations. The processes include Compton (inelastic) and Rayleigh (elastic) scattering in the non-collective regime and plasmon and Rayleigh scattering features in the collective regime. Example spectra from the two regimes illustrate the diagnostic information available (Fig. 1.2). Non-collective Mn Heα spectra from a shocked Be experiment [14] were used to determine the electron density from the broadening of the Compton down-shifted spectrum and the electron temperature from the relative intensities of the Compton and Rayleigh peaks (Fig. 1.2). Collective Ti Kα spectra from a shocked LiH experiment [14] were used to determine the electron density from the energy shift of the Plasmon feature and the ion temperature from the relative intensities of the Plasmon and Rayleigh features. A variety of diagnostic methods exist and which method is appropriate depends on the plasma conditions. A unifying theme is that the density, temperature, and ionization information is extracted from spectral energy shifts, the spectral shape, and the relative intensities of the different scattered features.

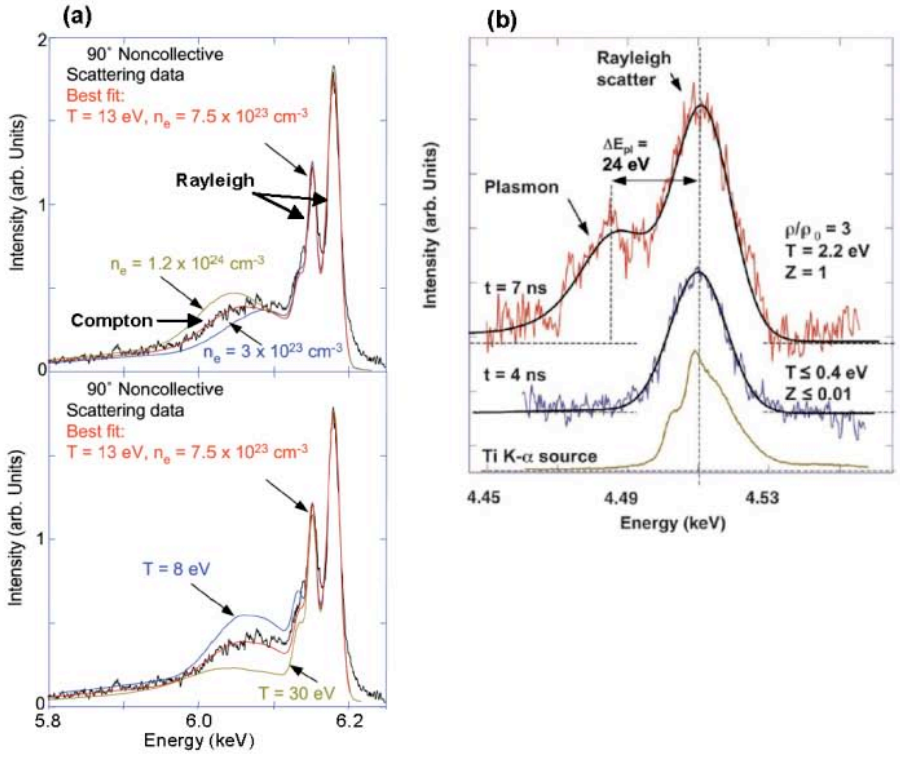

Figure 1.2. The data in (a) is from H. J. Lee *et al.*, PRL 102, 115001 (2009) investigating a shocked Be sample. The top panel shows the sensitivity of fits to electron density and the bottom panel shows the temperature sensitivity. The data in (b) is from A. L. Kritcher *et al.*, Science 322, 69 (2008), which describes investigations of shocked LiH. The bottom spectrum is the source, the 4 ns spectrum is prior to shock heating and compression, and the 7 ns spectrum is after shock heating and compression.

1.3. Literature Survey

The first detailed plans for X-ray Thomson scattering measurements of WDM were published by O. L. Landen *et al.* in 2001 [11]. The successful demonstration of non-collective scattering measurements of density and temperature measurements in isochorically-heated Be were published by S. H. Glenzer *et al.* in 2003 [12]. The first collective scattering measurements appeared in S. H. Glenzer *et al.* (2007) [13], also for isochorically-heated Be. Important measurements of shock-heated materials appear in H. Sawada *et al.* (2007) [16], A. L. Kritcher *et al.* (2008) [14], and H. J. Lee *et al.* (2009) [14]. Several groups have made significant contributions to the theory of x-ray Thomson scattering, notably G. Gregori *et al.* in 2003 [17] and in 2006 [18]. A review article by S. H. Glenzer and R. Redmer has been published in Reviews of Modern Physics [19].

1.4. Project Organization

The research proposed here to characterize warm dense matter requires five activities:

(1) Building an in-house theoretical framework suitable for designing and interpreting experiments;
(2) Creation of a uniform warm dense matter sample;
(3) High sensitivity x-ray spectrometer;
(4) Creation of an intense x-ray probe source;
(5) Experiment design synthesizing prior work, simulations, and realistic experimental capabilities.

The research advancing these topics is described in the following sections.

1.5. Science Goals and Results Summary

The motivation for this work arises from the conjunction of two progress streams in high energy density physics. First, experiments on Z have demonstrated the ability to produce warm dense matter samples with unprecedented uniformity, duration, and size. However, the measurements to date have been limited mainly to density and pressure. Temperature measurements have been performed only on transparent samples that are compatible with optical emission diagnostics. Thus, the temperature information that is essential for completion of the equation of state is missing for many materials. Furthermore, the ability to investigate *why* samples reach their final state conditions requires diagnostics that probe the sample interior microphysics and such diagnostics have been unavailable on Z up to now. The second progress stream is the development of x-ray probe diagnostics on optical laser facilities. These experiments have demonstrated remarkable promise for diagnosing internal sample conditions using x-ray scattering, diffraction, and absorption spectroscopy methods. However, they have been unable to provide benchmark quality material property measurements because the sample conditions are non-uniform and the sample evolution is too rapid. Thus, the overarching goal for this project was to advance high energy density physics by implementing advanced x-ray scattering techniques on Z.

The strategic goal described above will lead to many high-impact science results in the long term. First, stewardship science requires accurate and complete EOS information for many materials that is difficult or impossible to obtain with present methods. Similarly, many astrophysics and geophysics topics require both EOS information and a fundamental understanding of the microphysics that controls the EOS. For example, x-ray probing of high quality (uniform) samples may be the only method that can provide the accurate measurements of iron and iron alloy melting temperatures at earth core pressures. This information is essential for understanding the structure and evolution of our own planet. On a more fundamental level, a major challenge for WDM atomic physics arises from orbital interactions as the inter-ion distance shrinks. As the ions get closer together the orbitals of neighboring ions interact, leading to density broadening, continuum lowering, and pressure ionization. One outcome of this challenge is that no theoretical consensus exists on how to define and calculate the average ion charge. These differences result in different predictions for the quantities that depend on the ion charge such as the transport properties and structure factors. Benchmark quality measurements of warm dense matter ionization could resolve this problem.

We have identified many additional current science problems that could possibly benefit from the implementation of x-ray scattering on Z, ranging from phase changes in high pressure beryllium to investigations of white dwarf star convection zones. We further envision that un-anticipated results are likely to arise. Nevertheless, we elected to focus our efforts on a single high impact experiment in order to optimize the learning-rate to resource-invested ratio. This experiment is aimed at using x-ray scattering to measure temperature in LiD samples shocked to ~ 5-12 Mbar pressures. Discrepancies presently exist for theoretical EOS models and no data presently exists that can resolve these discrepancies. Thus, such information will have significant impact on High Energy Density Physics. Furthermore, LiD samples can be transparent and thus the temperature can also be measured using optical techniques. A cross comparison between x-ray scattering and optical methods will help develop and test understanding of x-ray scattering theories. Decoding x-ray scattering signals requires a model for the physics of atoms embedded in warm dense matter. This poses a dilemma, since the motivation for these investigations is a lack of warm dense matter understanding. In certain regimes, including the LiD experiment proposed here, it can be argued that sufficient understanding exists to permit accurate measurements of temperature, density and ionization. These claims are probably valid in some cases and more tenuous in others. The lack of consensus on the line between regimes with adequate and inadequate understanding leads to concern within the HED physics community about the validity of x-ray scattering results. Resolving this ambiguity would lead to a foundation for understanding warm dense matter and provide new confidence in warm dense matter diagnostics.

The many results described within this report demonstrate that a foundation for x-ray scattering measurements at Z has been established. Perhaps the most significant achievement is the development of in-house Sandia expertise in designing, executing, analyzing, and interpreting x-ray scattering measurements. The importance and difficulty of acquiring this expertise cannot be over-emphasized, especially considering the fact that x-ray scattering is a complex inter-disciplinary field that is also a completely new enterprise at our laboratory. Specific achievements include building an in-house theoretical framework for interpreting x-ray scattering (Section 2), design calculations for creating suitable warm dense matter samples on Z (Section 3), design, fabrication, and testing of a high sensitivity space-resolved x-ray spectrometer (Section 4), and creation of an intense quasi-monochromatic x-ray source (Section 5). Detailed design of the first x-ray scattering experiments planned on Z is described in Section 6. These experiments, scheduled for the fourth quarter of calendar year 2012, are aimed at the logical first step of implementing this complex technique on Z: demonstrating the ability to measure a scattered x-ray signal from a shocked warm dense matter sample. This first step should set our program on a path to obtain the high impact LiD EOS temperature measurements that are described in Section 7. A summary of the LDRD project is given in Section 8.

This page intentionally left blank.

2. THEORY AND MODELING OF X-RAY SCATTERING SIGNALS

2.1. Description of Models

The dominant code used to interpret experiments in the XRTS community was developed at Lawrence Livermore National Laboratory and later at Oxford University by Gregori and collaborators [17]. It is based on a chemical picture of atoms, where bound states have well-defined energies and are well-separated from free electrons. This formal separation allows the use of a separated form for the scattering signal proposed by Chihara [17, 24, 25]:

$$\frac{d^2\sigma}{d\Omega d\omega} = \sigma_T \frac{k_1}{k_0} S(k,\omega), \tag{2.1}$$

with σ_T the Thomson cross section and $S(k,\omega)$ the total dynamic structure factor, separated into electron-electron, electron-ion, and ion-ion parts:

$$S(k,\omega) = \left| f_I(k) + q(k) \right|^2 S_{ii}(k,\omega) + Z_f S^0_{ee}(k,\omega) + Z_c \int \tilde{S}_{ce}(k,\omega-\omega') S_s(k,\omega') d\omega'. \tag{2.2}$$

This approach requires reliable calculations of multiple structure factors valid across a range of electron temperatures and degeneracies and ion coupling parameters (along with form factors $f(k)$ and a screening term $q(k)$ for weakly bound electrons) and is fundamentally parameterized by the quantity Z_f, which represents the number of free electrons.

Gregori's code has been applied to a variety of experimental measurements and has generally been able to reproduce measured data; the best fits of the model to the data are then taken as diagnostic, providing information about the state of the scattering plasma. One of the principal aims of this LDRD was to determine independently the state of the scattering plasma through well controlled and characterized shock processes in order to test scattering models directly. Gregori's code was obtained and used to help design experiments to be fielded on Z and Z-Beamlet. We have also pursued development of an independent theoretical code, following and extending work done on quantum mechanical approaches to scattering by Eisenberger [26, 27], Sahoo [25] and Johnson [28]. Instead of basing these scattering calculations on a chemical picture of the atoms parameterized by Z_f, this approach uses the wavefunctions generated by a self-consistent-field atomic model to calculate directly the quantum mechanical scattering cross sections.

A summary of the self-consistent-field approach can be found in Refs. [20, 21]. The particular model used here, muze, is described in Ref. [23]. Essentially, the material space is divided up into spherical volumes based on the Winger-Seitz radius (which shrinks with increasing density) and wavefunctions are calculated for both bound-state and continuum electrons in an "average atom" with a given nuclear charge and trial screening potential. These wavefunctions are populated an atomic number of electrons that ensure cell neutrality using finite-temperature Fermi statistics; the resultant electron distribution is then used to generate a new screening

potential, and the procedure is iterated until the potential and wavefunctions converge to self-consistent values.

In this "physical picture," bound states remain clearly defined (although ensemble-averaging over multiple cells and broadening effects can broaden and blur the average atom eigenvalues) but unbound (positive-energy) electrons can retain some bound state character. For example, the wavefunction of a 2*p* electron in carbon that becomes pressure-ionized at densities above ~ 1 g/cc does not instantaneously become a free wave; it retains a higher probability of being localized near its parent ion than a truly free electron even though the tail of the wavefunction extends over many Wigner-Seitz radii. These "resonant," or partially bound states should not be expected to give the same scattering as the truly free electrons for which the Chihara model was developed (based on free-electron dielectric functions and structure factors). Instead, they may behave more like the bound states, whose scattering can be described quantum mechanically [26] via:

$$\frac{d^2\sigma}{d\Omega_1 d\omega_1} = \left(\frac{d\sigma}{d\Omega_1}\right)_{Th} \left(\frac{\omega_1}{\omega_0}\right) \sum_{i,f} \left|M_{fi}\right|^2 \delta(\varepsilon_f - \varepsilon_i - \omega) \tag{2.3}$$

where

$$M_{fi} = \left\langle f \left| e^{i\vec{k}\cdot\vec{r}} \right| i \right\rangle, \tag{2.4}$$

with <*f*| a free-wave state and |*i*> a bound state.

The model we have developed for scattering extends the equation above from bound electrons to all electrons in the scattering system, replacing the bound state |*i*> with that of a continuum (but not necessarily free-wave!) electron |*c*>, thus treating scattering from all electrons on an equal footing. The model is still under development: there remain some questions about how to treat the portion of the continuum electrons that extend beyond the Wigner-Seitz radius, whether it is important to use <*c*| rather than <*f*| for the final state, how to account for final state occupation numbers in degenerate regimes, and how to ensure proper normalization of the signal intensities. These are areas of active research.

The intensity of the elastic (Rayleigh) peak is predicted by computing the bound-bound scattering cross sections, replacing <*f*| by <*i*| in the above equation. These intensities can be modulated by an external static ion-ion structure factor (e.g. Ref. [30]) evaluated at the scattering wavenumber *k*. We do not yet calculate the contribution to elastic scattering from free electrons. The fundamental advantage of the physical-picture model is that it does not artificially separate the bound and continuum electrons. Treating all electrons with the same computational mechanics, it will not produce dramatically different signals under pressure ionization of populated valence orbitals. It also provides its own self-consistent values for the average ion charge state, continuum lowering effects, and binding energies, rather than folding in *ad-hoc* theories for those effects or relying on user-defined parameterization. On the other hand, the average-atom model has some significant deficiencies: in real material, a variety of charge states and electron configurations can exist simultaneously and mixtures cannot be treated naturally by

a single-cell atomic model. The very existence of resonant states (or rather, their quantum mechanical manifestation in an extended material) is a matter of theoretical uncertainty. So far, the model is only valid for non-collective scattering (although recent work by Johnson [31] has extended a similar model to the non-collective regime).

We have also developed an intermediate model that uses the temperature-and density-dependent predictions from the self-consistent-field model to parameterize an impact approximation [26, 27] form for the free-electron scattering. It predicts a Gaussian shape for the free-electron feature that can deviate significantly from the quantum mechanical scattering features described above. Like Gregori's model, this approach is parameterized by a quantity Z_f, which is this case is taken to be simply the number of electrons in the Wigner-Seitz cell with positive energies. The bound-free scattering and elastic peak intensity are treated as in the fully quantum mechanical model.

2.2. Calculation Results

Figure 2.1 shows the calculated scattering signals produced for Be and C in a variety of conditions from three models: Gregori's Chihara-based approach, the quantum mechanical approach outlined above (muzeQM), and the quantum mechanical approach using the impact approximation for continuum electrons (muzeIA).

This work was presented at the International Workshop on Warm Dense Matter in 2010 [29] and the quantum mechanical model has been used to model the scattering signal from some of the Z Beamlet experiments measuring the scattered Mn He α-complex signal from CH foams. Figure 2.2 shows the scattering at 90 degrees from muzeQM and Gregori's model, folded with the input x-ray intensities, compared with the measured scattered signal. In this case, the data does not discriminate between models whose primary difference lies in their treatment of free electrons since the downshifted scattering peak is dominated by the bound-free features of low-density carbon's 2*p* electrons.

Increasing the density to above ~ 1 g/cc, where the 2*p* orbitals become pressure ionized in an average atom model, would provide an interesting test of the three models, with both Gregori's approach and muzeIA predicting a dramatic transition in the shape of the scattering feature associated with the free (but resonant) 2*p* electrons. This is illustrated in Fig. 2.3.

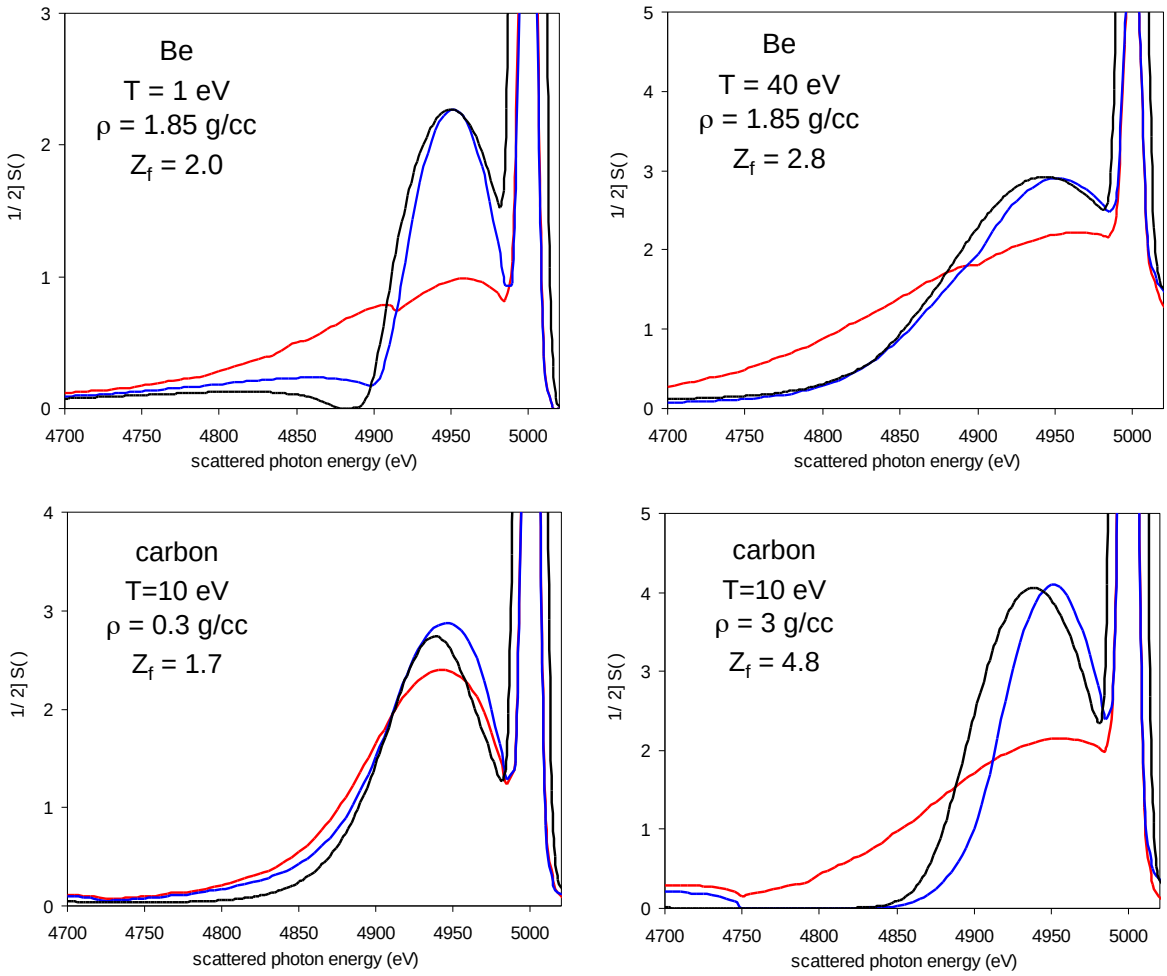

Figure 2.1. Top: Gregori (black), muzeIA (blue), and muzeQM (red) scattering at 90 from solid-density Be at 1 eV (left) and 40 eV (right). The free-electron scattering (*e* > ~4900 eV) is significantly broader in the quantum mechanical model. The elastic peak is ~10x less intense in the two muze models than in the Gregori model. Bottom: predictions from the same three models for T = 10 eV C at 0.3 g/cc and 3 g/cc (densities below and above the pressure ionization limit of the 2*l* electrons.) The free-electron feature in the quantum mechanical model retains a shape reminiscent of the bound-free features and the elastic peak is 4 – 10x less intense in the muze models.

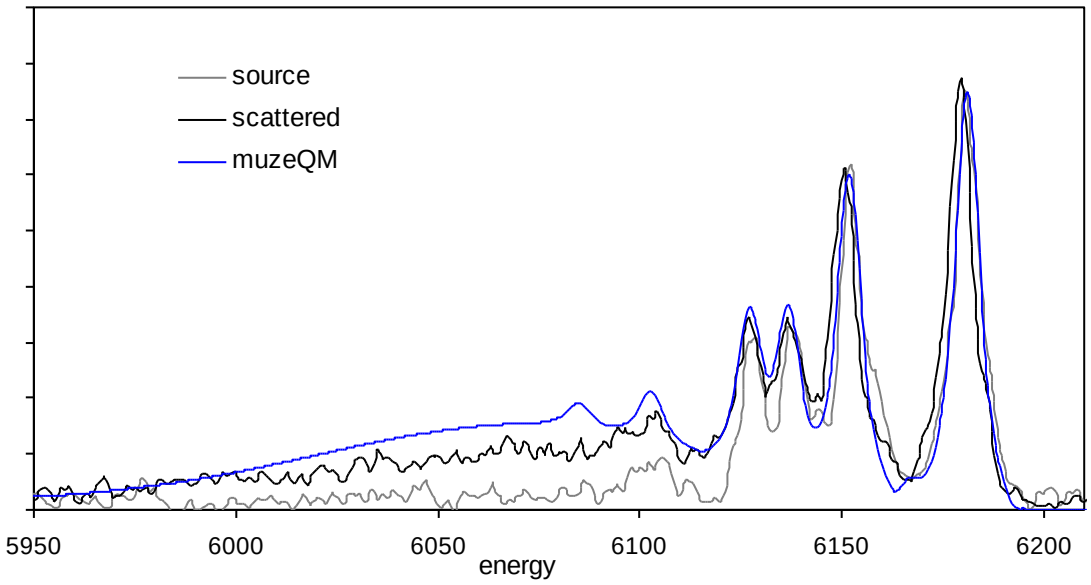

Figure 2.2. Source and scattering spectra from a cold CH target at 90° compared with an integrated scattering signal from the quantum mechanical model.

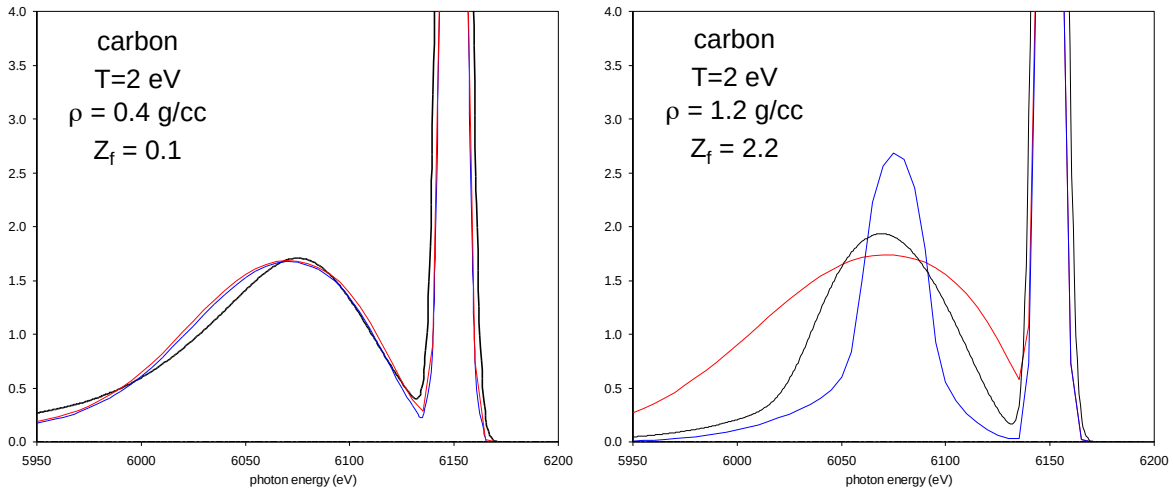

Figure 2.3. Gregori (black), muzeIA (blue), and muzeQM (red) scattering at 90 from carbon at T = 2 eV and density below (left) and above (right) the pressure-ionization limit of 2*p* electrons. The free-electron scattering feature retains its broad shape in the quantum mechanical model.

This page intentionally left blank.

3. DESIGN CALCULATIONS FOR CREATING WARM DENSE MATTER AT Z

3.1. Description of Simulation Technique

The multi-dimensional, radiation, magnetohydrodynamics (MHD) code ALEGRA [32] was used to scope out high velocity flyer plate impact experiments for XRTS studies on the Z accelerator. For foam (CH and CH_2) and beryllium (Be) targets, simulation studies determined density, pressure, and temperature in the shocked state for a range of flyer velocities that can be produced on Z. Two-dimensional (2D) ALEGRA simulations verified a feasible flyer plate load geometry (e.g., conductor dimensions, flyer plate thickness, flight distance, and anode-cathode gap) and shaped current for the first experiments, and determined the charge voltage that Z should operate at to produce the desired conditions. These calculations and key results are summarized below.

A graphical technique is used to scope out the extreme shock conditions that can be produced in Be and foam targets via impacts with the highest velocity Al (aluminum) flyer plates achievable on Z. Figure 3.1 includes plots of pressure vs. particle (mass) velocity on the Hugoniots (the locus of all possible shock states) of Be and Al, Fig. 3.1(a), and Al and CH, Fig. 3.1(b). The Hugoniots are extracted from Sesame equations of state (EOS) 2020 (Be), 3700 (Al), and 7592 (CH). In both plots it is actually the reflected Hugoniot of Al that is plotted; the flyer plate velocity is where $P = 0$. The intersection of the Hugoniots defines the shock pressure and particle velocity in both materials after impact. Initial densities are 2.7 g/cc for the Al flyer plate, and 1.85 g/cc and 0.1 g/cc for Be and CH targets, respectively. Figure 3.1(a) shows the shock pressure produced in a Be target after impact with 30 and 40 km/s Al flyer plates. Figure 3.1(b) plots shock pressure and temperature in a CH target after impact with 35 and 40 km/s Al flyer plates (40 km/s is the maximum feasible for these experiments on Z). Results are similar for CH_2 foam.

By translating the Al Hugoniot along the particle velocity axis in Fig. 3.1 it is possible to determine the shock pressure in Be and foam targets for the range of Al flyer velocities that can be produced on Z, approximately 10-40 km/s. The resulting pressure and particle velocity can be used with shock jump conditions to calculate density, temperature, and shock velocity. Although this technique is quick and convenient for scoping out achievable states, it is necessary to perform MHD simulation to determine a feasible experiment. To this end the ALEGRA code is used.

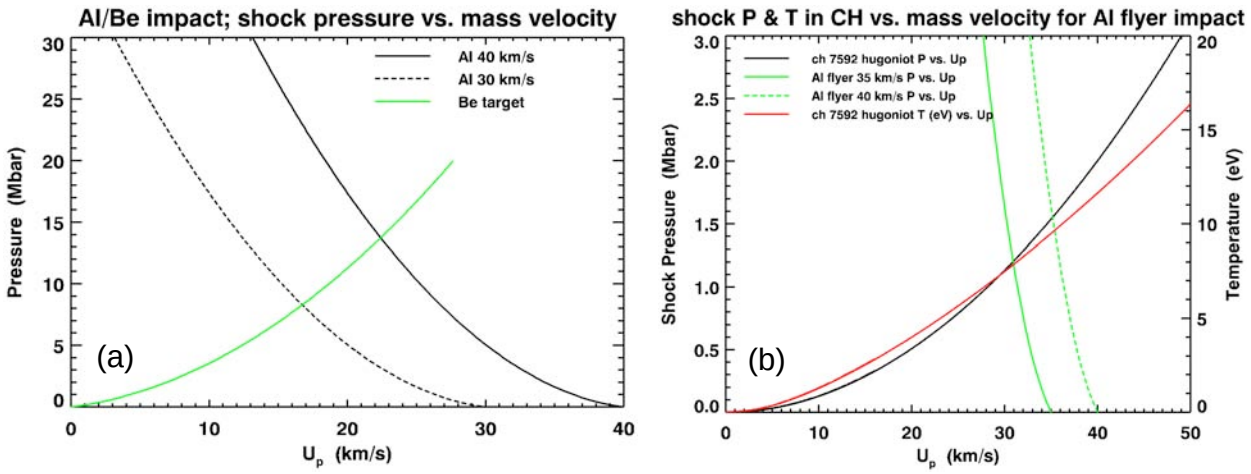

Figure 3.1. (a) Pressure in shocked Be vs. particle velocity produced by impact of 30 km/s and 40 km/s Al flyer plate; black (green) curve is the Be (Al) Hugoniot. (b) Pressure and temperature in shocked CH produced by impact of 35 km/s and 40 km/s Al flyer plate; green curves represent the Hugoniot of Al.

One-dimensional (1D) ALEGRA calculations of the flyer-plate-target impact provide details required to design a feasible experiment. Two types of 1D simulation were performed; self-consistent MHD and ballistic HYDRO. In the MHD case a magnetic pressure drive obtained by analysis of a shot performed on Z self-consistently accelerates an Al flyer plate to impact with a target. MHD simulation determines the state of the flyer plate at impact, how much aluminum remains solid, and timing of shock and release waves in the target, which must be understood in order to choose target dimensions. If the thickness of solid Al remaining in the flyer plate at impact is known, or if one wants to investigate the sensitivity of results to this parameter, then ballistic HYDRO simulation is much faster and equally accurate for determining post-shock conditions. In this case a solid Al flyer plate with initial thickness and constant velocity impacts a target.

3.2. Simulation Results

MHD simulation was used to model experiments with foam and Be targets for an Al flyer plate with initial thickness 1100 μm and impact velocity 32.3 km/s, near the upper end of what is feasible on Z. This simulation is an accurate model of a stripline flyer plate experiment on Z (shot 2027), with the addition of Be and CH targets. The Z capacitor banks were charged to 80 kV. The resulting magnetically insulated transmission line (MITL) and load currents are plotted in Fig. 3.2. Current is lost in the convolute, which is why the peak load current is less than the peak MITL current. The load current produces the magnetic field that accelerates the Al flyer plate in the MHD simulation.

The density of the Al flyer plate and Be target are plotted versus position at a time just before impact in Fig. 3.3(a); approximately 170 μm of Al (on the side of the flyer facing the target) remains solid. The flyer velocity versus time through impact is plotted in Fig. 3.3(b). After impact ($t > 3.265 \times 10^{-6}$ s) the velocity is that of the Al/Be interface. The simulated foam

experiment is similar; the Be target is replaced with CH foam; the flyer plate dynamics and state at impact are identical. Values of density, pressure, and temperature in shocked Be and CH targets are listed in Table 3.1.

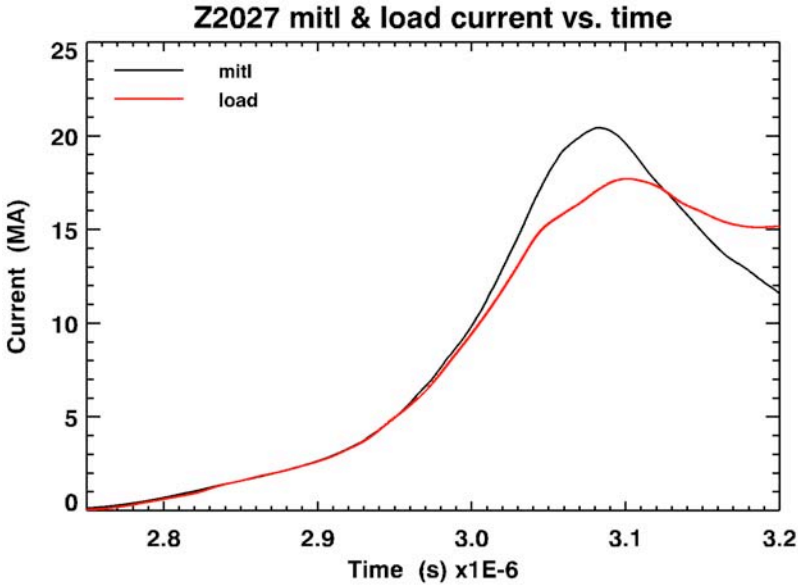

Figure 3.2. Current upstream of the convolute (mitl) and in the stripline (load) in shot 2027.

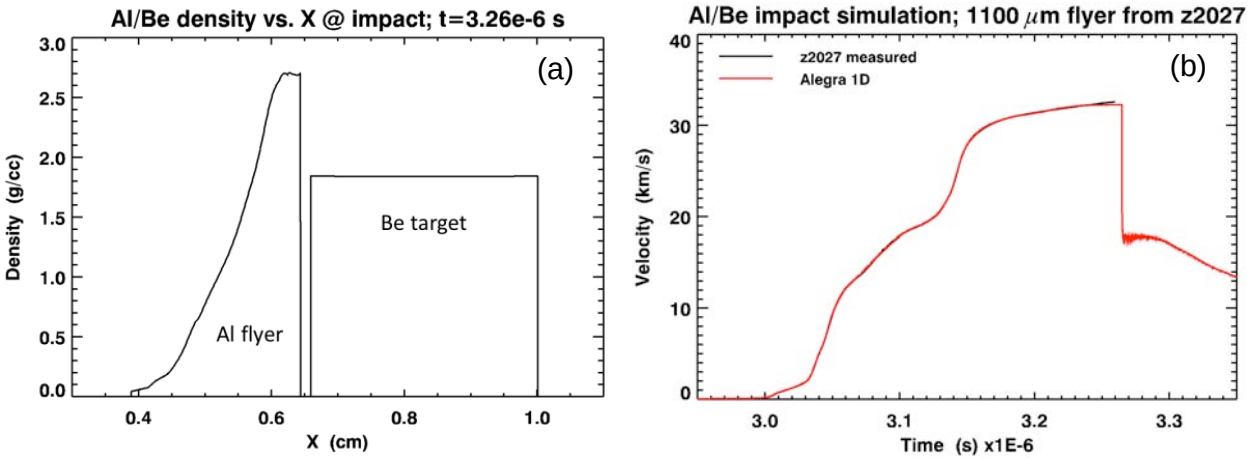

Figure 3.3. (a) Density vs. position just before impact of Al flyer plate with solid Be target. (b) Flyer plate velocity vs. time through impact (t = 3.265 × 10^{-6} s). The black curve is the measured flyer velocity in shot 2027, which is produced quite accurately by the simulation.

Table 3.1. Values of state variables in shocked Be and CH produced by impact with a 32.3 km/s Al flyer plate.

Target Material	Density (g/cc)	Pressure (Mbar)	Temperature (eV)
Be	4.9	9.4	3.1
CH	0.51	1.1	6.8

An important consideration for choosing flyer velocity, and material composition and dimensions of both flyer and target, is the duration of the steady shock state in the target, which is usually referred to as dwell time. The latter is determined by the speed of rarefaction (unloading) and shock waves moving through the flyer-target system after impact. At impact shocks are produced in flyer and target that move in opposite directions to the interface. When the shock in the flyer reaches the solid-liquid transition, a rarefaction wave is produced that travels in the direction of the shock moving in the target, and at a much faster speed, eventually catching up to it. After this time the shock is no longer steady and simple analysis cannot be used to infer state variables.

Much can be learned about target design by plotting the trajectories of the shock and rarefaction waves in the target. These are plotted in Fig. 3.4 for Be and CH targets, Fig. 3.4(a) and Fig. 3.4(b), respectively, for the shock state produced by the 32.3 km/s Al flyer in the simulated experiment. In each plot $X = 0$ is the location of the flyer/target interface. The slope of the shock trajectory is $1/U_S$, where U_S is the shock speed. The slope of the rarefaction trajectory is $1/U_R$, where U_R is the rarefaction speed. The time at which a wave arrives at position X is given by

$$t_s = \frac{x}{U_S} + t_{S0} \tag{3.1}$$

$$t_R = \frac{x}{U_R} + t_{R0} \tag{3.2}$$

where the subscripts S and R denote shock and rarefaction; t_{S0} (t_{R0}) is the time at which the shock (rarefaction) wave is produced (arrives) at the flyer/target interface. Let X_c represent the position at which the shock and rarefactions waves merge; at this position $t_S = t_R$.

The shock is produced at the same time in both cases. However, the rarefaction wave (in the flyer) arrives at this interface much faster in the impact with Be; 19 ns and 189 ns after impact for Be and CH, respectively. The shock pressure in the flyer after impact with Be is 8.5 times larger than is produced by the impact with CH (Table 3.1). Consequently, compared to an impact with CH, pressure waves travel much faster in the flyer after it impacts Be, so the rarefaction wave arrives much earlier at the Al/Be interface, and merges with the shock wave in the target much faster; 36 ns and 341 ns after impact in Be and CH, respectively. When the rarefaction wave arrives at the Al/Be (Al/CH) interface, 0.056 (0.687) cm of target material is in a steady shocked state. The steady state is lost after the rarefaction wave catches up to the shock.

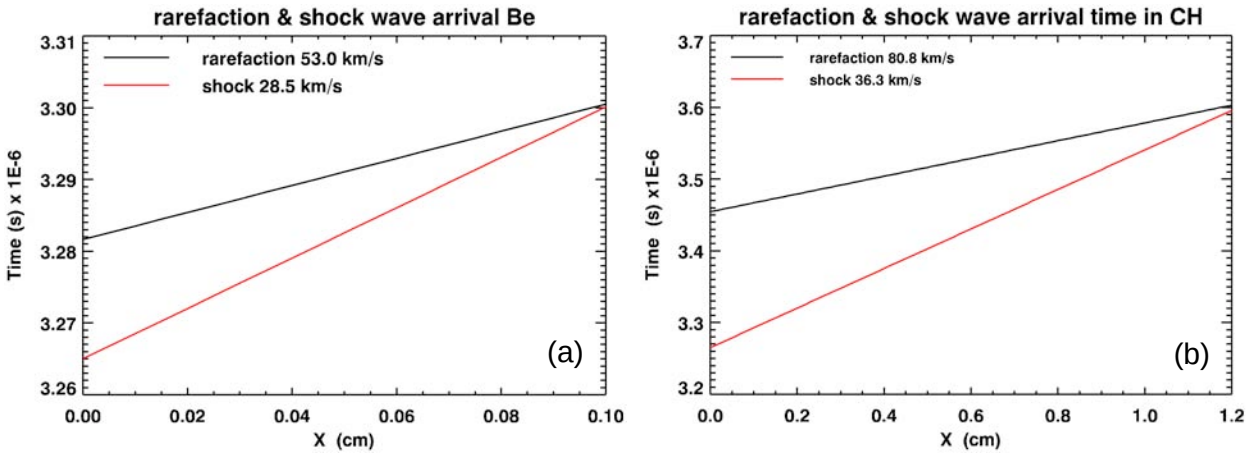

Figure 3.4. Arrival time of shock and rarefaction waves at distance X from the flyer/target interface at impact for (a) Be and (b) CH targets.

The results of this simulated experiment indicate the shock states that can produced in Be and CH targets in a flyer plate impact experiment on the Z accelerator (in machine time) operated close to the upper limit of allowed charging voltage (85 kV). Also, these results indicate an advantage of using a foam target versus a Be target. A foam target can be much thicker than a Be target (by more than a factor of 10), and since the duration of the steady shock state is over 9 times longer in CH, one has significantly more time to make the XRTS measurement.

To reduce the risk of damaging ZBL (Z-Beamlet laser) optics by debris from the flyer plate load, the first XRTS experiments on Z will likely be shot near the minimum charge voltage (50 kV). Consequently, the flyer velocity will be much less than 32 km/s. Also, after much consideration the XRTS team decided on using a CH_2 foam target. An impact study was performed using ballistic HYDRO simulation (as described above) to scope out shock conditions that could be produce by an Al flyer plate with velocity in the range 10-20 km/s. In these simulations the flyer plate thickness is 200 μm, realistic for this range of velocities. Three foam densities were simulated; 0.050 g/cc, 0.075 g/cc, and 0.100 g/cc. Sesame table 7171 is used for the CH_2 EOS. Plots of shock pressure, density, and temperature in CH_2 vs. flyer velocity are shown in Fig. 3.5. Figure 3.6 includes plots of shock and release wave speed, and the location in the target at which these waves merge, versus flyer velocity. These plots can be used in conjunction with Eqns. 3.1 & 3.2 to construct a trajectory plot (similar to Fig. 3.4) for the shock and release waves in the target for a given flyer velocity.

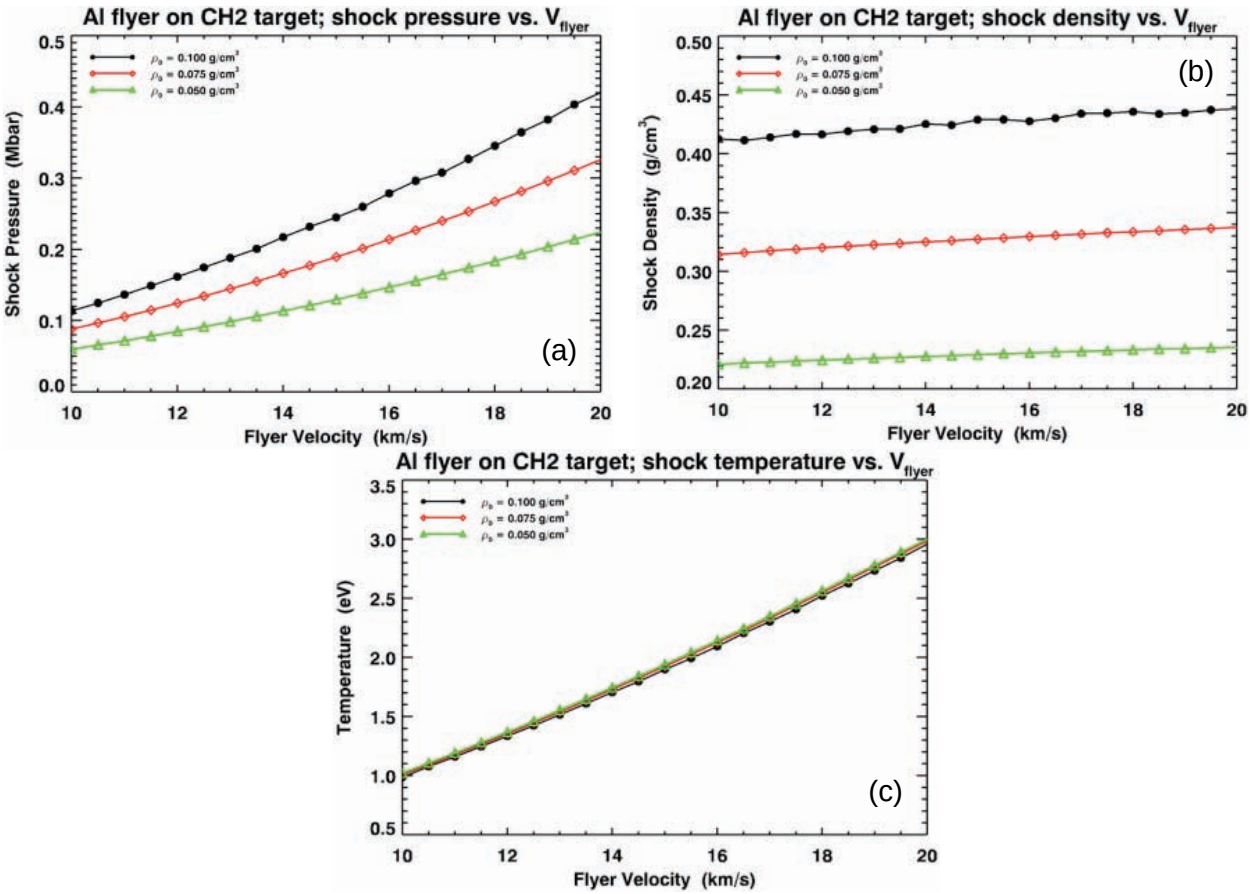

Figure 3.5. Plots of (a) pressure, (b) density, and (c) temperature vs. flyer velocity in shocked CH_2 foam for initial densities 0.100 g/cc (black dots), 0.075 g/cc (red diamonds), and 0.050 g/cc (green triangles).

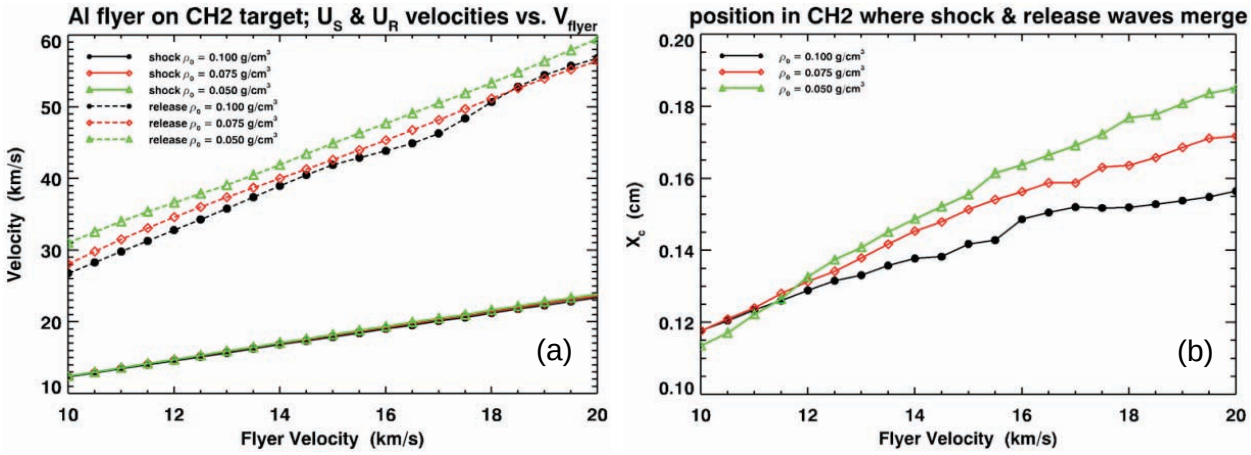

Figure 3.6. Shock and release wave speed (a) and merge location (b) vs. flyer velocity in shocked CH_2 foam for initial densities 0.100 g/cc (black dots), 0.075 g/cc (red diamonds), and 0.050 g/cc (green triangles).

The results in Fig. 3.6(b) depend on the thickness of solid Al remaining in the flyer at impact, which is 200 μm in these ballistic HYDRO calculations. The dwell time of the steady shock state and X_c both increase with increasing thickness of solid flyer at impact. Furthermore, for a given flyer plate material and velocity, the required charging voltage of the Z capacitor banks depends on the flyer thickness and vice versa. The magnitude of the accelerating magnetic field increases with increasing charge voltage, which increases the rate at which the magnetic field burns through the flyer (via Joule heating). Thus, running the experiment at the lowest charge voltage that achieves the desired velocity maximizes the thickness of solid material remaining in the flyer at impact.

Two-dimensional ALEGRA calculations were performed to determine the feasibility of a new load design for these experiments. A cross section of the coaxial load simulated is shown in Fig. 3.7. Relevant dimensions are 9 × 2 mm (X × Y) cathode (tungsten), 17 × 4 mm anode opening (1 mm ak-gaps top and bottom; 4 mm on the sides), and 1200 μm thick flyer plates (Al) top and bottom; the effective shorting height (in Z) is 56 mm. Anode material is aluminum. The snapshot in Fig. 3.7(b) at later time shows conductor deformation, which has a significant effect on the amplitude of the magnetic field accelerating the flyer plates; 2D simulation is needed to self-consistently account for this effect.

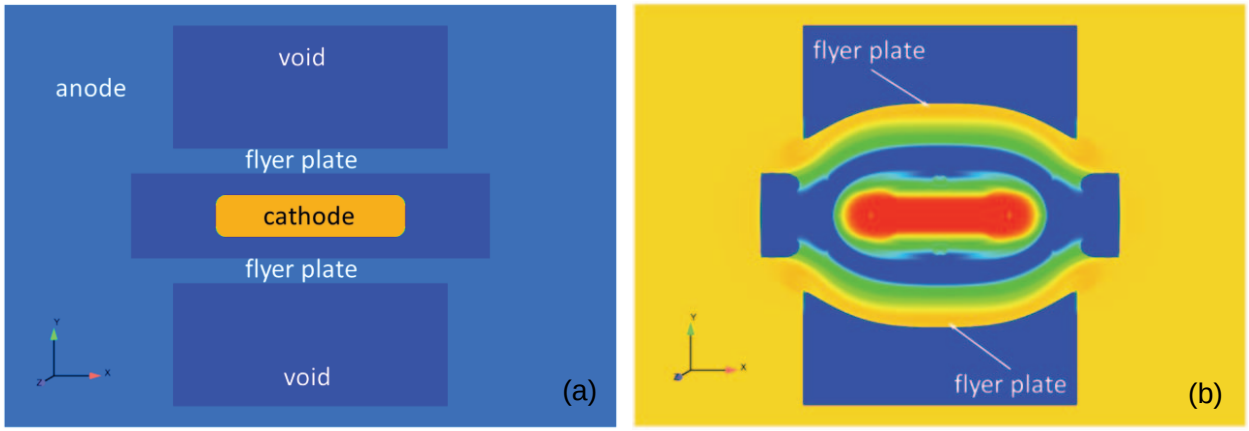

Figure 3.7. Cross section of symmetric, coaxial load for XRTS experiments at (a) initial time in simulation, and (b) 560 ns later. Solid colors represent density. The cathode material is tungsten, the anode and flyer plate material is aluminum, and dark blue represents void (density = 0.0).

The coaxial flyer plate load design depicted in Fig. 3.7 is a slight modification of one that was recently fielded in another experiment at 60 kV (shot 2385), which produced excellent results. The load current from shot 2385 was scaled by 0.85 to get an effective charge voltage near 50 kV; the resulting current, shown in Fig. 3.8(a), was used to energize the 2D simulation. The resulting flyer velocity and position versus time are plotted in Fig. 3.8(b). The rise time of the current is shaped to compress the Al flyer shocklessly during acceleration, which is accomplished in the simulation.

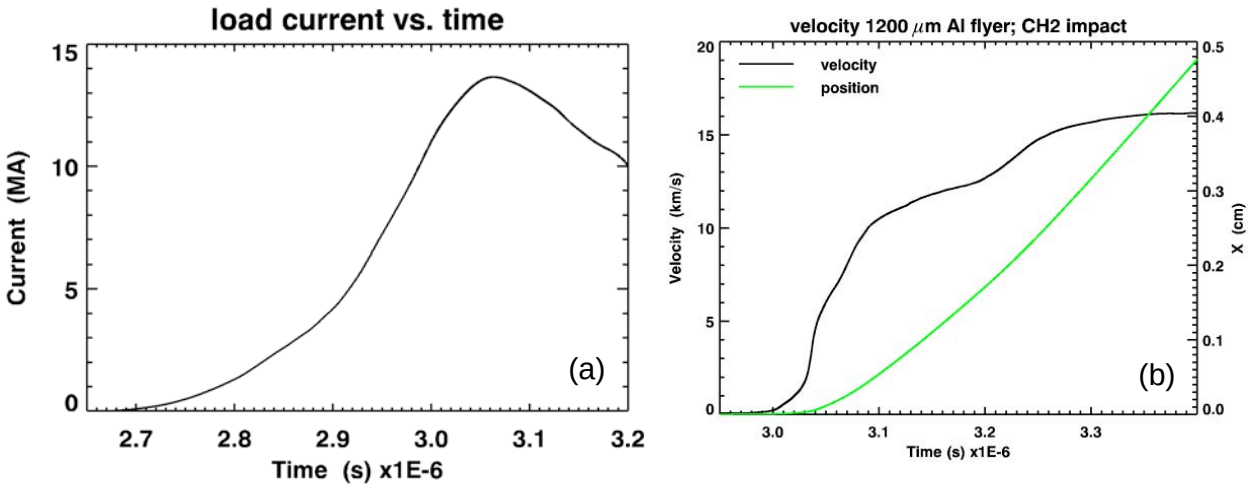

Figure 3.8. (a) Load current vs. time that energizes the 2D ALEGRA simulation. (b) The resulting flyer velocity and position (of the flyer free surface) vs. time.

The flight distance, the initial distance between flyer and target (y-dimension of top and bottom void regions in Fig. 3.7), is set so that the flyer plate velocity is near ballistic at impact. Based on the flyer velocity time history shown in Fig. 3.8(b), the flight distance for the XRTS impact experiment is set to 4 mm. With this flight distance the Al flyer plate impacts the CH_2 target at time $t = 3.353 \times 10^{-6}$ s with velocity 16 km/s.

The density, material phase, and temperature versus position X in the flyer plates at impact are shown in Fig. 3.9(a). The material phase parameter is 1 for solid and 3 for not solid, which is determined by a Lindeman melt law. If possible, it is more accurate to use the EOS to determine material phase. Nevertheless, Fig. 3.9(a) indicates the thickness of solid material in the Al flyer is greater than 300 μm. The melt temperature of Al at standard pressure is about 933 K. About 330 μm of solid Al remains at temperature less than 700 K at impact with the target, almost a factor of 2 more than in the high velocity case discussed above. Consequently, the dwell time increases significantly, as is shown in Fig. 3.9(b). The latter is a plot of the arrival time of shock and release waves in a CH_2 target for two thicknesses of solid Al flyer plate; 200 μm and 330 μm. For a target thickness of 0.15 cm, the duration of the steady shock state is about 1.7 times longer when the flyer thickness is 330 μm (about 75 ns); furthermore the release wave never catches up with the shock wave. Based on these results, the dimensions of the CH_2 target for initial XRTS experiments are 0.15 cm in length and 5 mm in cross-section.

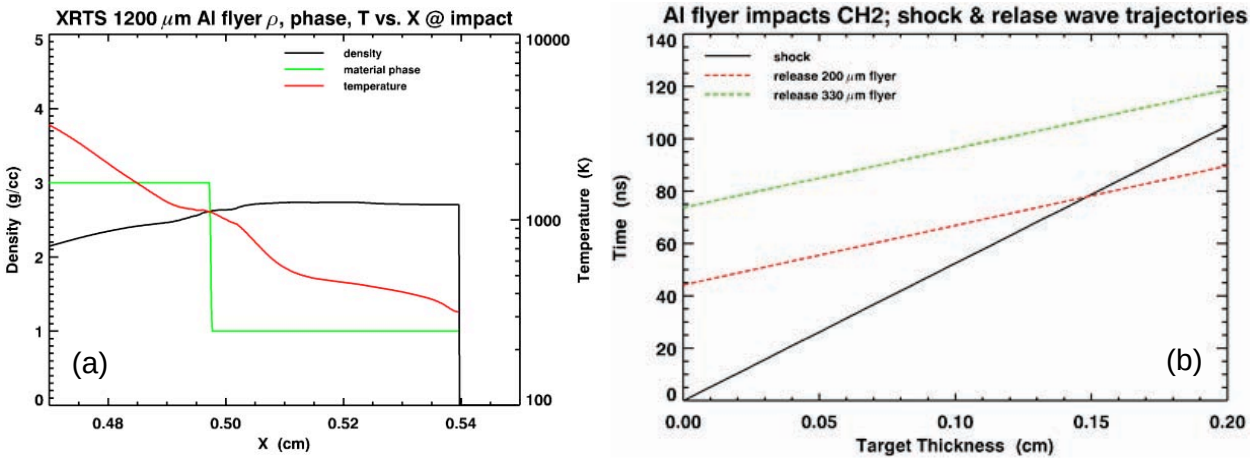

Figure 3.9. (a) Density, material phase, and temperature vs. position in the Al flyer plate at impact. Material phase is 1 for solid and 3 for not solid. (b) Arrival time of shock and release waves vs. position in CH_2 target.

3.3. Discussion and Conclusions

This simulation study produced a coaxial load design for initial XRTS experiments. A simulated experiment verified that the proposed shaped current shocklessly accelerates the initially 1200 μm thick Al flyer plates to near ballistic speed of 16 km/s over a flight distance of 4 mm. Thus, at impact with a CH_2 target (0.15 cm in thickness), 330 μm of the Al flyer plate remains in a solid state. This is important for the standard shock physics experiment on the side opposite the XRTS, the results of which will complement the XRTS experiment.

Initial transmission line simulations using results from the 2D ALEGRA calculation determined the timing of the laser triggered switches, and the capacitor bank charging voltage, 54 kV, that produces the desired shaped current on Z. The calculations summarized here form a validated, science based approach for designing accurate flyer plate impact experiments on the Z accelerator [33-35]; thus, they can be considered an accurate prediction of conditions produced in XRTS experiments.

This page left intentionally blank.

4. X-RAY SPECTROMETER

4.1. Requirements

X-ray scattering signals are weak because the scattering cross section is small. Thus, the vast majority of x-ray scattering measurements performed to date have employed Highly Oriented Pyrolytic Graphite (HOPG) crystals in the Von Hamos configuration. This setup provides high efficiency and enabled the first pioneering proof of principle measurements. However, it has the significant disadvantages that the spectral resolution is relatively low ($\sim \lambda/\Delta\lambda \sim E/\Delta E < 300$) and there is no spatial resolution. The latter problem implies that it is difficult or impossible to be certain that the scattering arises from a homogeneous plasma region. Without this certification, true benchmark quality data cannot be obtained. Thus, we believe spatial resolution is an essential requirement for Z x-ray scattering measurements.

Recently, Gamboa et al. [36] examined an imaging x-ray crystal spectrometer for XRTS using a double-focusing toroidally bent single germanium crystal. It was demonstrated that such an imaging spectrometer allows high spatial resolution within a large field-of-view combined with spectral resolution significantly higher than commonly used HOPG spectrometers. One issue of toroidally bent crystals is the need for precise alignment over six axes. Subtle errors in source positioning and Bragg angle setting can degrade the spatial resolution due to defocusing. A second disadvantage is that toroidal crystals are extremely expensive. This can be significant for Z experiments since it is possible that the crystals will be severely damaged by accelerator debris.

The drawbacks of the toroidal geometry led to selection of a spherical crystal spectrometer for Z x-ray scattering experiments. A focusing spectrometer with high spatial and spectral resolution, and high sensitivity using a spherically bent crystal has been built to measure XRTS on the Z experiments, referred as the x-ray scattering spherical spectrometer (XRS^3). In this section, the relative x-ray reflectivity, spatial and spectral resolution of spherically bent single crystals of quartz, mica, and germanium measured on a Manson x-ray source are presented. Cylindrically and spherically bent HOPG, and spherically bent highly annealed pyrolytic graphite (HAPG) mosaic crystals were also characterized as baseline comparisons.

4.2. Spherical Spectrometer Overview

The development and operation of focusing spectrometers with spatial resolution (FSSR) has been well described in Refs. [37-39], only a short overview is presented here. These spectrometers are based on spherically bent crystals with a large open aperture and small radius of curvature, which can be used to provide one- or two-dimensional spatial resolution (FSSR-1D or FSSR-2D, respectively). Though technically a 2-D imaging system, the FSSR-2D geometry can be used in such a way that it becomes a spectrometer with one dimension of spectral resolution, as shown in Fig. 4.1. High spectral and spatial resolutions, as well as high luminosity, are obtained with the absence of a slit by using the double-focusing aspects of spherically bent crystals and the Bragg crystal diffraction. A source emits radiation that is

incident upon the surface of a spherically bent crystal, with a radius of curvature R. X-rays from the source are dispersed from the crystal according to the Bragg equation,

$$n\lambda = 2d\sin\theta\,, \tag{4.1}$$

where d is the spacing of the crystal lattice planes, θ is the grazing angle between the incident ray and the crystal plane, λ is the reflected wavelength, and n is the order of the reflection (an integer ≥ 1).

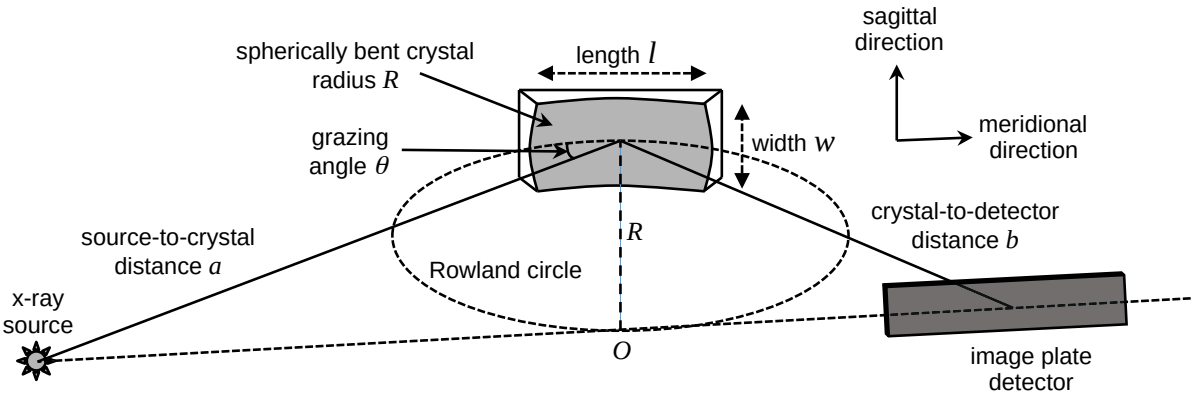

Figure 4.1. FSSR-2D experiment setup.

The analysis of the rays reflecting from the surface of the spherically bent crystal are best understood in terms of the meridional and sagittal planes of the crystal. The meridional plane corresponds to the plane of spectral dispersion, where the rays reflect from the crystal at various angles. The sagittal plane is perpendicular to the meridional plane, and is in this plane all of the rays reflect off of the crystal at approximately the same angle and point-to-point focusing can be achieved with little or no astigmatism. Spatial focusing by the spherical surface in the sagittal plane is achieved according to the lens formula,

$$\frac{1}{a}+\frac{1}{b}=\frac{2\sin\theta}{R}, \tag{4.2}$$

where a and b are the source-to-crystal and crystal-to-detector distances. A useful tool in the description of spherically bent optics is the Rowland circle, a circle with radius $R/2$ that intercepts the center point of the crystal. It has the property that rays from a point on the Rowland circle are focused back onto the Rowland circle, with each such ray reflecting off the crystal at the same angle. The detector is placed along the sagittal focal positions for the x-ray source, which all lie on a line passing through the point O on the Rowland circle.

4.3. Crystal Measurement Method

The relative x-ray collection efficiency, spatial and spectral resolution of spherically bent single crystals of quartz, mica, and germanium were each characterized with x-rays generated from a Manson x-ray source using the experimental setup shown in Fig. 4.2. The Manson x-ray source is an electron-beam device that excites atoms in the anode through electron-impact ionization. As the excited atoms decay, they give off isotropically distributed x-rays at energies characteristic of the anode source material. In these experiments, an electron beam current of 0.35 mA with electron beam energy of 8.0 keV was used to excite a manganese anode. The main spectral lines of interest occur at energies of 5.899 and 5.887 keV (Mn-K-α_1 and Mn-K-α_2 emission, respectively), while the spectral line at 6.490 keV (Mn-K-β) is useful for calibrating spectral dispersion. The generated x-rays were observed through two viewing ports each at 45° relative to the surface of the anode. At one viewing port, the x-rays were monitored with a Si-PIN x-ray photodiode detector (Amptek XR-100CR), which provided a cumulative count of the generated x-rays. At the other viewing port, the x-rays were directed toward the x-ray crystal of interest. The spherically bent single crystals all had radius of curvatures of 150 mm, thicknesses of < 0.1 mm, and were placed at a source-to-crystal distance of 300 mm. The HOPG and HAPG crystals also had radius of curvatures of 150 mm, but were placed at a source-to-crystal distance of 250 mm to enable simultaneous mosaic-focusing and physical focusing. A list of other relevant crystal parameters is given in Table 4.1.

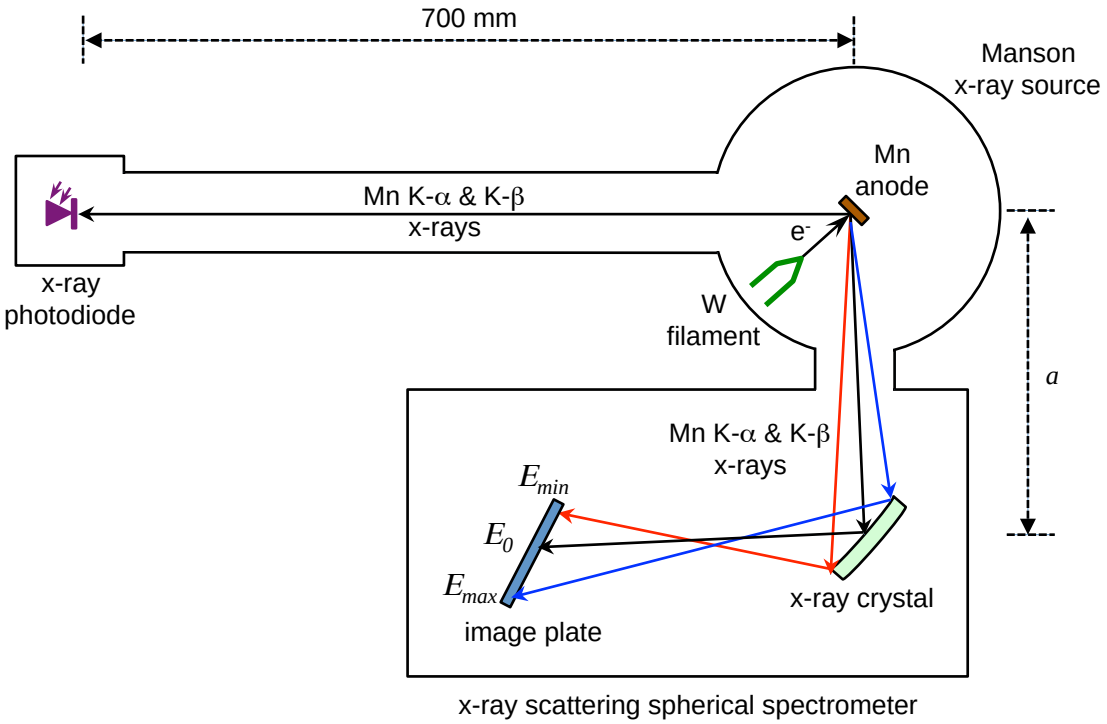

Figure 4.2. Manson source calibration setup. For calibrations using HOPG/HAPG crystals, a = 250 mm, while for calibrations using all other crystals, a = 300 mm.

Table 4.1. Crystal parameters: $2d$ is the crystal spacing; n is the order of reflection; θ is the grazing angle; l and w are the crystal length and width, respectively; and a is the source-to-crystal distance.

Label	Vendor	Crystal	$2d$ (Å)	n	θ (°)	l (mm)	w (mm)	Comments
HOPG-MP-CLY	Momentive Performance	HOPG 002	6.708	2nd	37	50	30	Cylindrically bent, 2 mm thick
HOPG-MP	Momentive Performance	HOPG 002	6.708	2nd	37	50	30	2mm thick
HOPG-OG	Optigraph	HOPG 002	6.708	2nd	37	45	25	100 μm thick
HAPG-OG	Optigraph	HAPG 002	6.708	2nd	37	45	25	40 um thick
QU20-23-IN	Inrad	Quartz 20-23	2.749	1st	46	60	18	-
QU20-23-IN-VT	Inrad	Quartz 20-23	2.749	1st	46	60	36	Vertical tiling
QU20-23-EC-HT	Ecopulse	Quartz 20-23	2.749	1st	46	50	20	Horizontal tiling
MICA-FS	FSSR	Mica I	19.915	7th	46	48	15	-
MICA-EC-VT	Ecopulse	Mica I	19.915	7th	46	50	36	Vertical tiling
GE422-IN	Inrad	Germanium 422	2.310	1st	64	50	10	-
GE220-IN	Inrad	Germanium 220	4.000	1st	31	50	10	-

The x-rays were reflected from the crystal and recorded onto an image plate (IP) detector. Because of the harsh electromagnetic pulse (EMP) environment of the Z-accelerator, solid-state electronic detectors and controllers are not readily feasible for Z experiment, so typically x-ray film is used. In contrast, IPs are totally immune to EMP interference, capable of detecting x-rays with photon energies of 1–100 keV, and have a dynamic range several orders larger than x-ray film [40]. The IP is a reusable recording medium consisting of x-ray sensitive material made from BaF(Br,I):Eu^{2+} phosphor crystals suspended in a plastic binder [41]. The incident x-rays ionize Eu^{2+} to Eu^{3+}, generating photoelectrons that become trapped in lattice defects (F-centers) created by the absence of the halogen ions (F, Br, I) crystals. This process stores a latent image in the IP phosphor that is metastable and fades exponentially over time through thermally activated spontaneous recombination of the trapped photoelectrons and Eu^{3+} ions [42-44]. The resulting pattern may be retrieved using an IP scanner, which irradiates the IP with red laser light that excites the trapped photoelectrons to recombine with Eu^{3+} ions and release blue light. This photostimulated luminescence (PSL) is collected by a photomultiplier tube, digitized and stored as an electronic image. The crystal characterizations were conducted using Fuji Biological Analysis System (BAS) TR-type IPs, and a Fuji BAS-5000 scanner with the following settings: *Sensitivity* S1000, *Latitude* L4, and *Scan Resolution* 25 μm.

For each crystal of interest, multiple calibration runs were performed to allow statistical averaging. Each calibration run consisted of exposing an IP to x-rays from the Manson x-ray source for approximately 360 s. The actual duration of x-ray exposure for each calibration run was determined by maintaining a consistent cumulative x-ray count as measured by the Si-PIN

photodiode x-ray detector. Aluminum (0.1 μm) and Kapton (140 μm) filters were used in front of the IP. After the x-ray exposure was completed, the IP was removed from the vacuum chamber, with care being taken to restrict exposure to visible light that could de-excite the metastable x-ray image recorded on it. For each calibration run, the IP was scanned at about 75 minutes after the end of the x-ray exposure. For TR-type IPs, A. L. Meadowcroft *et al.* [44] measured a 1/e decay time of 35.5 minutes, thus any variations in the extracted PSL signal due to slight differences in scan times would have been minimal.

4.4. Crystal Measurement Results

The results of crystal calibrations are presented in this section. A compilation of the x-ray collection efficiency data for all of the crystals is presented in Table 4.2. The photon energy range corresponds to difference between the lowest (E_{min}) and highest (E_{max}) photon energies measured on the image plate. The spectral resolution ($E/\Delta E$) is calculated using the measured full-width-half-max (FWHM) of the Mn-K-α_1 (5.899 keV) spectral line. The IP-spectral and IP-spatial values are the FWHM extents along the spectral and spatial directions, respectively, of the Mn-K-α_1 spectral line at the image plate without any magnification corrections. The peak fluence is the maximum PSL value of the Mn-K-α_1 spectral line. To calculate the crystal collection efficiency, the fluence within the corresponding IP-spectral and IP-spatial area of the Mn-K-α_1 spectral line was integrated. The integrated fluence of the cylindrically bent HOPG crystal (HOPG-MP-CLY) was used as the baseline. The relative collection efficiency for each crystal was calculated as the ratio its integrated fluence divided by the baseline HOPG-MP-CLY integrated fluence. As final comparison, the relative collection efficiency per width is calculated by taking into account each crystal width in ratio to the width of the HOPG-MP-CLY crystal.

Table 4.2. Crystal x-ray collection efficiency results.

Label	Photon energy (eV)	Energy range (eV)	Spectral resolution	IP-spectral (mm)	IP-spatial (mm)	Peak fluence (PSL/pixel)	Relative collection efficiency (%)	Relative collection efficiency per crystal width (%)
HOPG-MP-CLY	5690 – 6695	1005	620	0.850	3.496	4.40	100	100
HOPG-MP	5675 – 6865	1190	705	0.734	2.263	4.05	47.5	47.5
HOPG-OG	5685 – 6915	1230	810	0.672	2.362	2.05	30.2	36.2
HAPG-OG	5695 – 6905	1210	955	0.568	0.738	2.18	15.7	18.8
QU20-23-IN	5625 – 7170	1550	1410	0.181	0.163	3.51	1.9	3.2
QU20-23-IN-VT	5630– 7190	1560	1405	0.178	0.162	6.86	3.8	3.2
QU20-23-EC-HT	5685– 6905	1220	1460	0.166	0.194	3.10	1.9	2.9
MICA-FS	5550 – 6745	1195	1425	0.186	0.181	0.57	0.3	0.5
MICA-EC-VT	5540 – 6700	1160	1115	0.239	0.756	0.31	0.8	0.7
GE422-IN	5650 – 6120	470	1385	0.142	0.200	14.63	4.5	13.5
GE220-IN	4905 – 6410	1505	1235	0.676	0.418	0.79	2.1	6.3

4.4.1. Highly oriented/annealed pyrolytic graphite (HOPG/HAPG)

Thick highly oriented pyrolytic graphite (HOPG) crystals were obtained from the Momentive Performance company. The HOPG crystals were molded into solid pieces (50 mm long by 30 mm wide by 2 mm thick), one cylindrically bent (HOPG-MP-CLY) with radius of curvature of 150 mm, and one spherically bent (HOPG-MP) with radius of curvature of 150 mm, and glued onto aluminum mounts, as shown in Fig. 4.3. The graphite (002) of the HOPG crystal has a crystal spacing ($2d$) of 6.708 Å, so to measure the Mn spectra produced by the Manson x-ray source 2nd order reflection was used at a central Bragg angle (θ) of 37°. The IP x-ray image of the Mn spectra measured with the HOPG-MP-CLY crystal in mosaic focusing mode (a = 250 mm) is shown in Fig. 4.4. The recorded Mn-K-α_1 line on the IP was quite large with a spectral extent FWHM of 0.850 mm and a spatial extent FWHM of 3.496 mm. The HOPG-MP-CLY had a wide spectral range ($E_{max} - E_{min}$ = [6695 – 5690] eV = 1005 eV) that was able to capture both the Mn-K-α and Mn-K-β lines, as shown in Fig. 4.5(a). However, it has a poor spectral resolution $E/\Delta E$ of only 620, and the detail view of Fig. 4.5(b) show that the Mn-K-α_1 and Mn-K-α_2 lines are not well resolved. The peak fluence of the Mn-K-α_1 line was 4.40 PSL/pixel.

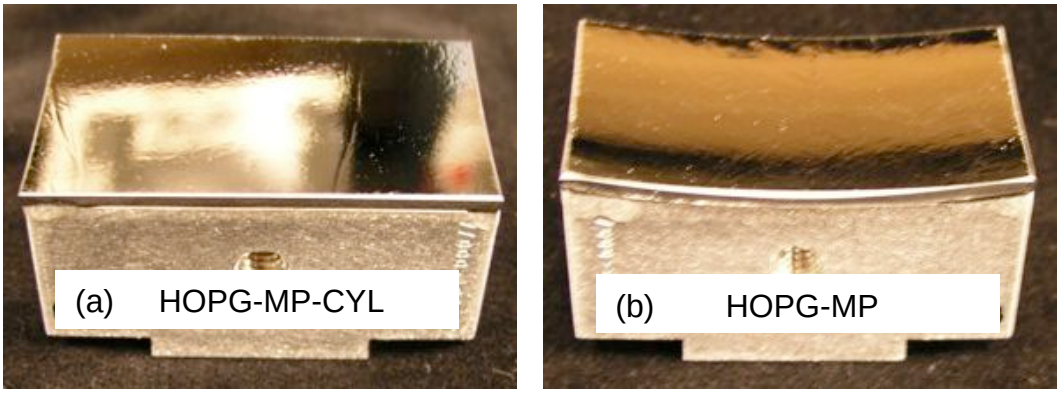

Figure 4.3. Thick (2mm) HOPG crystals (Momentive Performance): (a) cylindrically bent, and (b) spherically bent.

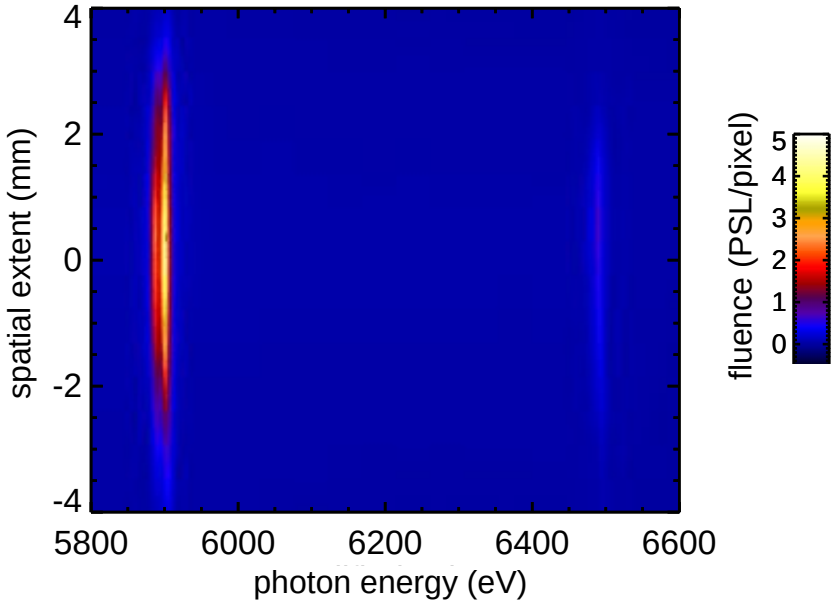

Figure 4.4. IP x-ray image of Mn spectra measured with thick (2 mm) cylindrically bent HOPG crystal (HOPG-MP-CLY).

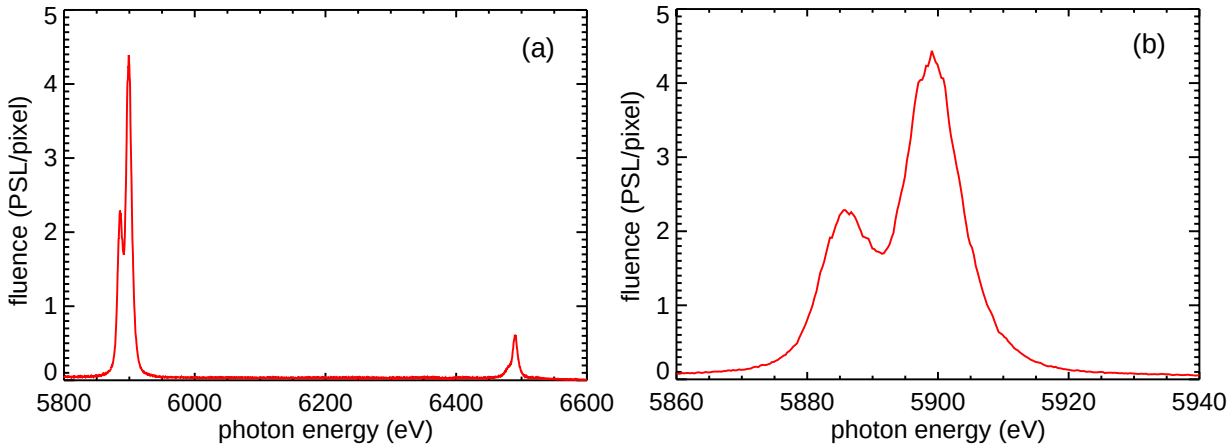

Figure 4.5. Mn spectra measured with thick (2mm) cylindrically bent HOPG crystal (HOPG-MP-CLY): (a) wide range, (b) detail view of K-α_1 and K-α_2.

The IP x-ray image of the Mn spectra measured with the spherically bent HOPG-MP crystal in mosaic focusing mode (a = 250 mm) is shown in Fig. 4.6. The recorded Mn-K-α_1 line on the IP was somewhat smaller with a spectral extent FWHM of 0.734 mm and a spatial extent FWHM of 2.263 mm. The HOPG-MP also has a slightly wider spectral range ($E_{max} - E_{min}$ = [6865 – 5675] eV = 1190 eV), and captured both the Mn-K-α and Mn-K-β lines, as shown in Fig. 4.7(a).

Spherically bending the HOPG crystal did improved slightly the spectral resolution, but it was still rather poor ($E/\Delta E$ = 705), and the Mn-K-α_1 and Mn-K-α_2 lines are not well resolved (Fig. 4.7 (b)). The peak fluence of the Mn-K-α_1 line decreased a little (I_P = 4.05 PSL/pixel). Compared to the cylindrically bent HOPG, the spherically bent HOPG had a relative collective efficiency of η = 47.5%. Since HOPG-MP-CLY and HOPG-MP are the same width (30 mm), the relative collective efficiency per crystal width is also η_w = 47.5%.

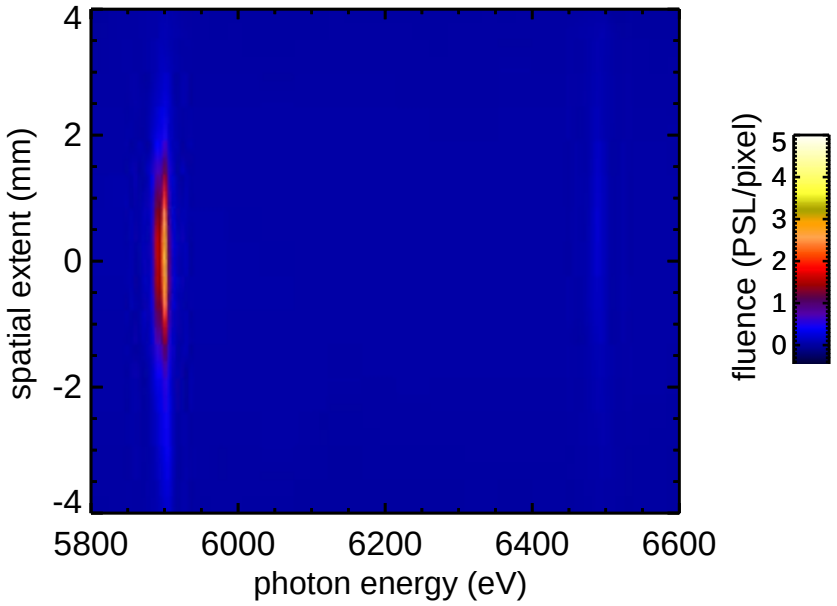

Figure 4.6. IP x-ray image of Mn spectra measured with thick (2mm) spherically bent HOPG crystal (HOPG-MP).

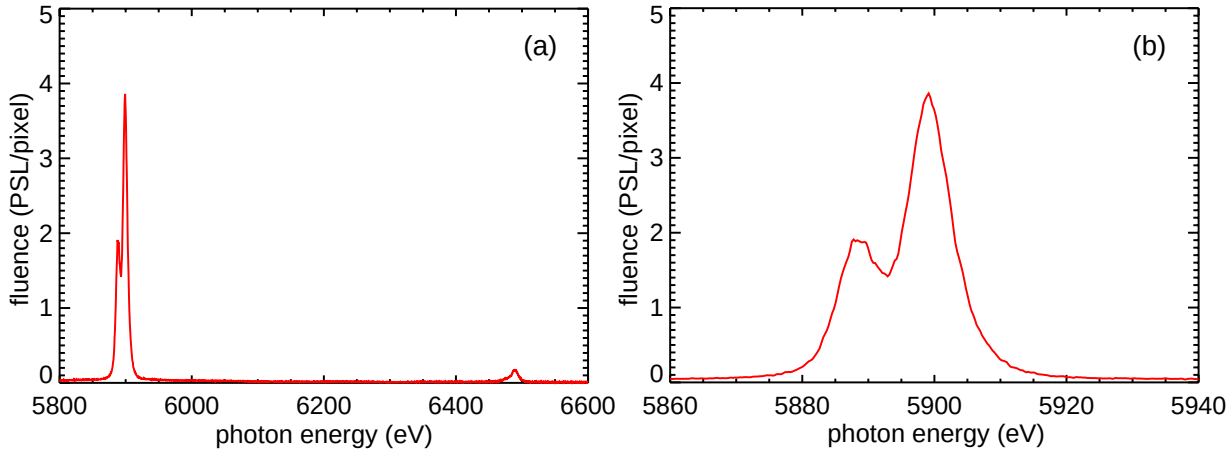

Figure 4.7. Mn spectra measured with thick (2mm) spherically bent HOPG crystal (HOPG-MP): (a) wide range, (b) detailed view of K-α_1 and K-α_2.

Thinner pyrolytic graphite crystals were obtained from the company of Optigraph, as shown in Fig. 4.8. In one case, pyrolytic graphite was deposited onto a BK7 glass substrate (45 mm long by 25 mm wide) that was spherically polished to a radius of curvature of 150 mm to create a 100 μm thick spherically bent HOPG crystal (HOPG-OG). In another case, pyrolytic graphite was deposited onto an identical BK7 glass substrate and then heated to create a 40 μm thick spherically bent highly annealed pyrolytic graphite crystal (HAPG-OG). The HAPG crystal has the same crystal spacing as the HOPG crystals, so to the measure the Mn spectra the same Bragg angle and order of reflection is used. The IP x-ray image of the Mn spectra measured with the HOPG-OG crystal in mosaic focusing mode (a = 250 mm) is shown in Fig. 4.9. Compared to the thick HOPG-MP crystal, the thin HOPG-OG crystal had similar IP extents for the Mn-K-α_1 line ($IP_{spectral}$ = 0.672 mm, $IP_{spatial}$ = 2.362 mm), spectral range ($E_{max} - E_{min}$ = [6915 – 5685] eV = 1230 eV), as shown in Fig. 4.10(a). The spectral resolution was improved somewhat ($E/\Delta E$ = 810), and the Mn-K-α_1 and Mn-K-α_2 lines are just starting to become resolved (Fig. 4.10(b)). The peak fluence of the Mn-K-α_1 line was reduced to 2.05 PSL/pixel, and the relative collective efficiency was down to 30.2%. Due to the difference in crystal widths between HOPG-MP-CLY (30 mm) and HOPG-OG (25 mm), the relative collection efficiency per crystal width of the latter is 36.2%.

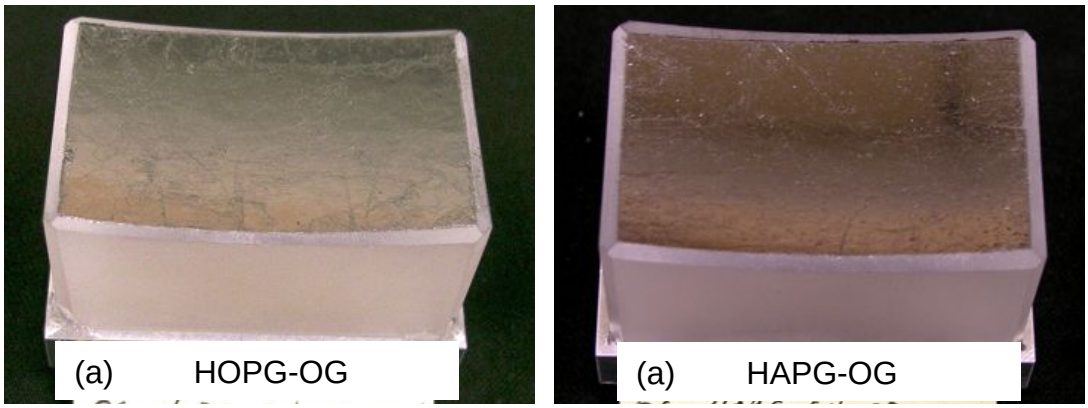

Figure 4.8. Thin spherically bent pyrolytic graphite crystals (Optigraph) on BK7 glass substrates: (a) HOPG (100 μm), and (b) HAPG (40 μm).

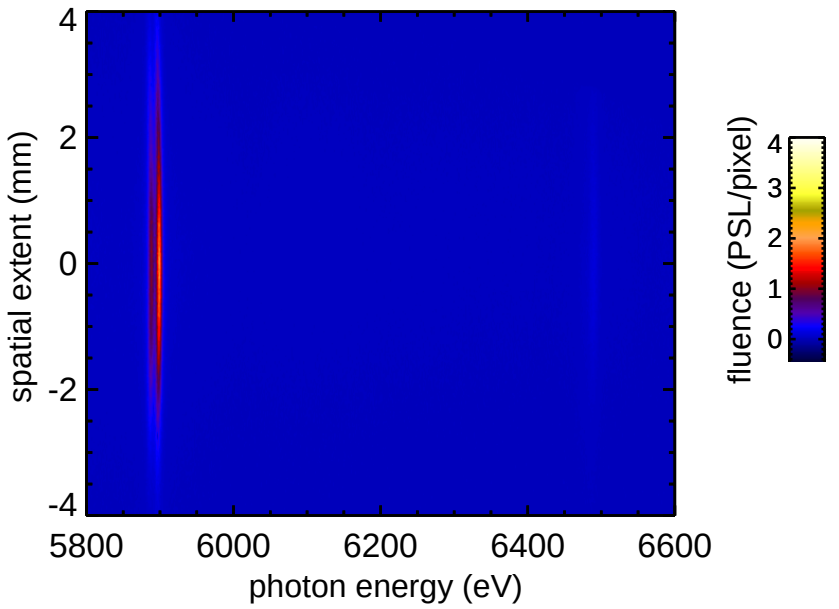

Figure 4.9. IP x-ray image of Mn spectra measured with thin (100 μm) spherically bent HOPG crystal (HOPG-OG).

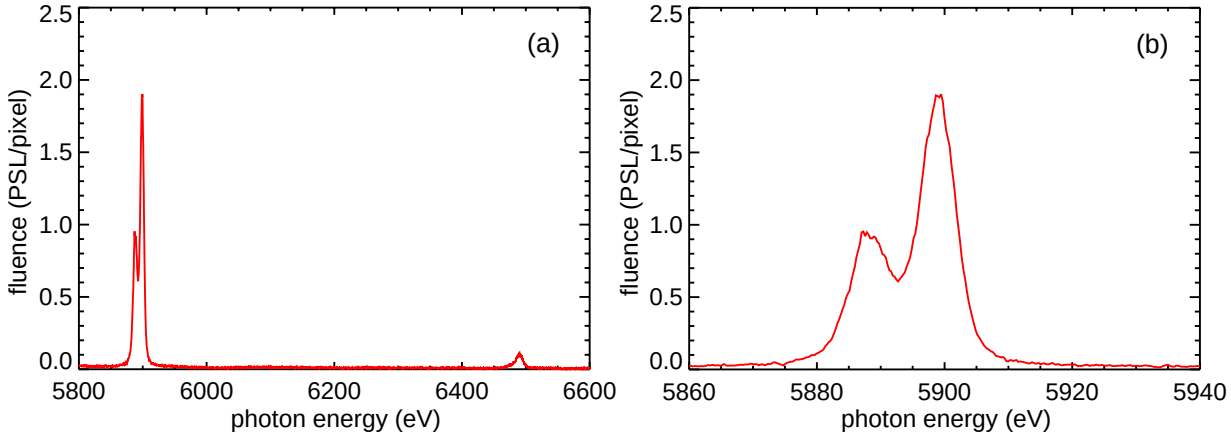

Figure 4.10. Mn spectra measured with thin (100 μm) spherically bent HOPG crystal (HOPG-OG): (a) wide range, (b) detailed view of K-α_1 and K-α_2.

The IP x-ray image of the Mn spectra measured with the HAPG-OG crystal in mosaic focusing mode (a = 250 mm) is shown in Fig. 4.11. The HAPG-OG crystal had noticeable improvement over the HOPG-OG crystal in the IP extents for the Mn-K-α_1 line ($IP_{spectral}$ = 0.568 mm, $IP_{spatial}$ = 0.738 mm), and spectral resolution ($E/\Delta E$ = 955), as shown in Fig. 4.12. While the spectral range ($E_{max} - E_{min}$ = [6905 – 5695] eV = 1210 eV) and peak fluence (I_P = 2.18 PSL/pixel) were similar to the HOPG-OG crystal. The relative collective efficiency and the relative collection efficiency per crystal width were further reduced to η = 15.7 and η_w = 18.8%, respectively. As expected, no spatial information could be resolved for any of the HOPG/HAPG crystals. To

simultaneously measure x-rays with both spectral and spatial resolution thin single crystals are need, as presented in the following sections.

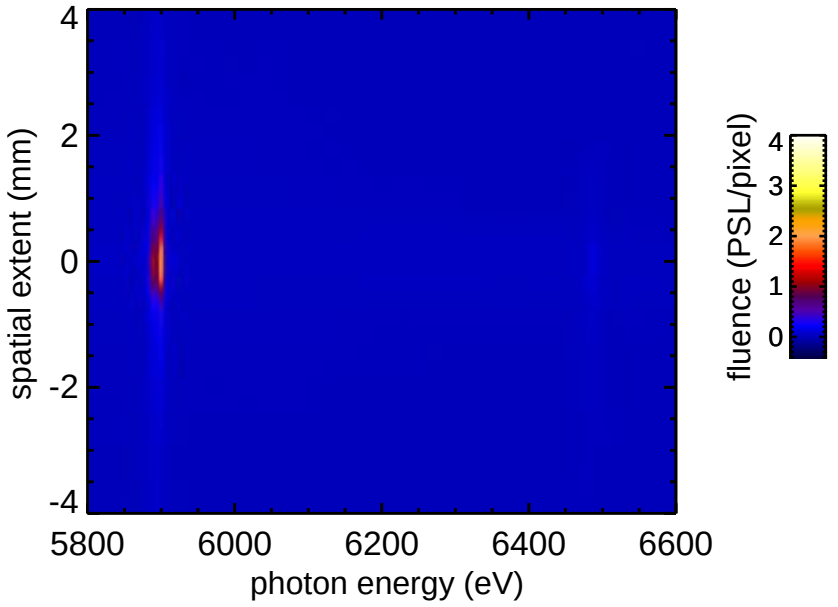

Figure 4.11. IP x-ray image of Mn spectra measured with thin (40 μm) spherically bent HAPG crystal (HAPG-OG).

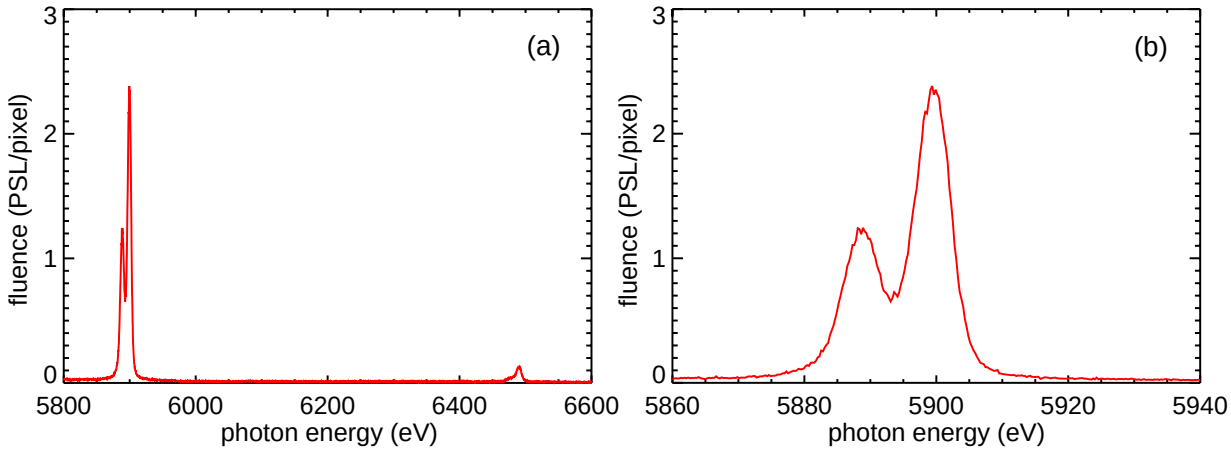

Figure 4.12. Mn spectra measured with thin (40 μm) spherically bent HAPG crystal (HAPG-OG): (a) wide range, (b) detailed view of K-α_1 and K-α_2.

4.4.2. Quartz

Spherically bent quartz 20-23 crystals (< 100 μm thick) were obtained from two suppliers, the Inrad company and the Ecopulse company, as shown in Fig. 4.13. Inrad provided a single quartz 20-23 crystal (60 mm long by 18 mm wide) bent onto a BK7 glass substrate that was spherically polished to a radius of curvature of 150 mm (QU20-23-IN). Because of fine polishing precision, the crystal is held onto the substrate only by optical contact with no glue required. The crystal suppliers were asked to fabricate larger spherically bent crystals, but they were unable to produce them successfully. Instead, Inrad provided two crystals bent onto a BK7 glass substrate tiled vertically with an overall size of 60 mm long by 36 mm wide (QU20-23-IN-VT). Alternatively, Ecopulse provided two crystals bent onto a BK7 glass substrate tiled horizontally with an overall size of 50 mm long by 20 mm wide (QU20-23-EC-HT). In this case, glue was used to affix crystals to the substrate. For the quartz 20-23 crystals, the Mn spectra were measured with a source-to-crystal distance of 300 mm (1st order reflection, $2d$ = 2.749 Å, θ = 46°).

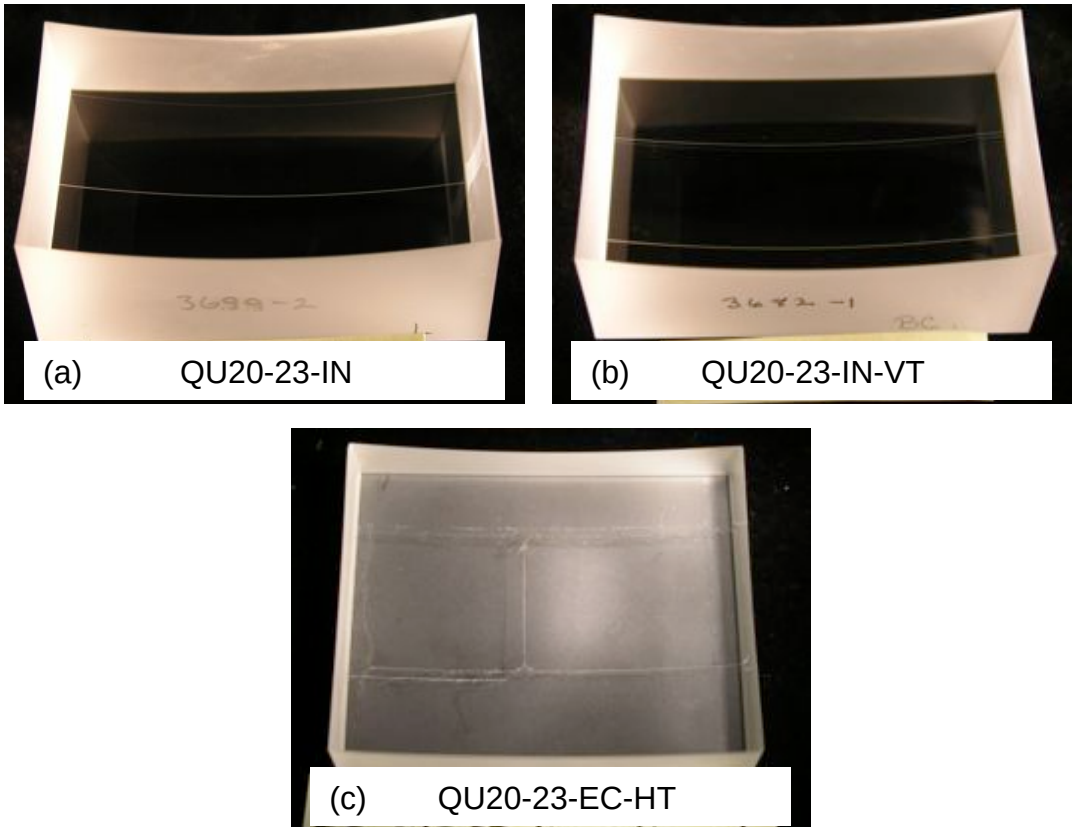

Figure 4.13. Spherically bent quartz 20-23 crystals on BK7 glass substrates: (a) single crystal (Inrad), (b) two vertically tiled crystals (Inrad), and (c) two horizontally tiled crystals (Ecopulse).

The IP x-ray image of the Mn spectra measured with the QU20-23-IN crystal is shown in Fig. 4.14, and the spectral lineouts are shown in Fig. 4.15. Overall, there was considerable

improvement over the HOPG crystals, ($IP_{spectral}$ = 0.181 mm, $IP_{spatial}$ = 0.163 mm, $E/\Delta E$ = 1410, $E_{max} - E_{min}$ = [7170 – 5625] eV = 1550 eV). However, as expected there was a reduction in x-ray collection efficiency compared to the baseline cylindrically bent crystal (I_P = 3.51 PSL/pixel, η = 1.9%, η_w = 3.2%). Nonetheless, the ability of a thin spherically bent single crystal to spectrally and spatially resolve x-rays is highly valuable. In a slightly modified calibration, an array of 65 μm thick Au wires vertically spaced with 180 μm wide gaps was placed in front of the Mn anode, and the QU20-23-IN crystal was moved slightly back to image the Au wires, as shown in Fig. 4.16. The IP x-ray image of the Mn spectra and spatial lineout of the Mn-K-α_1 spectral line demonstrated that Au wires are resolved with a spatial resolution of about 75 μm.

The IP x-ray image of the Mn spectra measured with the QU20-23-IN-VT crystal is shown inFig. 4.17, and the spectral lineouts are shown in Fig. 4.18. The vertically tiled crystals produce similar results as the single crystal ($IP_{spectral}$ = 0.178 mm, $IP_{spatial}$ = 0.162 mm, $E/\Delta E$ = 1405, $E_{max} - E_{min}$ = [7190 – 5630] eV = 1560 eV). Because QU20-23-IN-VT was twice as large as QU20-23-IN, there was an increase of about a factor of two in the x-ray collection efficiency (I_P = 6.86 PSL/pixel, η = 3.8, η_w = 3.2%).

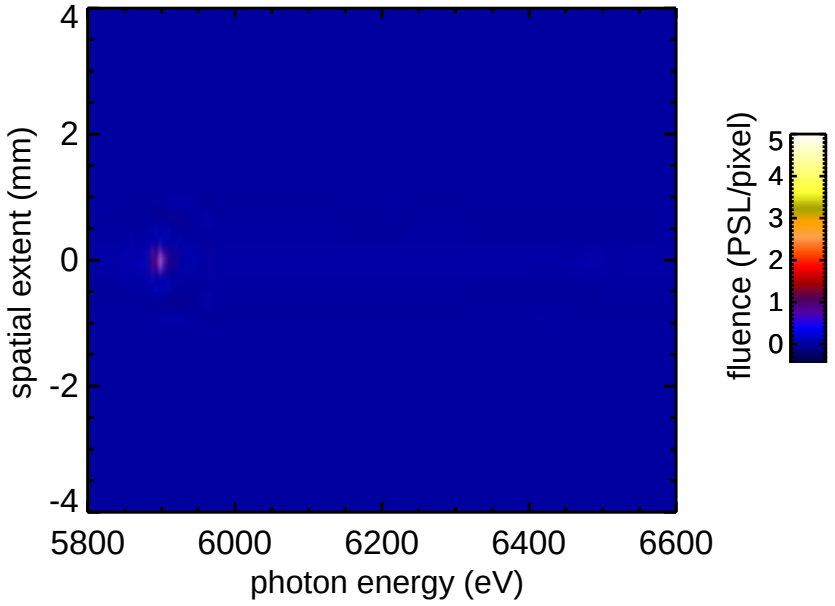

Figure 4.14. IP x-ray image of Mn spectra measured with spherically bent quartz 20-23 single crystal (QU-20-23-IN).

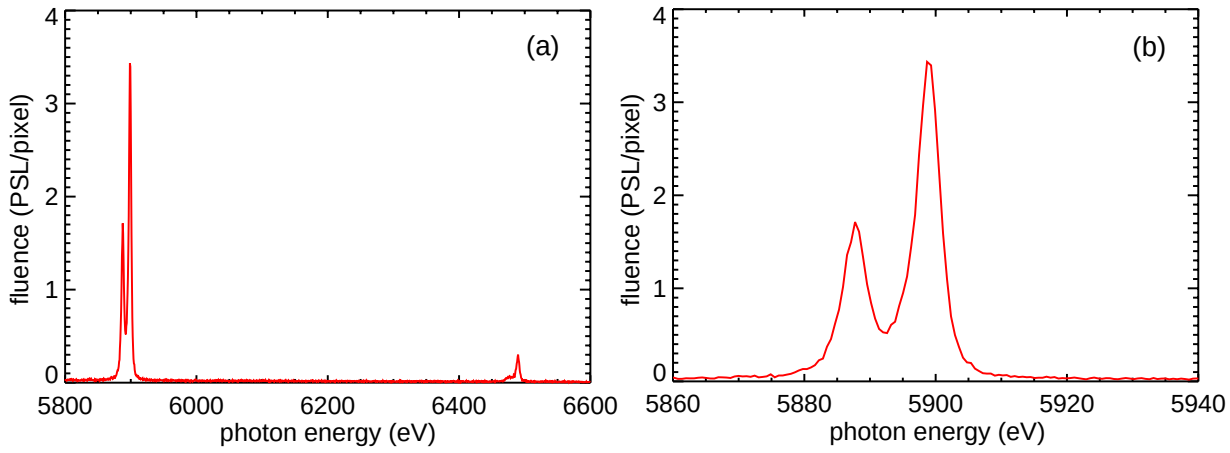

Figure 4.15. Mn spectra measured with spherically bent quartz 20-23, single crystal (QU-20-23-IN): (a) wide range, (b) detailed view of K-α_1 and K-α_2.

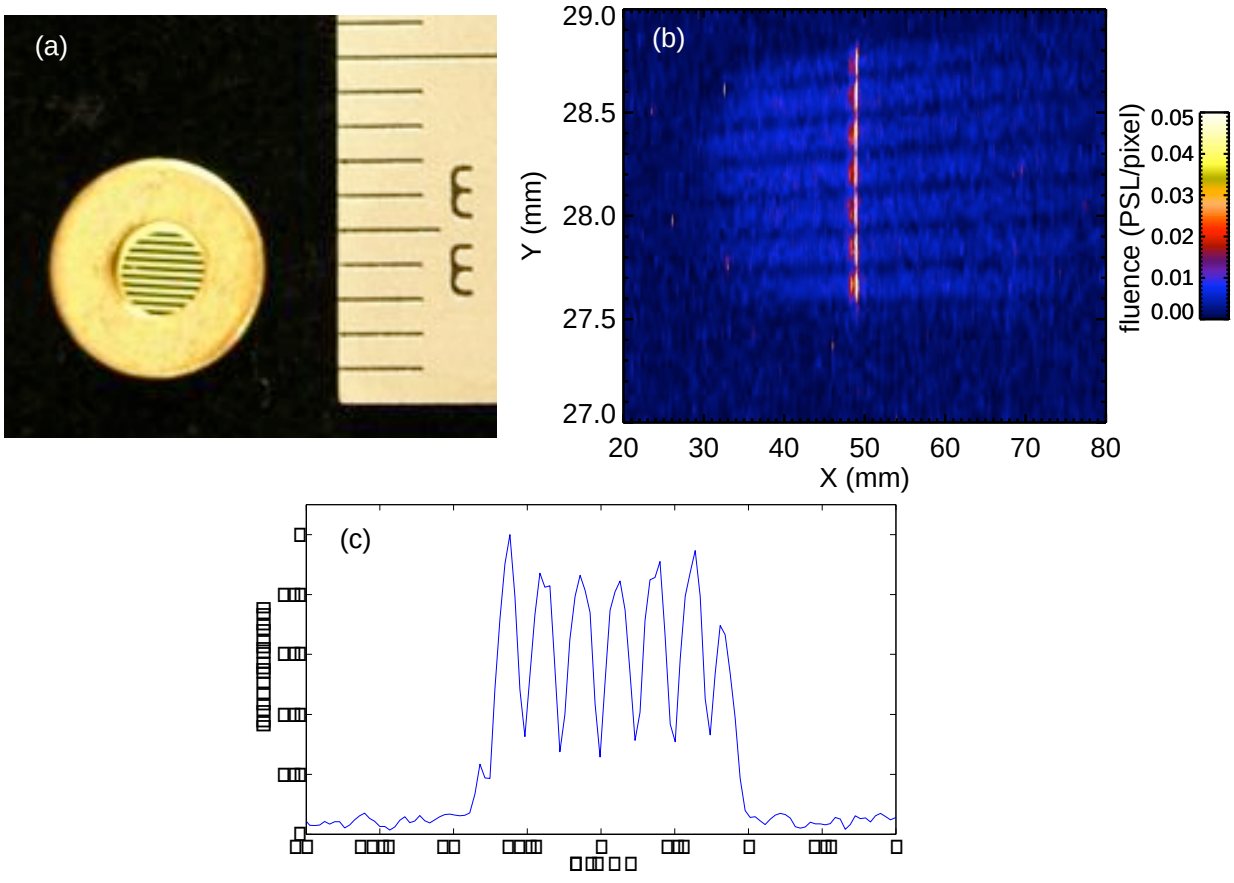

Figure 4.16. (a) Array of 65 µm thick Au wires vertically spaced with 180 µm wide gaps, (b) IP x-ray image of Mn spectra measured with spherically bent quartz 20-23, (QU-20-23-IN), and (b) the spatial lineout along the Mn-K-α_1 spectral line.

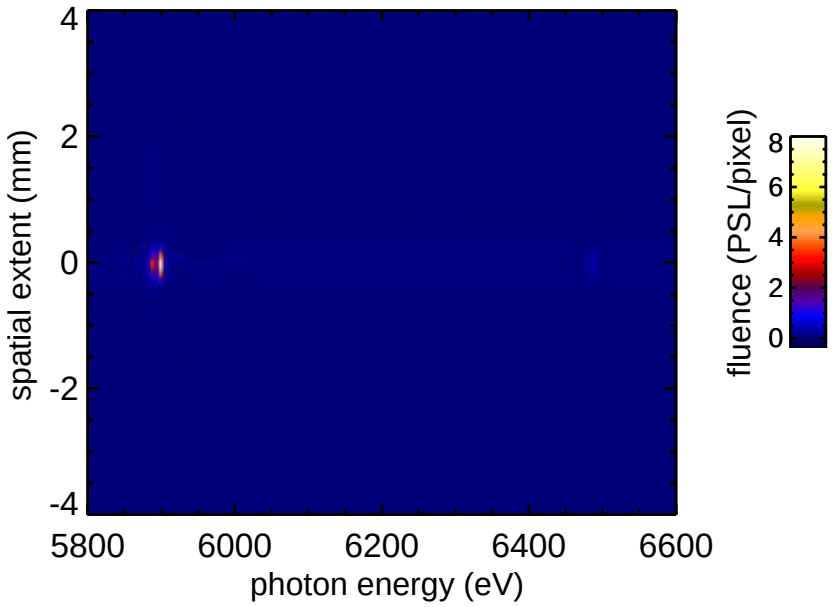

Figure 4.17. IP x-ray image of Mn spectra measured with spherically bent quartz 20-23, two crystals vertically tiled (QU-20-23-IN-VT).

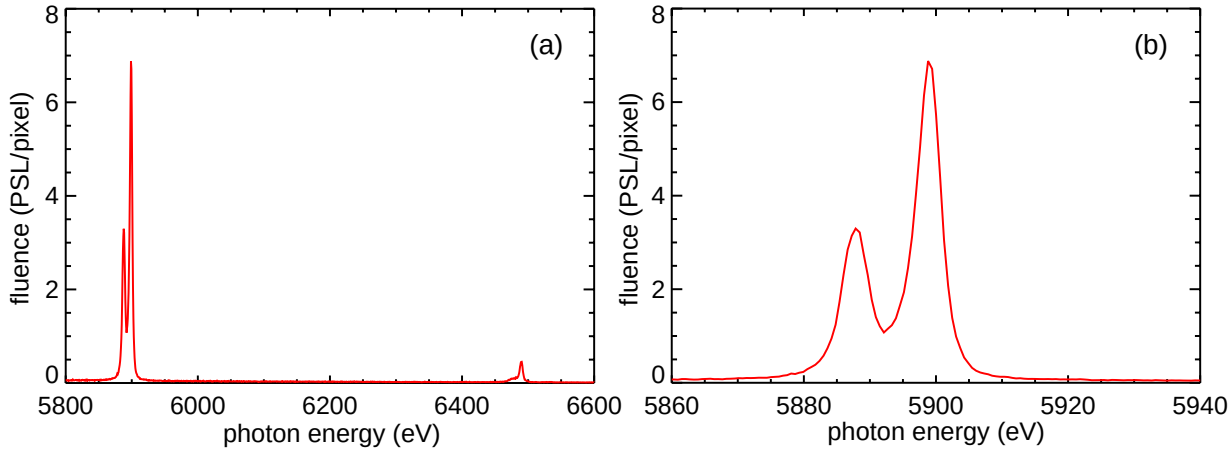

Figure 4.18. Mn spectra measured with spherically bent quartz 20-23, two crystals vertically tiled (QU-20-23-IN-VT): (a) wide range, (b) detailed view of K-α_1 and K-α_2.

The IP x-ray image of the Mn spectra measured with the QU20-23-EC-HT crystal is shown in Fig. 4.19, and the spectral lineouts are shown in Fig. 4.20. The gap between the horizontally time crystals is noticeable under close examination of the x-ray image (Fig. 4.19(b)), which would undesirable if a spectral line of interest happens to be located near it. Nonetheless, the QU20-23-EC-HT crystals produce similar results as the single crystal ($IP_{spectral}$ = 0.166 mm, $IP_{spatial}$ = 0.192 mm, $E/\Delta E$ = 1460). The spectral range is smaller ($E_{max} - E_{min}$ = [6905 – 5685]

eV = 1220 eV) because QU20-23-EC-HT is only 50 mm long, while its x-ray collection efficiency (I_P = 3.10 PSL/pixel, η = 1.9, η_w = 2.9%) was also similar to the QU20-23-IN crystal.

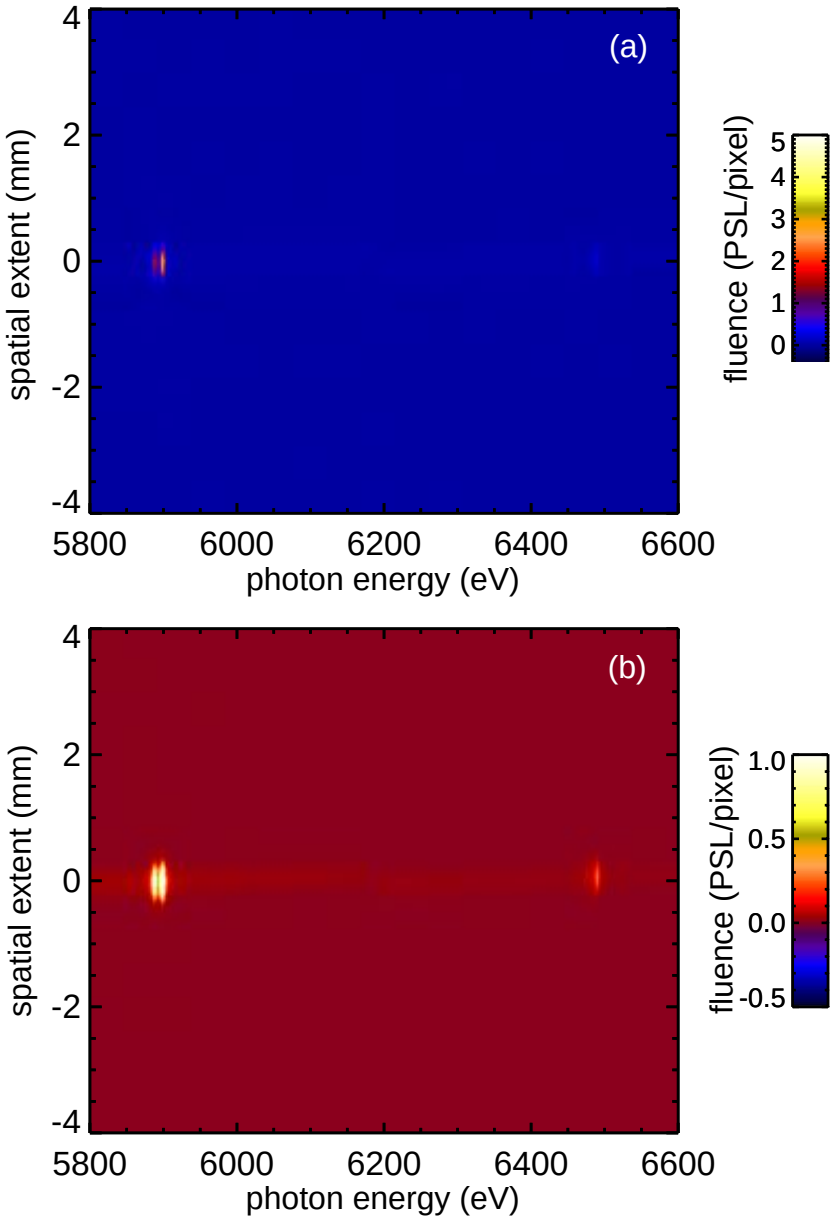

Figure 4.19. IP x-ray image of Mn spectra measured with spherically bent quartz 20-23, two crystals horizontally tiled (QU-20-23-EC-HT): (a) full range of fluence, and (b) lower range of fluence to enhance discontinuity in spectra.

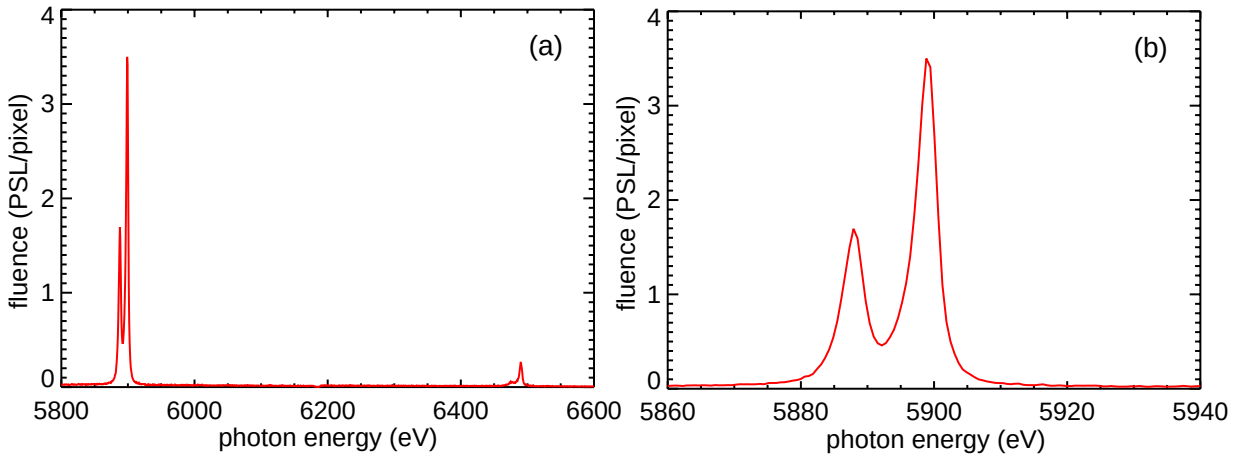

Figure 4.20. Mn spectra measured with spherically bent quartz 20-23, two crystals horizontally tiled (QU-20-23-EC-HT): (a) wide range, (b) detailed view of K-α_1 and K-α_2.

4.4.3. Mica

Previously, mica crystals have been examined for use in a FSSR diagnostic [49]. Two different thin (< 100 μm thick) mica I crystals were examined; one taken from the inventory of Ref. [49] (MICA-FS), and one obtained from Ecopulse (MICA-EC-VT), as shown in Fig. 4.21. MICA-FS was a single mica crystal 48 mm long by 15 mm wide, while MICA-EC-VT was two vertically tiled crystals with a overall size of 50 mm long by 36 mm wide. For both mica crystals, the Mn spectra were measured with a source-to-crystal distance of 300 mm (7st order reflection, 2d = 19.915 Å, θ = 46°).

The IP x-ray image of the Mn spectra measured with the MICA-FS single crystal is shown in Fig. 4.22, and the spectral lineouts are shown in Fig. 4.23. The MICA-FS single crystal produced similar results as the QU20-23-IN single crystal ($IP_{spectral}$ = 0.186 mm, $IP_{spatial}$ = 0.181 mm, $E/\Delta E$ = 1425, $E_{max} - E_{min}$ = [6745 – 5550] eV = 1195 eV). However, because mica was used in such a high order of reflection, the x-ray collection efficiency was considerably decreased (I_P = 0.57 PSL/pixel, η = 0.3, η_w = 0.5%). The IP x-ray image of the Mn spectra measured with the MICA-EC-VT vertically tiled crystal is shown in Fig. 4.24, and the spectral lineouts are shown in Fig. 4.25. In this case, the quality of measured Mn spectra was less than expected ($IP_{spectral}$ = 0.239 mm, $IP_{spatial}$ = 0.756 mm, $E/\Delta E$ = 1115, $E_{max} - E_{min}$ = [6700 – 5540] eV = 1195 eV) due to poor quality mica and/or the imprecise vertically tiling. Similarly, the x-ray collection efficiency was less than desired (I_P = 0.31 PSL/pixel, η = 0.8, η_w = 0.57%).

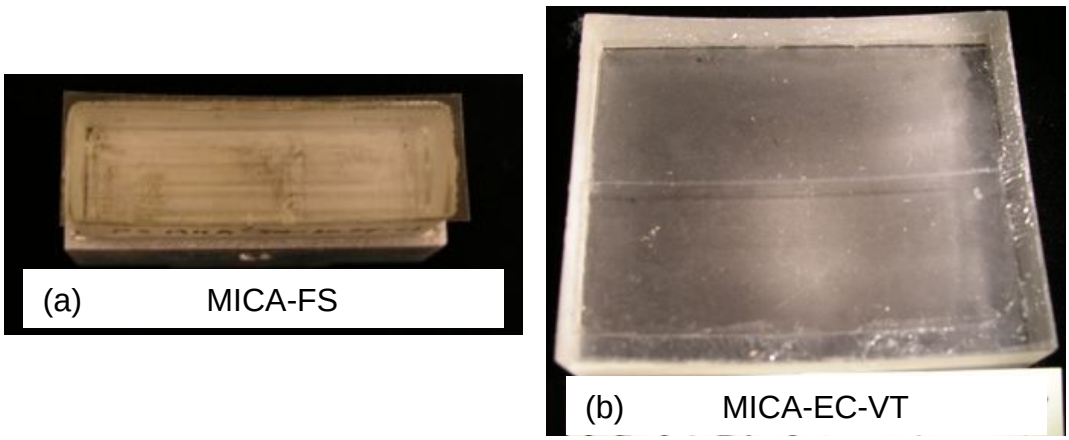

Figure 4.21. Spherically bent mica crystals on BK7 glass substrates: (a) single crystal (FS), (b) two vertically tiled crystals (Ecopulse).

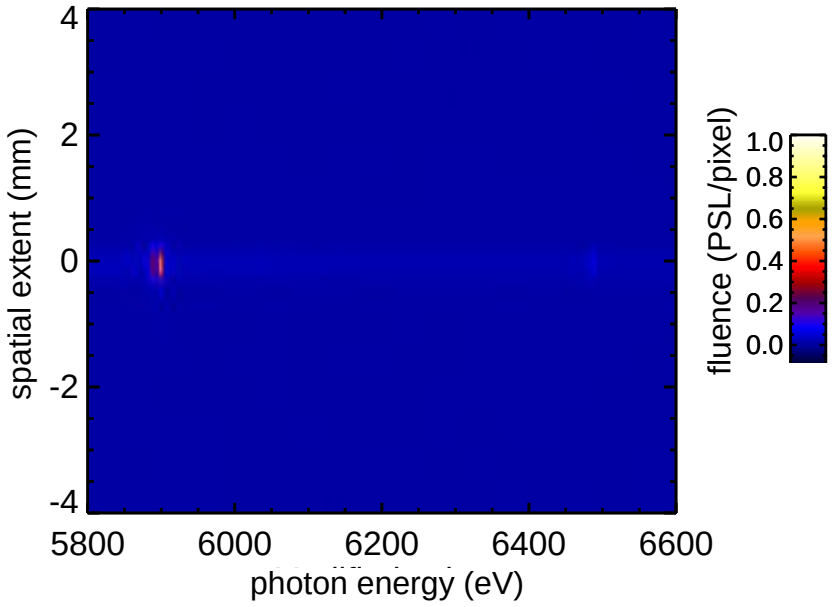

Figure 4.22. IP x-ray image of Mn spectra measured with spherically bent mica single crystal (MICA-FS).

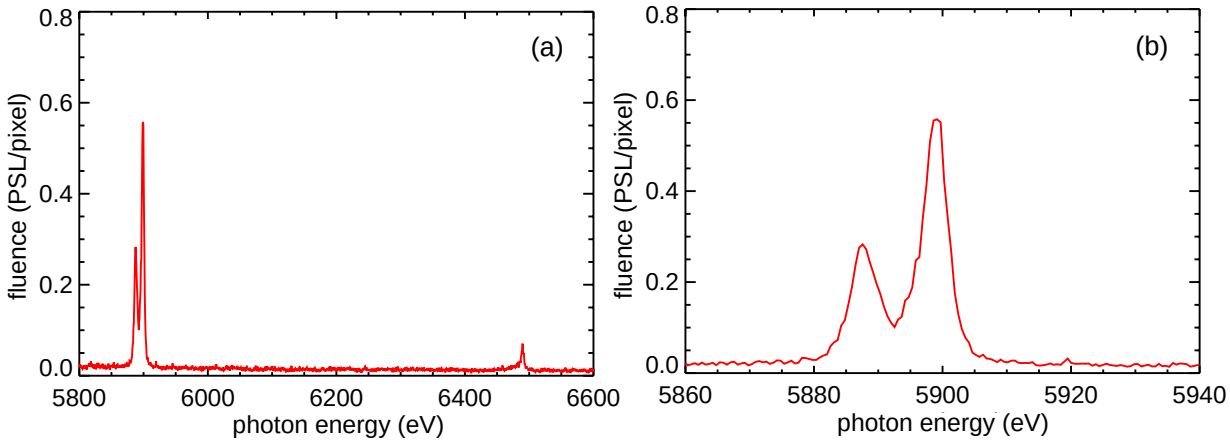

Figure 4.23. Mn spectra measured with spherically bent mica single crystal (MICA-FS). (a) wide range, (b) detailed view of K-α_1 and K-α_2.

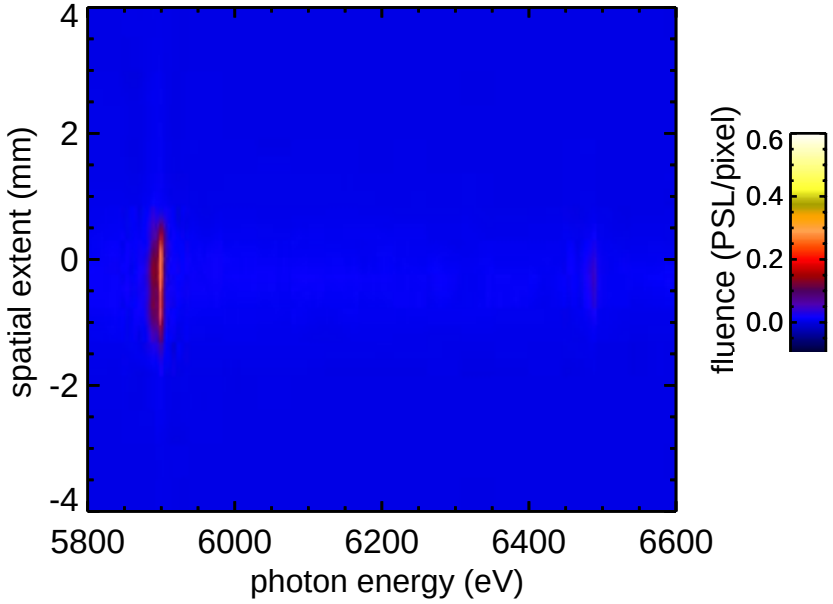

Figure 4.24. IP x-ray image of Mn spectra measured with spherically bent mica, two vertically tiled crystals (MICA-EC-VT).

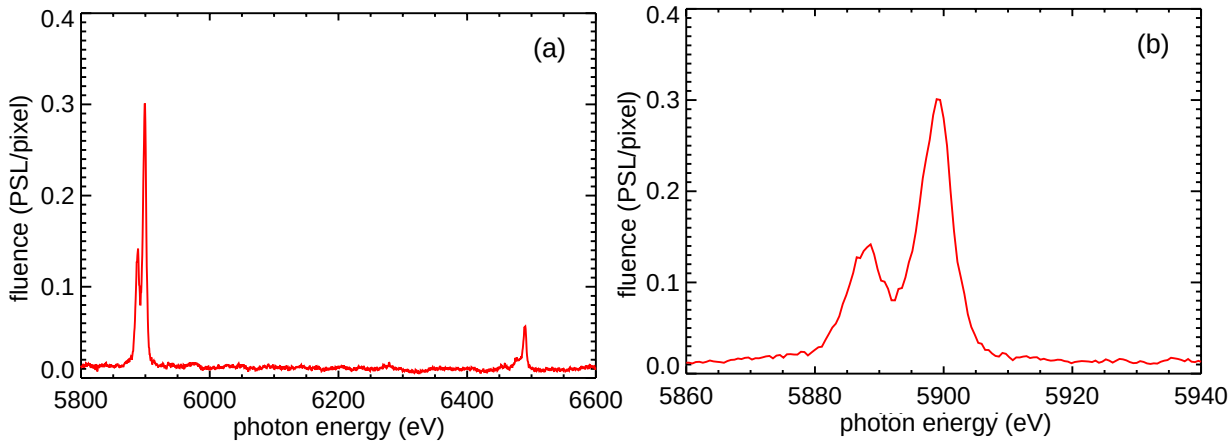

Figure 4.25. Mn spectra measured with spherically bent mica, two vertically tiled crystals (MICA-EC-VT): (a) wide range, (b) detailed view of K-α_1 and K-α_2.

4.4.4. Germanium

Spherically bent germanium 422 and 220 crystals (< 100 μm thick) were obtained from Inrad, each crystal was 50 mm long by 10 mm wide and bent onto a BK7 glass substrate that was spherically polished to a radius of curvature of 150 mm, as shown in Fig. 4.26. For the germanium 422 crystal (GE422-IN), the Mn spectra were measured with a source-to-crystal distance of 300 mm (1st order reflection, $2d$ = 2.310 Å, θ = 64°). The IP x-ray image of the Mn spectra measured with GE422-IN is shown in Fig. 4.27, and the spectral lineouts are shown in Fig. 4.28. It produced similar results as QU20-23-IN ($IP_{spectral}$ = 0.142 mm, $IP_{spatial}$ = 0.200 mm, $E/\Delta E$ = 1385), but smaller spectral range ($E_{max} - E_{min}$ = [6120 – 5650] eV = 470 eV). However, its x-ray collection efficiency was considerably higher (I_P = 14.63 PSL/pixel, η = 4.5, η_w = 13.5%).

For the germanium 220 crystal (GE200-IN), the Mn spectra were measured with a source-to-crystal distance of 300 mm (1st order reflection, $2d$ = 4.000 Å, θ = 31°). The IP x-ray image of the Mn spectra measured with GE220-IN is shown in Fig. 4.29, and the spectral lineouts are shown in Fig. 4.30. It produced slightly poorer results than GE422-IN ($IP_{spectral}$ = 0.676 mm, $IP_{spatial}$ = 0.418 mm, $E/\Delta E$ = 1285), but had a much larger spectral range ($E_{max} - E_{min}$ = [6410 – 4905] eV = 1505 eV). Its x-ray collection efficiency was also lower than GE422-IN (I_P = 0.79 PSL/pixel, η = 2.1, η_w = 6.3%).

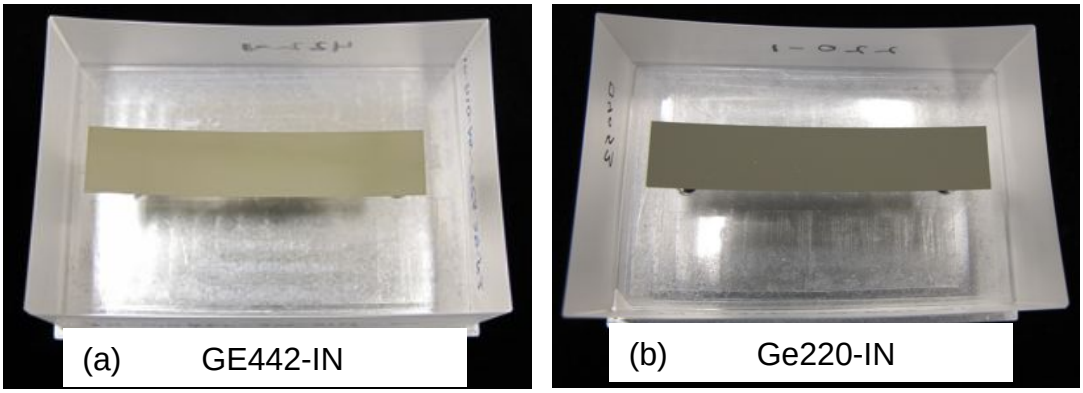

Figure 4.26. Spherically bent germanium crystals on BK7 glass substrates: (a) single crystal 422 (Inrad), (b) single crystal 220 (Inrad).

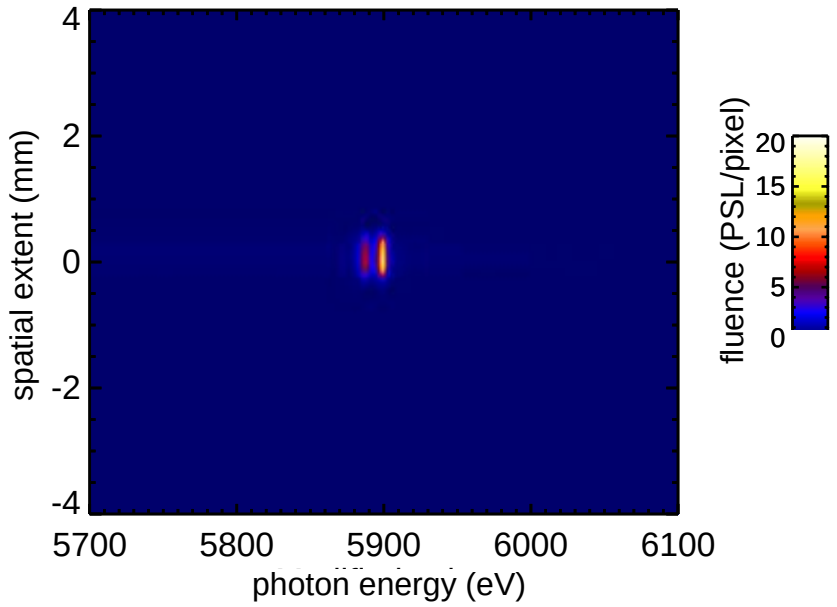

Figure 4.27. IP x-ray image of Mn spectra measured with spherically bent germanium 422 crystal (GE422-IN).

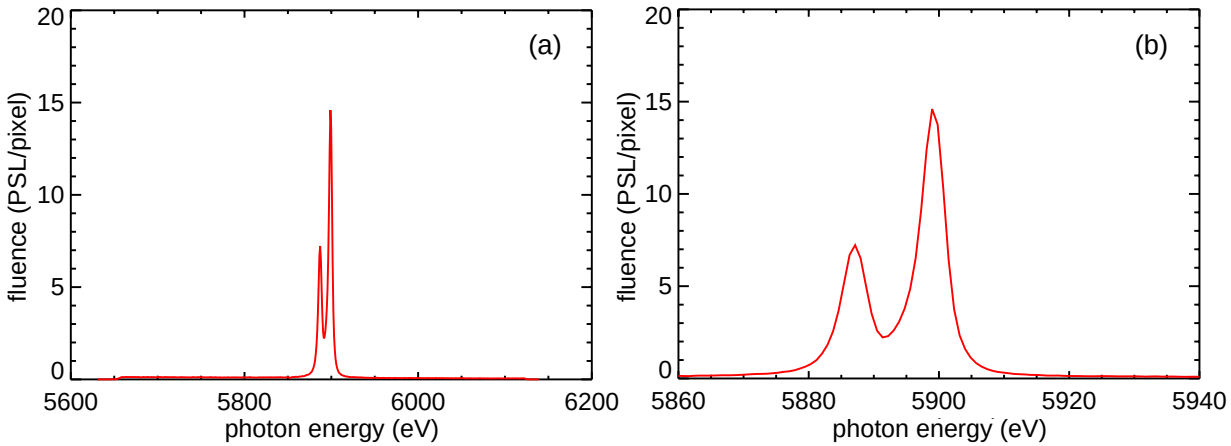

Figure 4.28. Mn spectra measured with spherically bent germanium 422 crystal (GE422-IN): (a) wide range, (b) detailed view of K-α_1 and K-α_2.

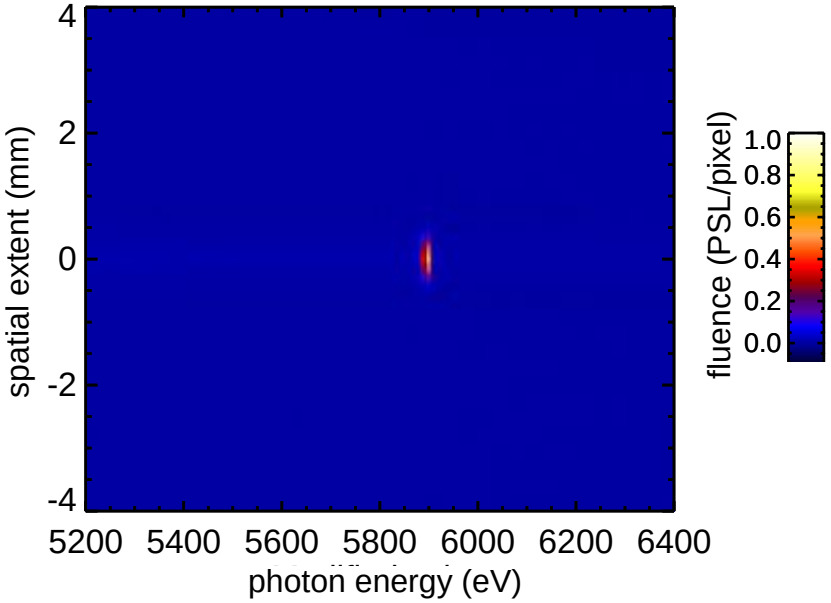

Figure 4.29. IP x-ray image of Mn spectra measured with spherically bent germanium 220 crystal (GE220-IN).

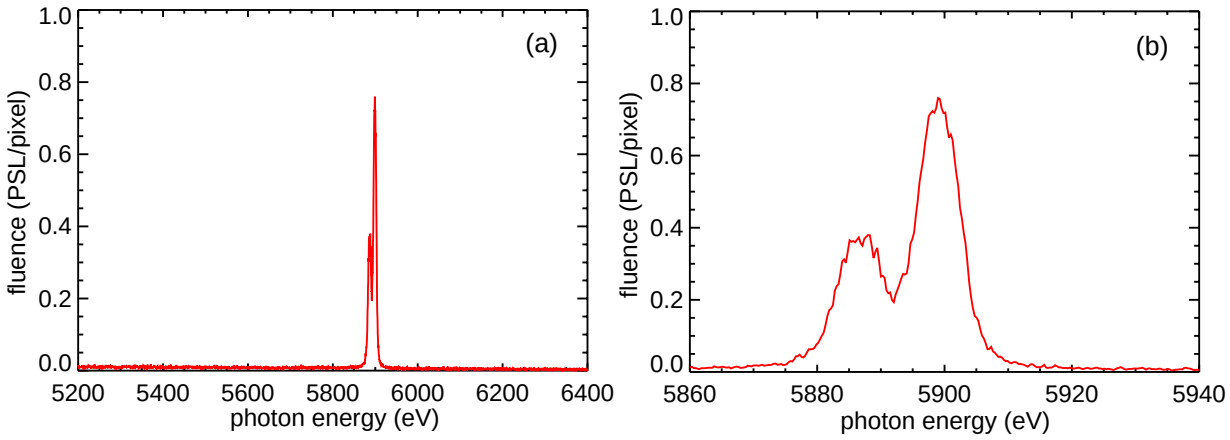

Figure 4.30. Mn spectra measured with spherically bent germanium 220 crystal (GE220-IN): (a) wide range, (b) detailed view of K-α_1 and K-α_2.

This page intentionally left blank.

5. X-RAY SOURCE

5.1. Overview

Experimental x-ray spectra from laser heated Ti, V, and Mn foils are presented. These metal foils were irradiated with the Z Beamlet laser, which provided 1kJ (2ω, lambda = 526 nm) at an irradiance of 2×10^{15} W/cm^2 on target. The spectra were collected at two different viewing angles simultaneously with two spatially resolved, time integrated spectrometers that used spherically bent quartz crystals. These experiments are motivated by the need to understand the variation of the spectra as a function of angle, and to optimize the brightness of various spectral lines. Here the following lines were examined: Ti He-β (5586 eV), V He-β (6117 eV) and Mn He-α (6181 eV). The density and temperature of the emitting plasma for each foil was determined by fitting the experimental spectra to simulated spectra produced from the collisional-radiative spectral analysis codes SPECT3D and PrismSPECT. In addition, HYDRA simulations were post processed with SPECT3D in order to resolve the temperature and density gradients in the plasma.

5.2. Motivation

A new spectrometer is being developed at Sandia National Laboratory for use in the Z machine. This spectrometer is intended to diagnose Warm Dense Matter targets using x-ray Thomson scattering (XRTS). The spectrometer uses the FSSR-2D geometry with a spherically bent quartz crystal. This type of spectrometer provides spatially resolved spectra along one direction of the target. With spatial resolution we hope to resolve temperature and density gradients that exist in the target plasma. In this type of scattering experiment an x-ray source is required to probe the target while a spectrometer collects scattered x-rays. The scattered x-ray spectrum contains information about the state of the plasma and perhaps detailed atomic physics if high signal-to-noise ratios can be achieved.

However, due to the small scattering cross-section the scattered signal is weak in most experiments. Thus, in preparation for future XRTS experiments we have begun dedicated experiments to optimize the brightness of the x-ray probe as well as understand the brightness variations that result from viewing the x-ray source at different angles (see Table 5.1).

5.3. Experimental Setup

The experiments presented here were performed with the Z Beamlet Laser at Sandia National Laboratory [45]. In standard operation the laser provides 1.2 kJ of green light (2ω, λ = 0.527 μm) from a single beamline in two separate pulses. The first pulse is called the pre-pulse, and the second is called the main pulse. The pre-pulse arrives on target before the main pulse. Both pulses are focused with an f/6.7 lens to a spot diameter of 150 μm on target. The pre-pulse nominally contained 200 J leaving the remaining energy in the main pulse. The main and pre-pulse durations were nominally 0.5 ns and 1 ns FWHM respectively. The estimated pre-pulse and main pulse irradiances were 2×10^{15} W/cm^2 and 5×10^{15} W/cm^2 respectively. In addition 3

other laser pulse configurations were tried. In Table 5.2, the nominal values for all 4 pulse configurations are listed.

A series of experiments of was preformed in which thin metal foils were irradiated with Z Beamlet. Most of the experiments were dedicated to understanding the x-ray emission from Mn foils that were either 5 or 25 μm thick. However, Ti, V, and Ni were also shot. Two spectrometers were used to simultaneously collect spectra at two different viewing angles. In addition a pinhole camera recorded an image of the emitting plasma. A variety of spectrometer configurations were developed in order to examine the various spectral lines from the foils. Table 4.1 and Table 5.1 provide a complete list of all the configurations that we fabricated and tested. Some of the configurations were designed for use on a bench top K-α source (Manson Model 5 Multi-Anode Ultra-soft x-ray Source). All of the configurations used Fuji TR image plate and a spherically bent crystal (radius of curvature R = 150 mm). The image plates were scanned by a Fuji BAS-5000 using a 25 μm pixel size. The scanning time was 45 ± 5 minutes after the shot for all experiments. Configuration III was determined to be the best configuration for scattering experiments with a Mn source since it produced the most intense x-ray image at the detector. In this configuration the image plate is located on the Rowland Circle. This particular geometry has been described previously and is sometimes referred as an FSSR-1D geometry [39].

The targets were fabricated from 5 and 25 μm thick foils that were purchased from Goodfellow. The Mn foils were not free standing. Due to the brittleness of these foils Goodfellow applies an adhesive to the foil and then hot presses the Mn onto a sheet of 100 μm thick polyester. The overall foil thickness including the adhesive and polyester is ~150 μm. All other foils did not have a polyester backing. The foils were laser cut by General Atomics into 2 mm diameter discs. The discs were glued to the tip of a 0.5 diameter glass pipet.

Table 5.1. Five spectrometer configurations that were developed for the ZBL source experiments. All configurations used spherically bent crystals with *R* = 150 mm..

Config.	Spectral Line	Energy (eV)	Crystal	2d (Å)	Crystal Length (mm)	Crystal Width (mm)	Central Bragg Angle (°)	Range (eV)	Source Distance (mm)	Comments
I	Mn He-α	6181	Qu20-23	2.749	60	18	46	5775-6910	200	FSSR-2D
I	Mn He-α	6181	Ge422	2.31	50	10	59.5	6025-6459	200	FSSR-2D
III	Mn He-α	6181	Ge422	2.31	50	10	60.27	5922-6508	256	FSSR-1D
IV	Ni He-α	7268	Mica 9th	2.204	50	35	46	7296-8014	200	FSSR-2D
V	Ti He-β	5581	Qu20-23	2.749	60	18	53.9	5287-5767	200	FSSR-2D

5.4. Experimental Results

First we investigated the state of the emitting plasma by fitting the experimental spectra to those produced by collisional-radiative simulations (PrismSPECT and Spect3D). This was done for each of the laser pulse configurations listed in Table 5.2. The objective is to develop an understanding that will allow us to optimize the x-ray emission. These experiments will be

referred to as the "source experiments." This leads into the second set of results from the cold scattering experiments where scattered spectra were collected using foam samples and a Mn He-α x-ray probe.

Table 5.2. Values for the 4 laser pulse configurations used for the ZBL experiments. The dead time refers to the elapsed time between the end of the pre-pulse and the start of the main pulse.

Pulse configuration	Main Pulse Energy & Duration	Pre-Pulse Energy & Duration	Dead Time
1	1 kJ, 1ns	0.2 kJ, 0.5 ns	1 ns
2	1 kJ, 1ns	None	NA
3	2 kJ, 2 ns	0.2 kJ, 0.5 ns	0.9 ns
4	2 kJ, 2 ns	None	NA

5.4.1. Mn source experiments

The source experiments used two spectrometer orientations. In one set of experiments the two spectrometers were position to view the foil disc at 90° (face-on) and 10° (side-on) with respect to the foil surface. In the other orientation, the 10° spectrometer was repositioned so that it looked directly into the rear of the foil (i.e., opposite of the laser drive side). See Fig. 5.1 for a schematic of the two different spectrometer orientations.

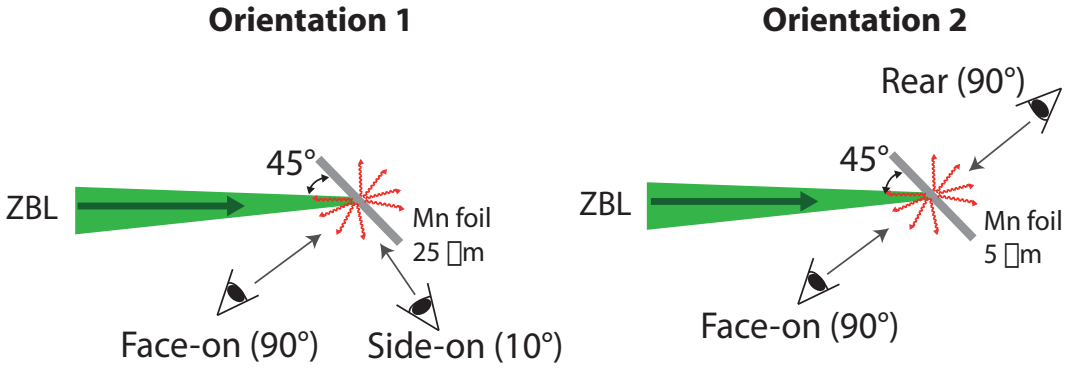

Figure 5.1. Illustration of the two spectrometer orientations used to collect spectra from a laser irradiated Mn foil. The angles indicated here are referenced from the foil surface.

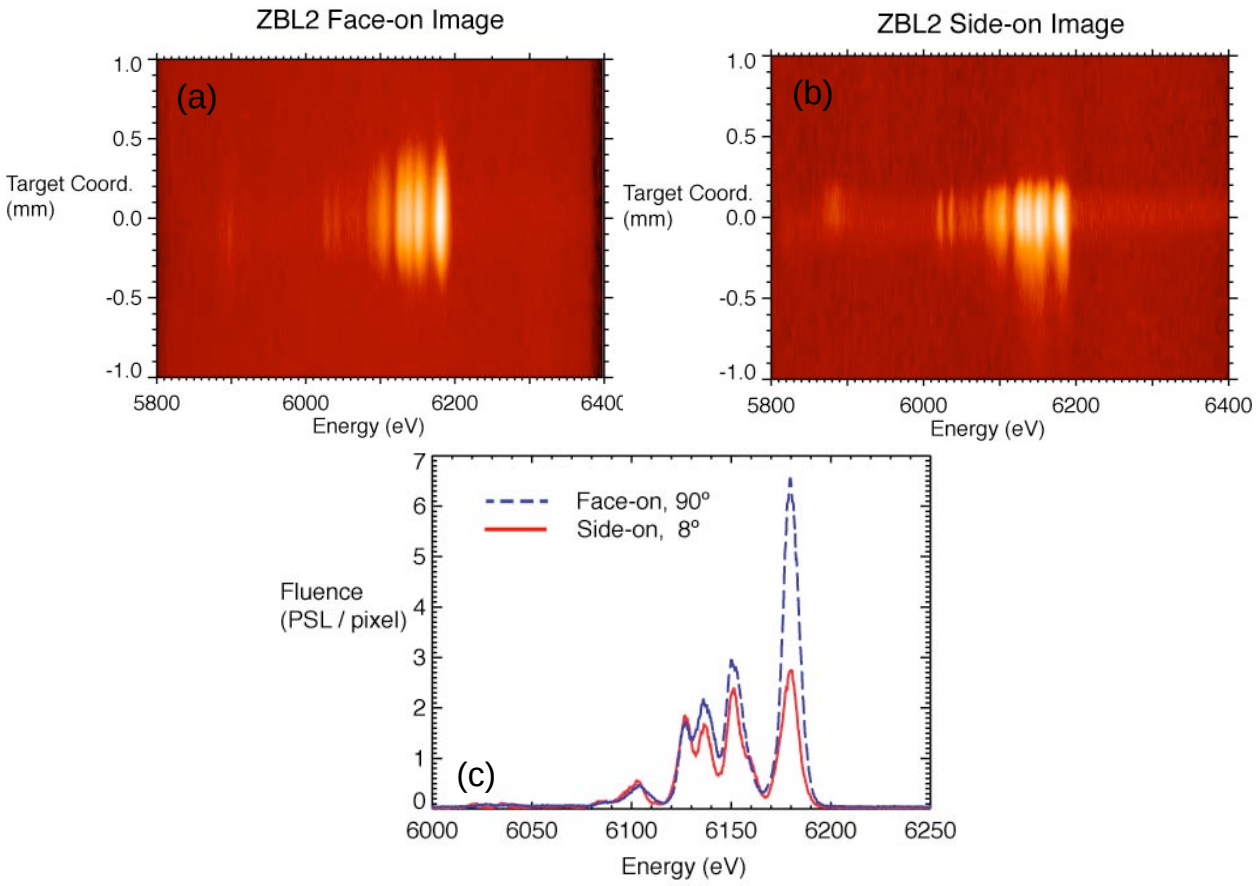

Figure 5.2. Data from a 25 μm Mn disk using spectrometer orientation 1. The spectrometer design was that listed as configuration I in Table 5.1. Note the lineouts are not corrected for filter transmission. (a) Face-on image. (b) Side-on image. Here the laser entered from the bottom of the image

Figure 5.2(a) and (b) shows the images that are recorded by the spectrometer using spectrometer configuration I as listed in Table 5.1. Figure 5.2(c) shows the measured spectra. The face-on and side-on views show spectra with different shape and peak brightness. The face-on and rear views show spectra with the same shape, but different peak brightness. In Fig. 5.3(a) PrismSPECT was used to fit the measured spectra from the face-on view. The simulations assumed a steady-state, Non-LTE plasma with $n_i = 6 \times 10^{18}$ ions/cm^{-3} and $T_e = 2.2$ keV. Although, the simulations appears to accurately reproduce the spectra, the simulated electron density was 1.4×10^{20} cm^{-3}, which is surprisingly ~3% of the critical density (4×10^{21} cm^{-3}). It is thought that the ratio between the He-α Resonance line and the Intercombination line provides a measure of n_i, while the ratio of the Resonance line and to nearest Li-like satellites provides a measure of T_e. Figure 5.3(b) and (c) shows multiple PrismSPECT simulations that demonstrate the effects on the Mn spectra when changing n_i and T_e are varied.

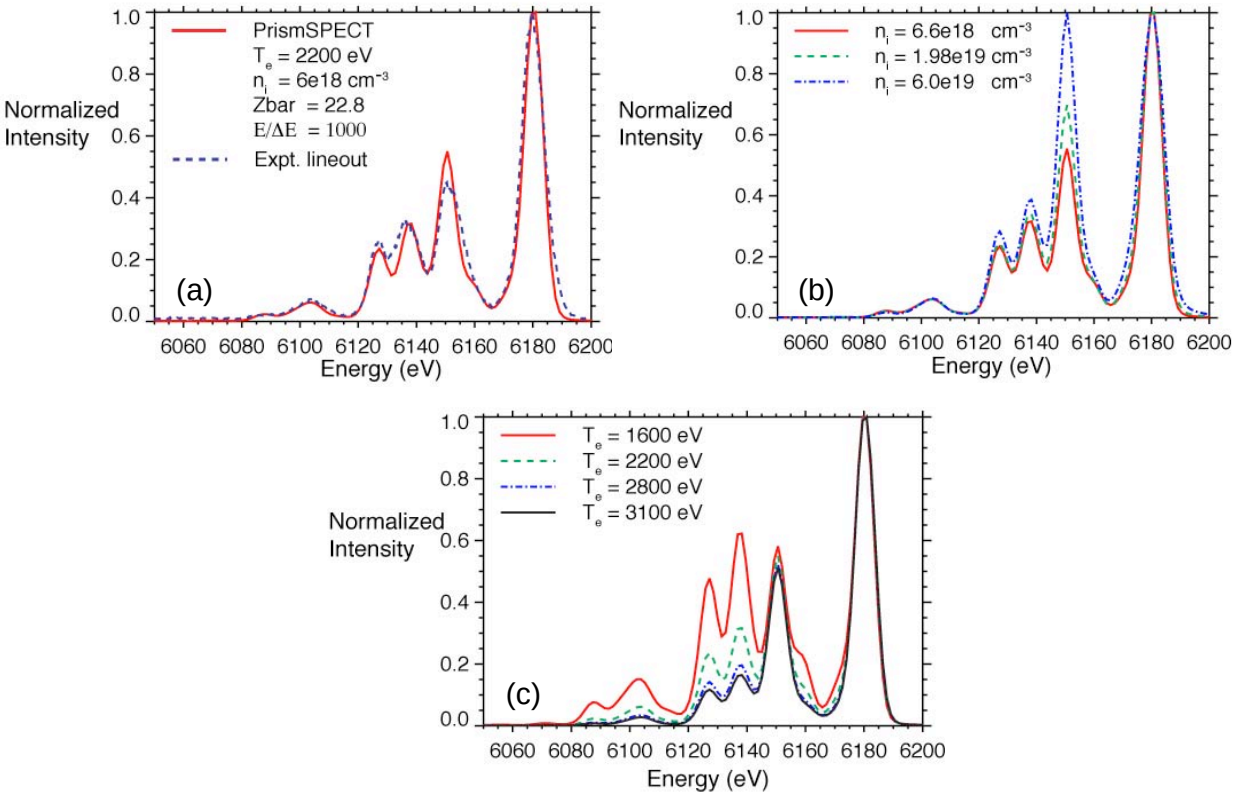

Figure 5.3. (a) Comparison of a PrismSPECT simulation with experimental spectra. (b) PrismSPECT simulation showing the relative intensity between the inter-combination line and the resonance line. Here T_e = 2.2 keV and a 200 μm thick plasma slab were used. (c) Same as (b) but T_e was varied and n_i was fixed at 6 × 10^{18} cm^{-3}.

SPECT3D simulations were also performed using n_i = 6 × 10^{18} cm^{-3} and T_e = 2.2 keV. Here again we assumed a uniform, Non-LTE plasma. The plasma was shaped as a disk that was 215 μm tall and 340 μm in diameter. These dimensions were the FWHM measurements of emitting plasma obtained from the experimental spectra. The comparison between the SPECT3D results and the measured spectra are shown in Fig. 5.4. The overall agreement is poor. Furthermore, the face-on view does not reproduce the PrismSPECT spectra. We are currently working to understand the source of this disagreement. We suspect there are temperature and density in the plasma that play important roles. Furthermore, the consequences of using a time-integrating detector must be evaluated. In other words, the plasma conditions are not steady-state and this may further confuse the interpretation of data. Thus, 2D and 3D HYDRA simulations are currently in progress. The output from HYDRA can be inserted into SPECT3D, which will then generated the simulated spectra.

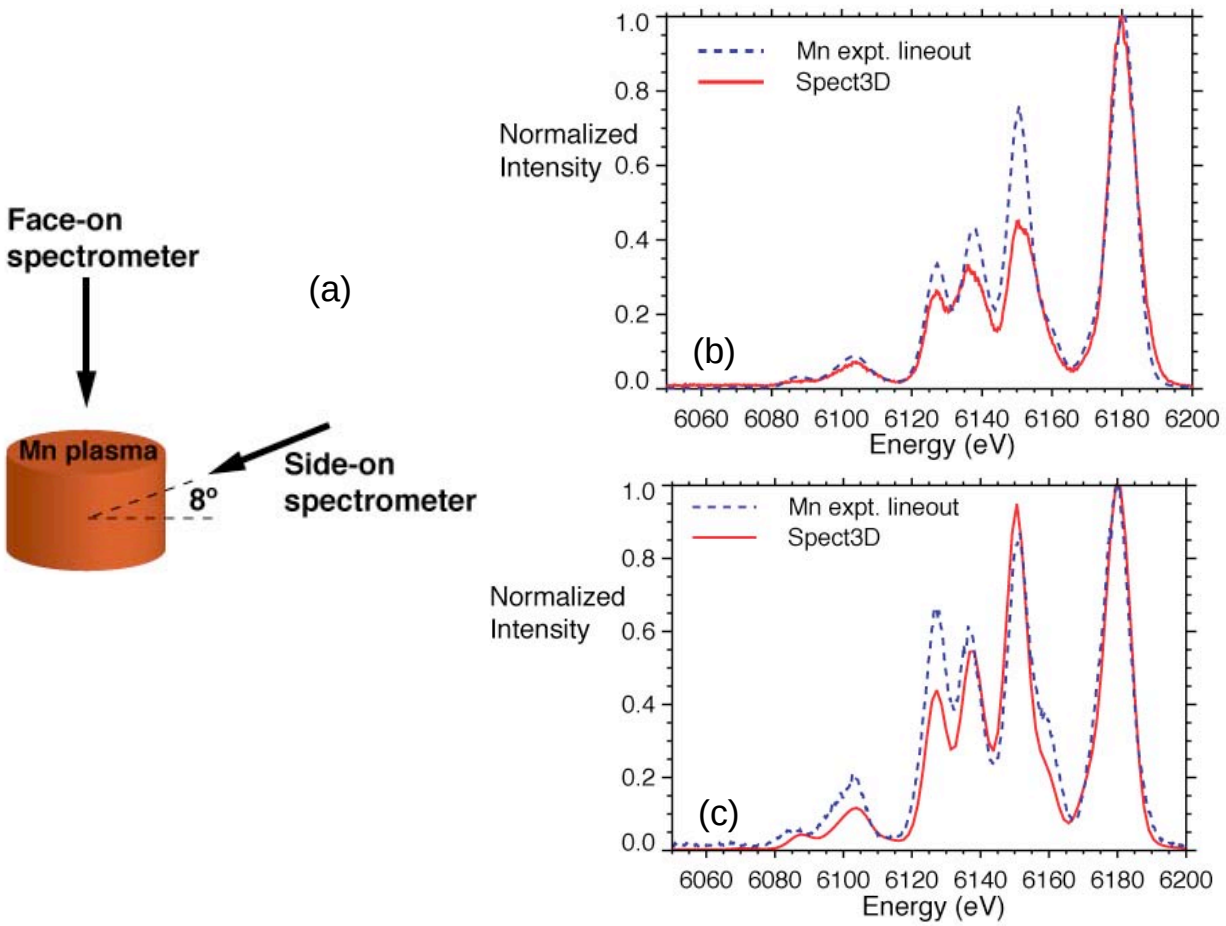

Figure 5.4. (a) Setup of Spect3D simulation. The plasma disc is 215 μm tall and 315 μm diameter. (b) Comparison of the face-on Spect3D simulation and experiment. (c) Comparison of the side-on Spect3D simulation and experiment. All intensities have been normalized to the He-α line.

5.4.2. Foam scattering experiments

In preparation for future Z experiments we have conducted several scattering experiments in the ZBL test chamber. The objective was to collect scattered x-rays from a room temperature sample using input x-rays from the Mn source that was discussed previously. TPX foam (CH_2) was the chosen target material due to its low atomic number and density. Thus the foam has a relatively long mean free path for the 6 keV Mn probe x-rays. This allows us to use a large foam sample, which in turn should be easily resolvable with even a coarse spatial resolution.

The setup for these experiments is shown in Fig. 5.5. Here the central scattering angle is 90°. The foam used in the experiments had densities of 0.24 and 0.46 g/cm^3. Spectrometer configuration III as listed in Table 5.1 was used to record the scattered x-rays from both foam densities. The full data image is shown in Fig. 5.6(a). The isolated spectrum located between the horizontal stripes on the left and the scattered signal on the far right is the source spectrum

that was produce near the surface of the Mn. The source spectrum is reproduced in the elastic scattering signal directly to the right. However, the scattered signal has a faint low energy tail. This is the inelastic scattering signal that originates from x-rays scattered by weakly bound electrons attached to the carbon atoms. The horizontal stripes are images of the laser ablated Mn plasma that extended beyond the Cu shields that are drawn in Fig. 5.5.

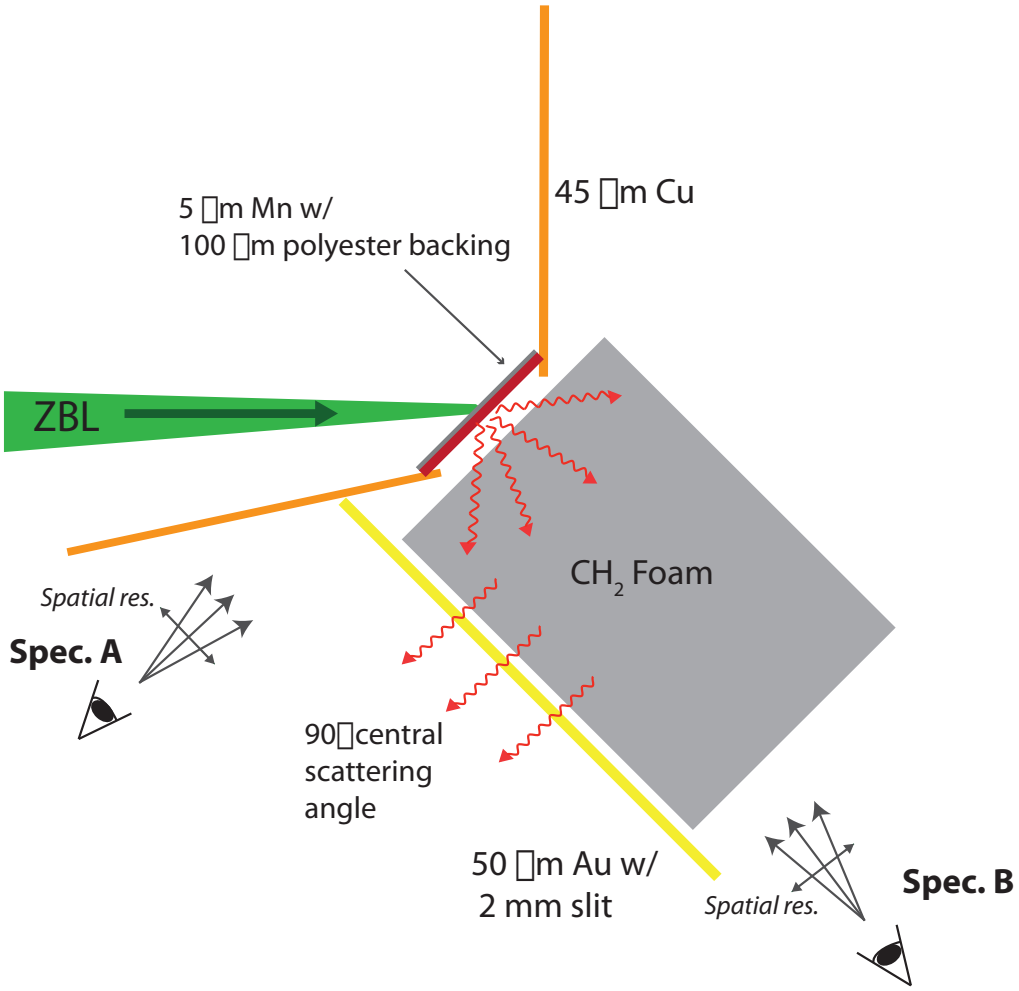

Figure 5.5. X-ray scattering experiment with room temperature TPX foam. Two identical spectrometers (Spec. A and Spec. B) were used to simultaneously observe the Mn source and the scattered signal.

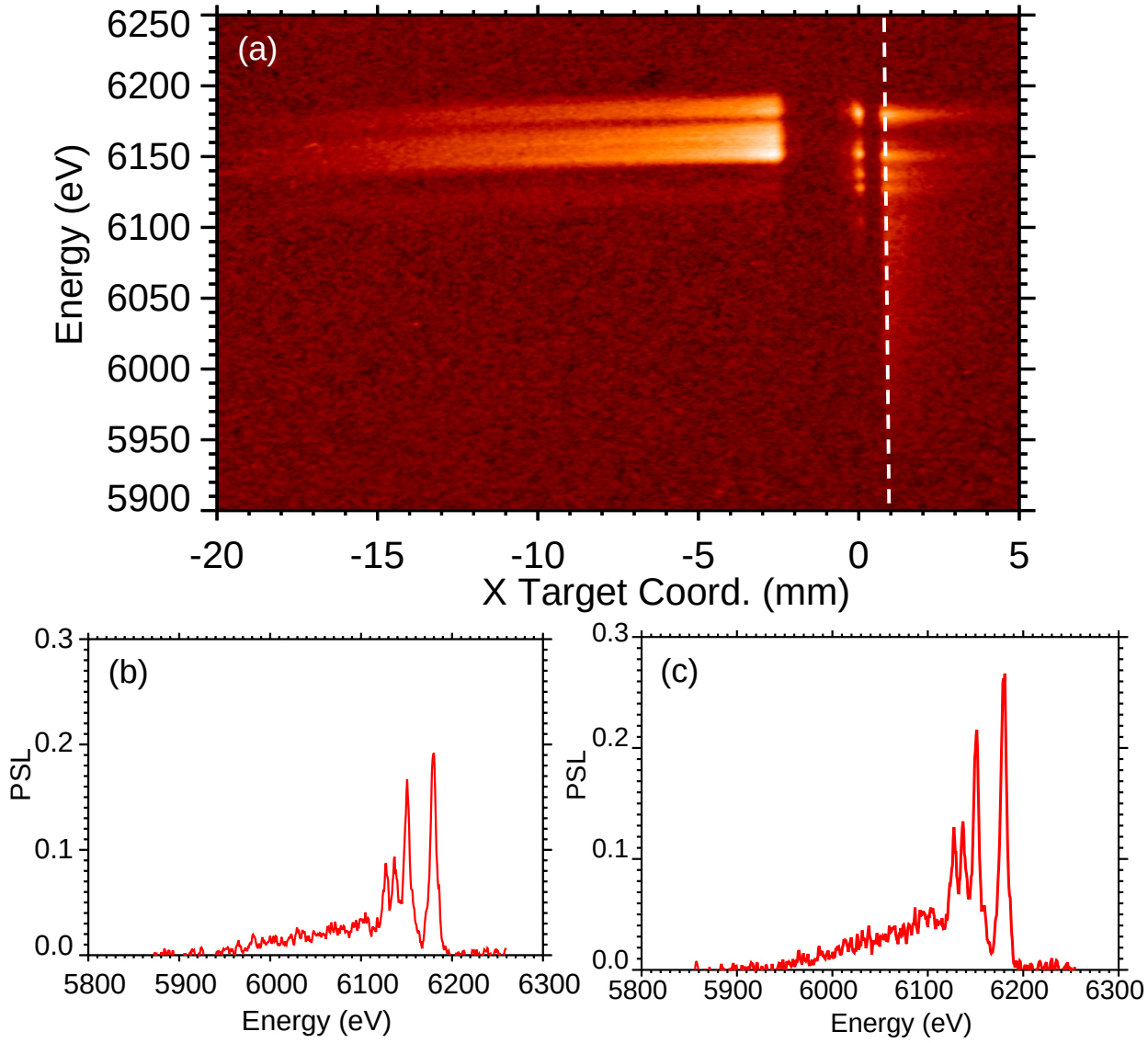

Figure 5.6. (a) Shown here is the full image obtained from a single experiment that used 0.24 g/cc TPX foam. Both elastic and inelastic scattering are seen in the far right of the image. The long tail to the left is the emission from the laser plasma plume. (b) This is a vertical lineout taken through the leading edge of the scattering signal seen above. (c) This is the same vertical lineout from an experiment that used 0.46 g/cc foam (not shown here).

6. Z EXPERIMENT DESIGN

6.1. Overview

This section describes the Z experiments scheduled for calendar year 2012. Design considerations for a future high impact x-ray scattering experiment are described in Section 7. The objective of the Z experiments is to obtain high quality x-ray scattered signal from a warm dense matter (WDM) state that would provide accurate and precise temperature, electron density, and ionization state information. The overall Z-XRTS experimental setup is shown in Fig. 6.1. Four scattering experiments on the Z-accelerator are planned for the 4th quarter of 2012 (two in November, and two in December). The goal of the November experiments is to demonstrate that we can collect scattered x-rays from a room temperature foam sample on Z. In the December experiments we will attempt to shock the foam using a magnetically launched flyer plate traveling at 16 km/s. Both of these experiments will require the new X-ray Scattering Spherical Spectrometer (XRS^3). The design of the spectrometer is similar that used in the ZBL scattering experiments. However, the crystal and image plate will be the housed in tungsten box in order to protect them from debris and background radiation. The walls of the box are 1 inch thick, which stop all x-rays below 400 keV. However, from 2 to 10 MeV the wall transmission is around 10%. The operating characteristics of the XRS^3 are listed in Table 6.1.

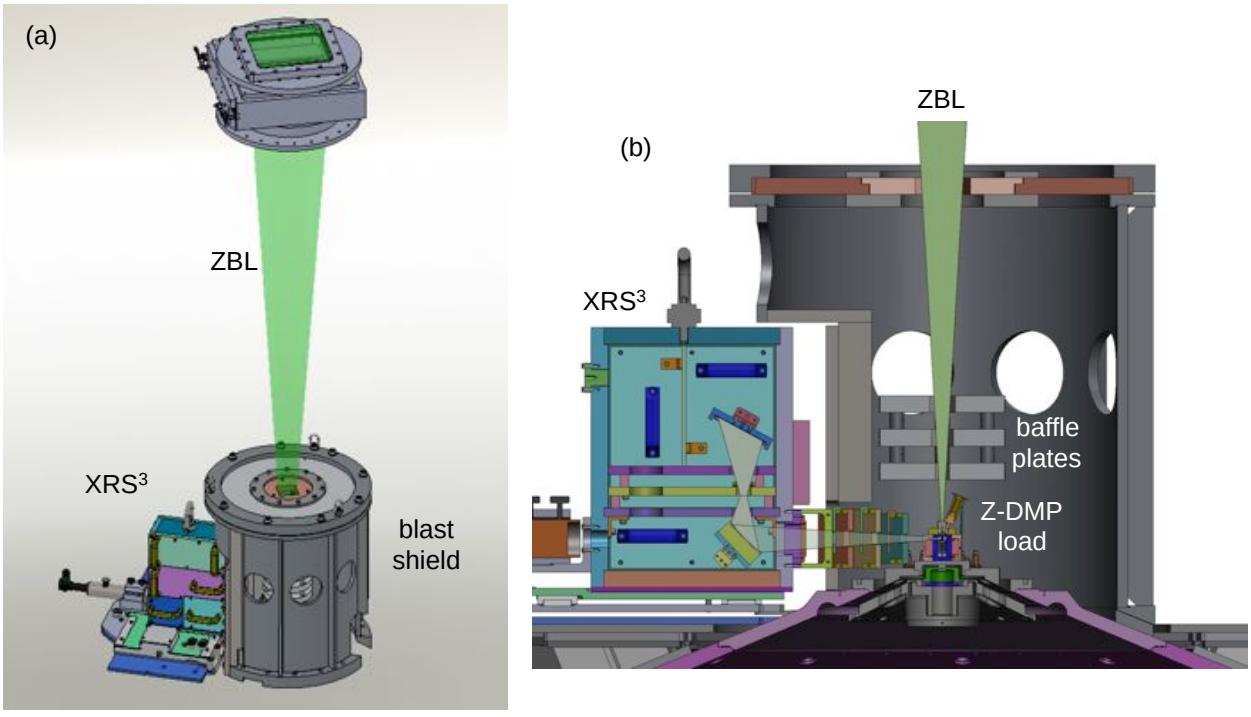

Figure 6.1. Z-XRTS experimental setup: (a) isometric view, and (b) cross-section view.

Table 6.1. List of operating characteristics of the XRS^3 as intended for use on the first Z-XRTS experiments. The collected photons number assumes a 1.5 mm thick cold TPX foam sample with a density of 0.1 g/cc.

XRS^3 Operating Characteristics	
Geometry	FSSR-1D
Probe x-rays	Mn He-α (6181 eV)
Crystal	Ge 422 (2d = 2.31 Å)
Calculated integrated reflectivity	0.046 mrad
Crystal size (meridional x sagittal)	60 x 20 mm
Central Bragg angle	60.27°
Crystal radius of curvature	216.5 mm
Source-to-crystal distance	370 mm
Crystal-to-detector distance	188 mm
Spatial magnification	0.508
Detector position	Rowland Circle
Energy range	480 eV (5960 – 6450 eV)
Dispersion at central Bragg angle	19.3 eV/mm
Active solid angle	3.5×10^{-6} sr
Spatial resolution with 2 mm tall slit	100 - 200 μm
Spectral resolution (E/ΔE)	1000
Estimated collected elastic photons	2×10^5

The target hardware that will be used for these first experiments can be seen in Fig. 6.2. Z will be used to magnetically launch flyers (15-30 km/s) to shock compress carbon samples (CH, CH_2 or CRF foams) up to pressures of 0.3–2 Mbar, and create the WDM states. The Z-Beamlet laser (ZBL) strikes a small Mn foil at a location that is 0.5 mm from the rear surface of foam sample and 1.25 mm from the center of the foam. The laser-irradiated foil will generate x-rays that enter into the foam. The x-rays scattered from the WDM will be collected with a high spectral and high spatial resolution x-ray scattering spherical spectrometer (XRS^3) and recorded onto image plate. A modified DMP blast shield will be fielded to mitigate load debris from damaging ZBL optics. The initial XRTS experiments on Z will be performed at low charge voltages to minimize the debris field. In succeeding XRTS experiments, the charge voltage will be increased to generate higher shock pressures. Carbon foam samples of various initial mass densities will be used to probe the effects of pressure ionization and continuum lowering in the shock compressed state. Material phase transitions and coexistence regimes will be investigated by shock loading beryllium samples.

6.2. Z-DMP Load

An overview of the magnetic loading technique for materials studies using pulsed power generators is given here, for more details see Refs. [10, 33-34]. In a Z-DMP coaxial load, two anode panels (north and south) are arranged around a central cathode stalk to form two anode-cathode (A-K) vacuum gaps, as shown in Fig. 6.2. The short circuit is created between the anode panels and the cathode post through a shorting cap at the top of the coaxial load. The current flowing on the anode and cathode produces a planar magnetic field between them, and the interaction between this field and the current results in a smooth mechanical stress wave that is proportional to the current squared. The impulsive pressure produced provides sufficient momentum to launch the anodes panels across a gap (1 mm) at a high velocity and impact load samples. The magnetically launched anode flyer plates reach velocities up to 30 km/s, which shock compress samples to pressures up to tens of Mbar.

In the Z-XRTS experiments, six total load samples, three on each anode panel, will be fielded. The XRTS diagnostic will be used on the top load sample of the south panel, and VISAR (velocimetry interferometer system for any reflector) and SVS (streaked visible spectroscopy) diagnostics will be fielded on the remaining load samples (Fig. 6.2(b)). In initial Z-XRTS experiments, XRTS load will be a 5 mm wide by 5 mm tall by 1.5 mm thick carbon foam sample. A thin Mn foil (5 μm thick) x-ray source will be placed near the carbon foam (Fig. 6.2(c)). During the Z shot, ZBL will irradiate the Mn foil to generate 6.181 keV (Mn-He-α) x-rays that will enter the front surface of the carbon foam. As the flyer plate shock compresses the carbon foam, x-rays will penetrate into it, scatter from the shock state and exit out the side perpendicular to the shock propagation (Fig. 6.2(d)).

Figure 6.3 present detail views of the XRTS load sample. Two x-ray source geometries had been experimentally evaluated in the ZBL calibration chamber (see Section 5.4.1): (1) a "reflection" geometry using x-rays from the Mn foil's front side foil, and (2) a "transmission" geometry using the x-rays from its rear side. For the Z-DMP experiment, an x-ray source transmission geometry where the Mn foil is set vertically at a 45° angle relative to the foam sample was chosen based on several experimental considerations. First, the transmission geometry allows easier alignment of the ZBL onto the Mn foil, as described in Section 6.5). Although x-rays have to pass through the thin Mn foil and so are slightly attenuated by about 50%, it allows the x-ray source to be situated closer to the sample than possible with the reflection geometry, which results in higher x-ray fluence into the sample. In addition, the transmission geometry avoids having the emission from the laser plume near the sample (see Fig. 5.6(a)).

The x-rays scattered from both the ambient and shock compressed states of the carbon foam sample, and direct x-rays from the x-ray source will be simultaneously collected by the XRS^3 spectrometer (Fig. 6.4). A tantalum exit aperture will allow x-ray scattering from only shock and ambient sample regions, and block scattering from other parts of the load hardware, and a copper filter will be used to attenuate the direct x-rays.

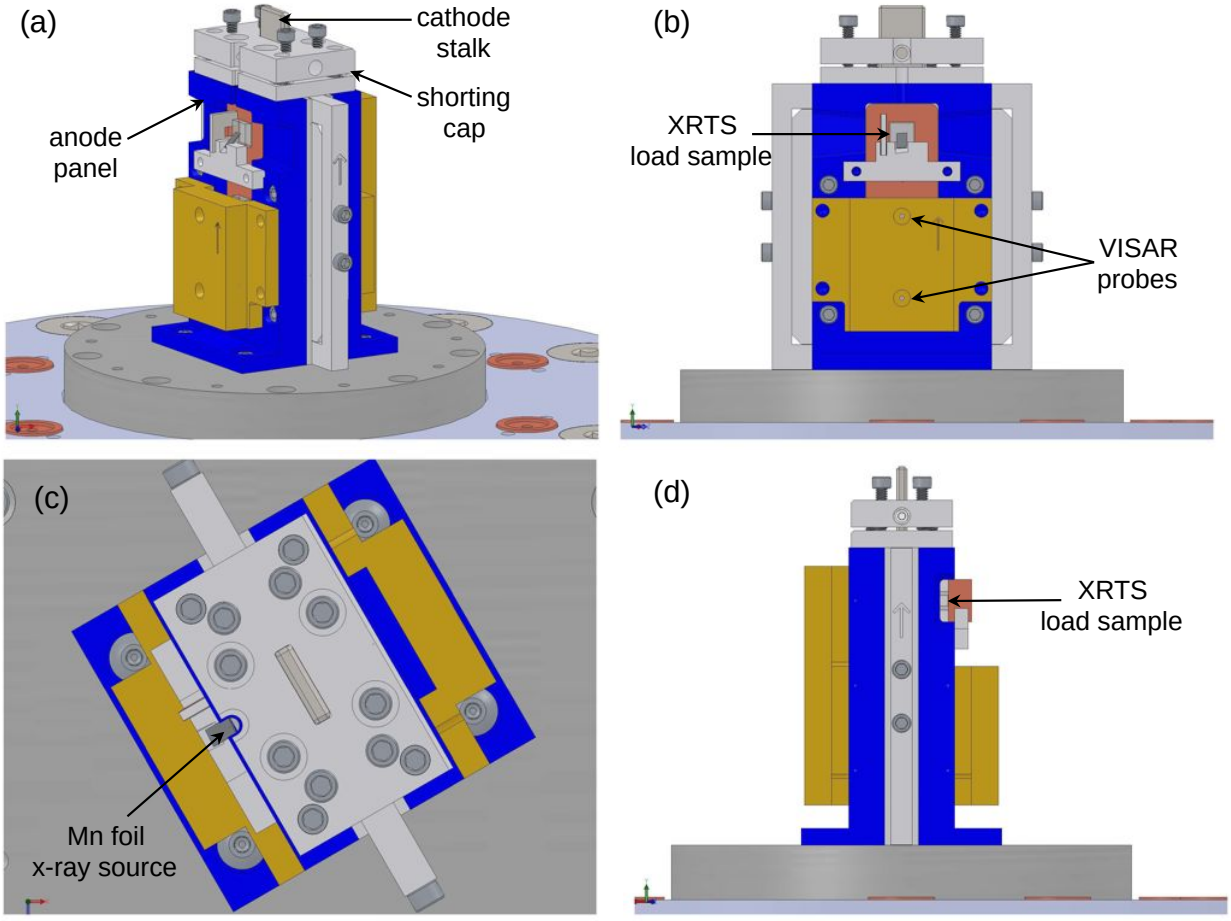

Figure 6.2. Z-DMP coaxial load: (a) isometric view, (b) front view, (c) top view, and (d) side view.

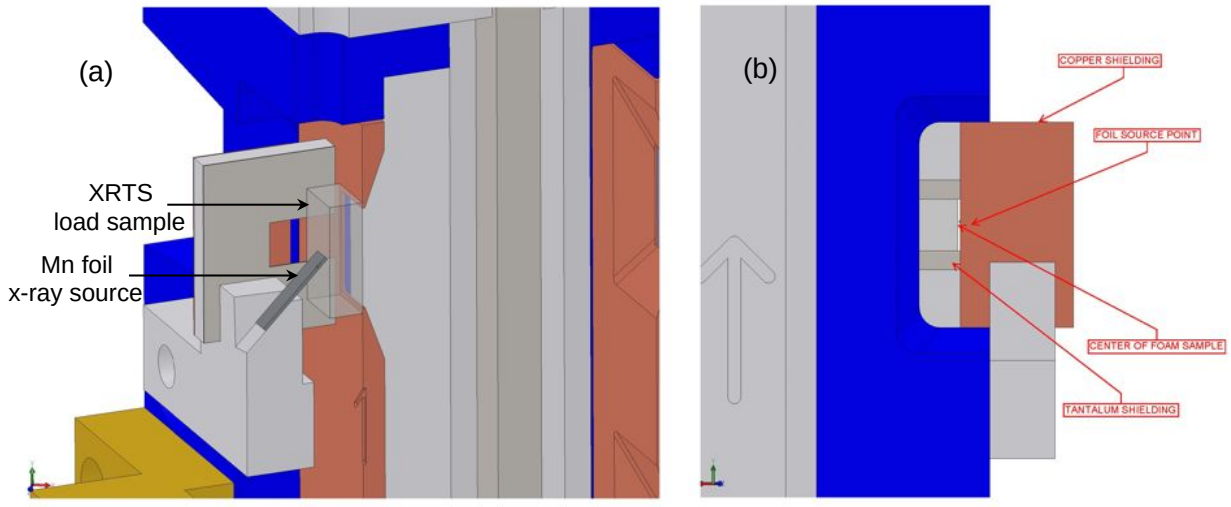

Figure 6.3. Detailed views of Z-DMP coaxial load: (a) isometric view, and (b) side view.

6.3. XRS^3 Spectrometer

With the XRS^3 spectrometer (Fig. 6.4), the x-rays will be both spectrally and spatially resolved by a spherically bent crystal, and recorded onto image plate (IP) that are housed within a box made of 1" thick tungsten. The XRS^3 spectrometer was designed to prevent damage to the crystal and IP from load debris, and shield x-ray background from Z interfering with the x-ray scattering signal recorded on the image plate. An entrance snout consisting of chevron (V-shape) plates is meant to deflect load debris from entering the XRS^3 spectrometer. Internally, there are 1" thick tungsten crossover plates to further reduce x-ray background by allowing only x-rays that are reflected off the crystal to reach the IP. The crossover plates also serve to further protect the IP for debris damage.

The XRS^3 spectrometer will sit on an alignment base that has 3-directional adjustments to allow precise positioning of it to the Z-DMP load target (Fig. 6.5). The entire XRS^3 assembly, weighing about 650 lbs. (spectrometer body: 490 lbs. and base: 160 lbs.), will be craned into the Z center section. Using an alignment attached to the front of the tungsten box, the XRS^3 spectrometer will be slid on bearings in the y-direction until the crystal-to-target distance is 370 mm with a tolerance of ± 2 mm. With the crystal removed, the alignment telescope will be used to horizontally (x-direction) and vertically (z-direction) locate the target center of the foam sample within a tolerance of ± 1 mm. A translational stage provides direct horizontal adjustment, but vertical movement of the XRS^3 spectrometer is accomplished indirectly by turning a large knob located at the back of the alignment base.

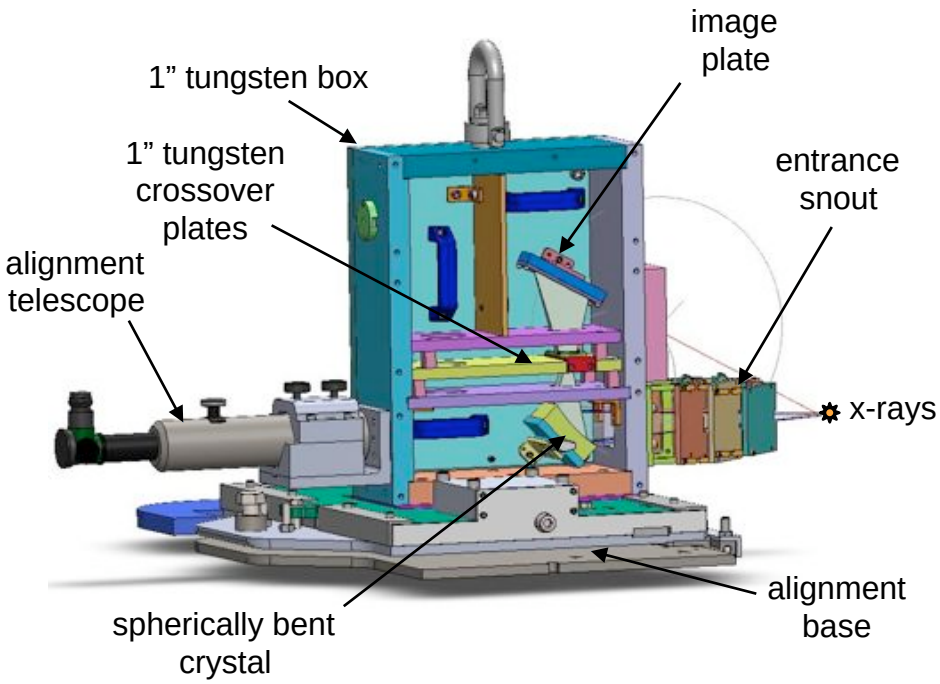

Figure 6.4. X-ray scattering spherical spectrometer (XRS^3).

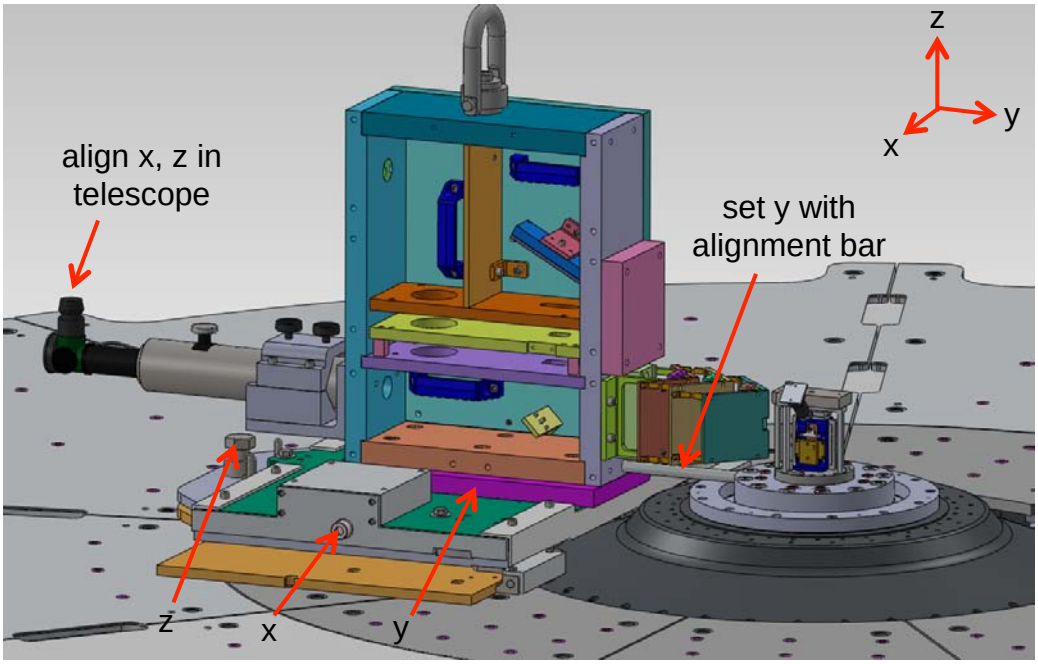

Figure 6.5. Positioning of XRS[3] to the Z-DMP load with the alignment base.

6.4. X-ray Background of Z-DMP Experiments

In CY2012, there were two x-ray background tests performed with the CRITR-RR (compact rugged in-chamber transmission-type with radial-spatial resolution) spectrometer [46] as a ride-along to Z-DMP experiments. The CRITR-RR spectrometer is similar to the XRS[3] spectrometer; it also uses a crystal and an IP detector inside of a tungsten box to shield against both high-energy x-rays and debris. In addition, CRITR-RR has already been fielded in previous Z experiments while XRS[3] had not yet been commissioned for Z experiments. Thus, in the meantime CRITR-RR was chosen for the x-ray background tests. The first test was on the Z-DMP shot Z2368 (coaxial load hardware A0221B) that had Z fired at a Marx charge voltage of 75 kV. The CRITR-RR spectrometer looked through an opening in the blast shield to view the load, and the IP was scanned 14 hours after shot (Fig. 6.6). Overall, the x-ray background for the Z-DMP shot Z2368 was very encouraging with the average background level (~ 0.01 PSL) much, much lower than a typical radiation producing Z-pinch shot. The structure near the right-hand side of the IP is the "straight-through" radiation that was not diffracted by the crystal, passed straight through the imaging slit, and captured on the IP. On a nominal radiation producing shot this region is usually saturated (> 25 PSL), while on the Z-DMP shot the straight-through PSL level < 1 PSL and it was very locally concentrated.

The second test was on Z-DMP shot Z2371 (coaxial load hardware A0223A), but Z was fired at a Marx charge voltage of 82 kV. There was no blast shield opening for CRITR-RR to view the

load, and the IP was scanned 2 hours after the shot (Fig. 6.7). The x-ray average background level of Z2371 was slightly higher (~ 0.03 PSL) than Z2368, but still well below the expected signal of the x-ray scattering (~ 0.5 PSL). Although, there a 12-hour difference between the scan times of the IP for the two shots, it's known that after the initial 100 minutes the fade rate of the IP is very slow (< 10%) [44]. The main reason for the higher x-ray background is most likely the higher voltage induced large electron flow current in the magnetically insulating lines (MITL) of Z that generated more x-rays.

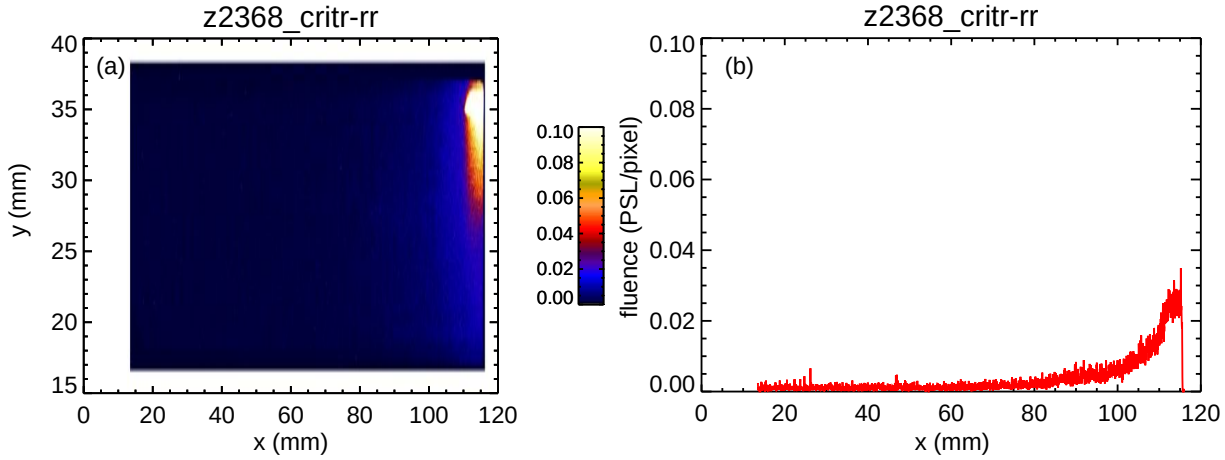

Figure 6.6. X-ray background of Z-DMP shot Z2368 measured using CRITR-RR spectrometer: (a) IP image, and (b) horizontal lineout at the center of the IP.

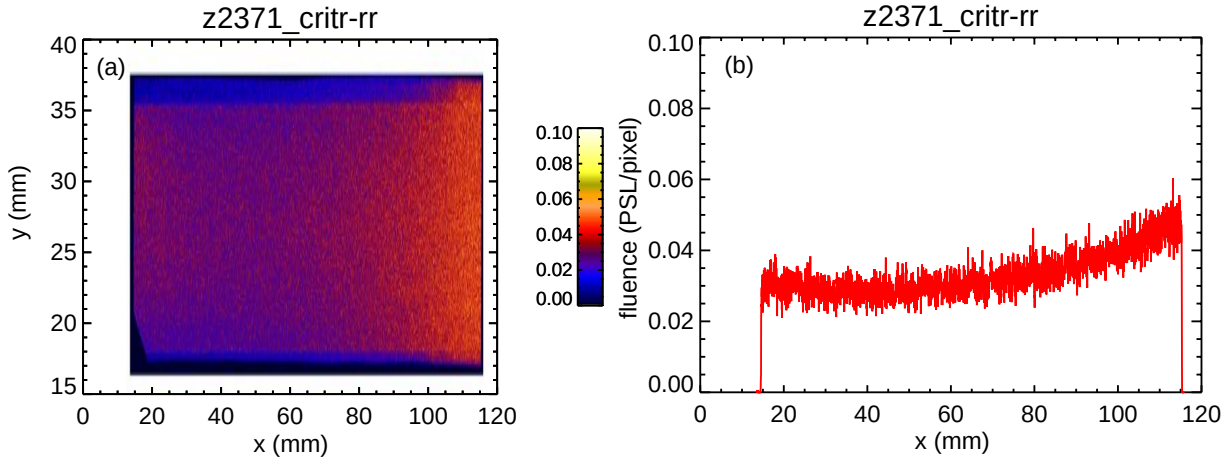

Figure 6.7. X-ray background of Z-DMP shot Z2371 measured using CRITR-RR spectrometer: (a) IP image, and (b) horizontal lineout at the center of the IP.

6.5. ZBL Alignment and Timing

Since 2003, ZBL has been successfully fielded on Z for monochromatic x-ray backlighting of wire-array Z-pinch plasmas [47-50]. However, in the upcoming Z-XRTS experiments, it will be the first time ZBL will be aligned and timed to a Z-DMP load. The ZBL beam originates in the ZBL facility that is housed in a separate building next to the Z-accelerator. The laser pulse is transported 75 m along a relay telescope assembly between the two buildings before reaching the axis of the Z center section chamber. There the square beam (32 cm by 32 cm) reaches a final optics assembly (FOA) consisting of a turning mirror and a 3.2 m focal length lens. The procedure for aligning ZBL to this new Z-DMP configuration is similar to the earlier Z-pinch configuration, but will involve one key difference. In the Z-pinch configuration, the ZBL beam is focused to a spot size of 150 μm onto a metal foil 100 – 200 mm from the Z-axis to generate x-rays to image an imploding plasma pinch. However, for the Z-DMP configuration the ZBL beam will be focused on the foil that will only be about 25 mm from the Z-axis. Because ZBL will be aligned so near on-axis of Z, mitigation of load debris from damaging the FOA require consideration, which will be discussed in the Section 6.6.

Figure 6.8 shows an overhead view of the ZBL entering the Z-DMP load region through a hole in the blast shield lid. Inside the blast shield, the ZBL beam will pass through three baffle plates (Fig. 6.1(b)) and an aperture block above the Z-DMP load (Fig. 6.9(a)), before being focused onto the Mn foil. Precise alignment of ZBL will be provided using a camera with field of view (FOV) of 3 mm placed near the Mn foil that has fiducial notches (Fig. 6.9(b)).

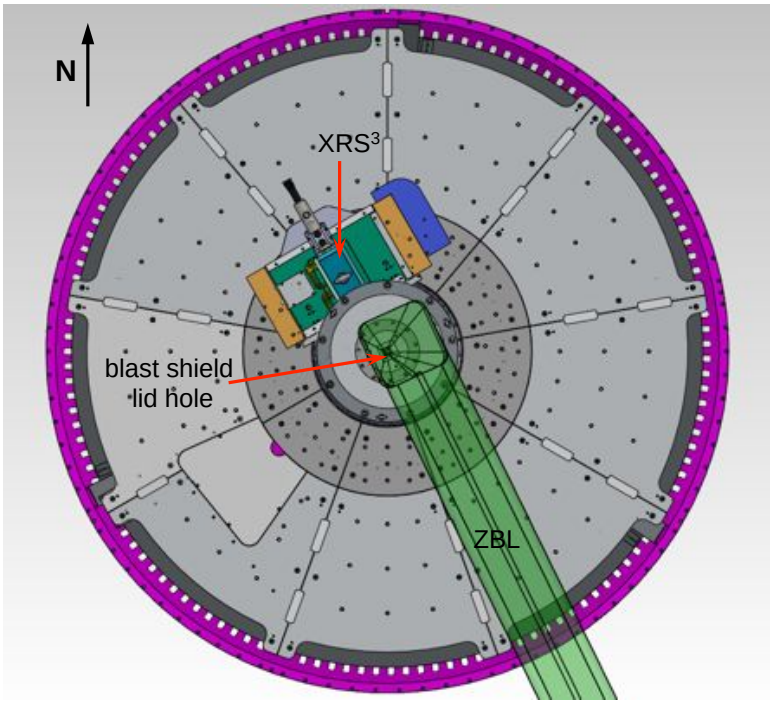

Figure 6.8. Overhead view of ZBL entering to Z-DMP load region.

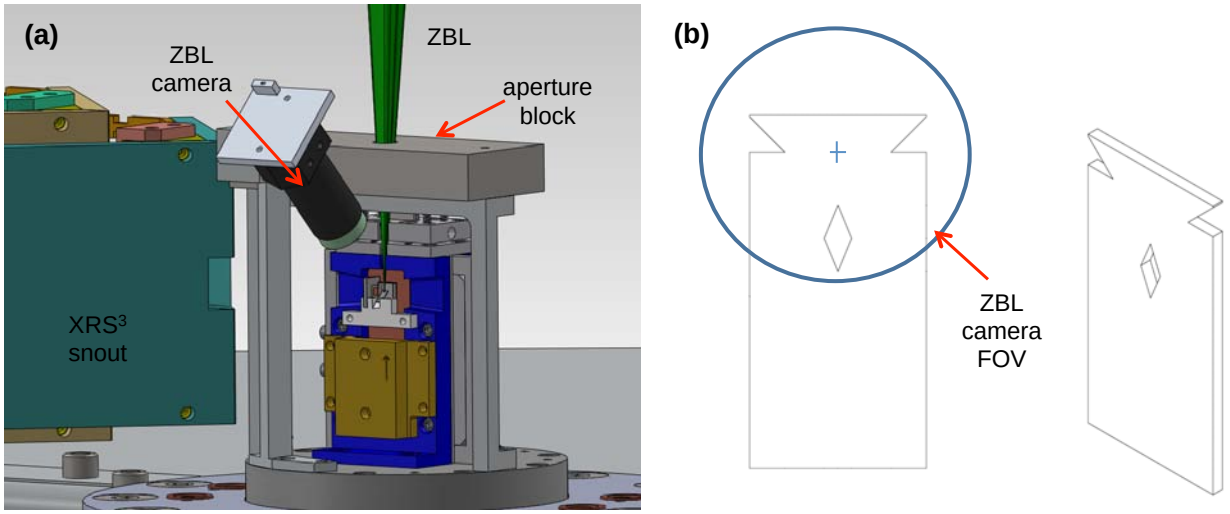

Figure 6.9. ZBL alignment to Z-DMP load: (a) isometric view, and (b) ZBL camera field of view of the Mn foil.

For Z-pinch experiments, the firing of ZBL (2 ns pulse length) has been precisely synchronized relative to the Z "machine time" firing sequence. For Z-DMP experiments, normally only VISAR is fielded, which uses a separate VISAR laser (5 μs pulse length). Because the VISAR laser pulse is so long, it does not require as precise of synchronization as ZBL to the firing of Z. When Z is fired, a trigger pulse is sent to the VISAR laser that continuously illuminates the Z-DMP sample as the current pulse reaches the Z-DMP load to magnetically launch the flyer which impacts and sends a shock wave through the sample.

However, XRTS of the Z-DMP load will require ZBL to be timed more precisely so that the x-rays are generated while the sample is being shock compressed. For the initial Z-XRTS experiment with a 16 km/s Al flyer impacting a 1.5 mm thick CH_2 foam sample (see Fig. 3.9(b)), the x-rays should penetrate into sample when the shock wave has propagated only 1.0 mm through it, so that 0.5 mm of foam remains ambient ahead of the shock front (± 0.1 mm). This will require the firing synchronization of ZBL and the Z-DMP load to be ± 5 ns.

While there are on-going efforts to VISAR signals to the Z machine time base, for XRTS experiments an alternative approach will be used to pinpoint the correct ZBL firing relative to the Z-DMP load. The SVS diagnostic have been field for both Z-pinch and Z-DMP experiments and have already been synchronized to the Z machine time base. In one of the commissioning shots on Z, the Z-DMP load will be fired without ZBL being fired, and the SVS diagnostic will be fielded on two "timing" samples below the top XRTS sample. Timing sample 1 will be a quartz window, and timing sample 2 will be a CH_2 sample that is identical to the XRTS sample but backed by a quartz window. When the Al flyer impacts the timing samples, SVS will record the "impact emission" from the quartz timing sample 1. Later in time when the shock wave has propagated completely through the CH_2 timing sample 2, SVS will record the "shock-breakout

emission". The firing of ZBL for the actual Z-XRTS experiment will be synchronized to occur 50 ns after the impact time, and 25 ns before the shock-breakout time (see Fig. 3.9(b)).

6.6. ZBL Debris Mitigation

The experimental environment of Z is inherently destructive. The large current pulse and extreme magnetic fields at the Z load literally causes it to explode, and results in debris flying outwards at very high velocities (~ tens of km/s). While post-shot examination of previous Z experiments have shown that the debris consists of both hot fluids (plasma and liquid) and solid fragments, the actual debris field remains to be well characterized. The purpose of the blast shield surrounding the Z load is to contain the debris from damaging the rest of the Z center section. An entrance hole in the top lid of the blast shield enables ZBL to be focused on to a x-ray source target near the Z load, which also allows debris to escape out (Fig. 6.10).

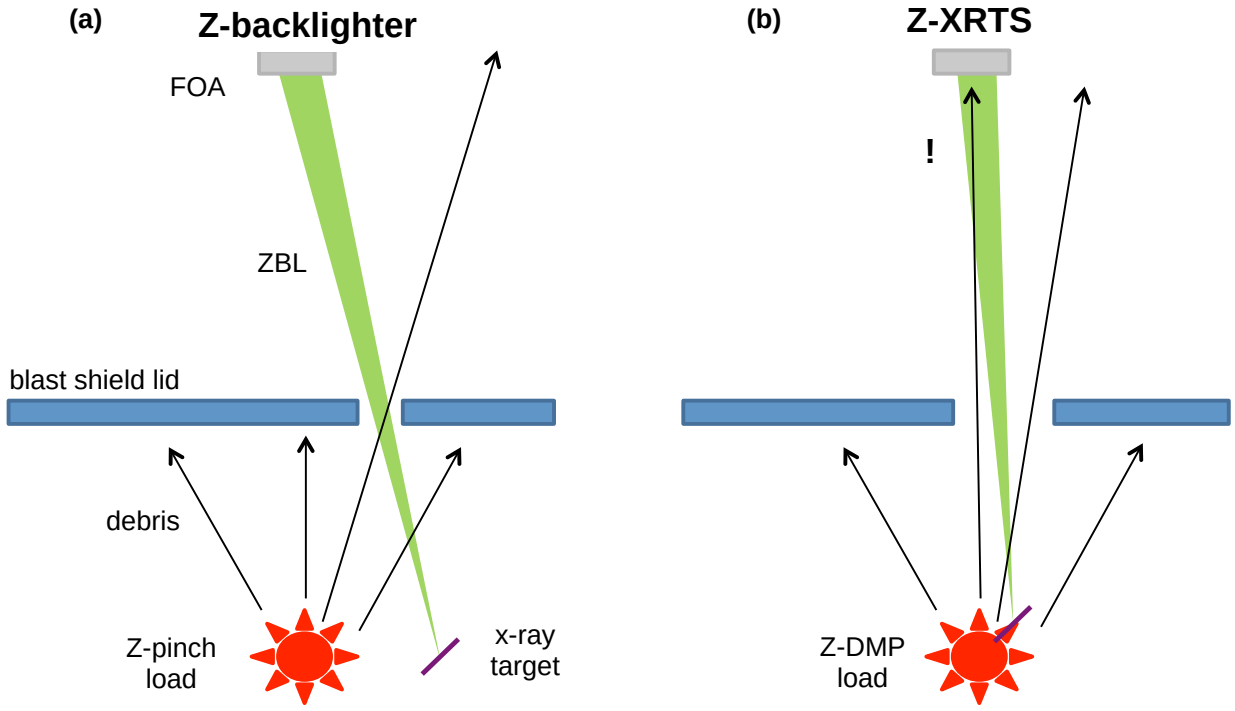

Figure 6.10. Schematic of possible direct LOS debris reaching the FOA of ZBL: (a) Z-backlighter configuration with Z-pinch load, and (b) Z-XRTS configuration with Z-DMP load.

As description in Section 6.5, x-ray backlighting of the Z-pinch load uses a x-ray source target that is displaced about 200 mm from the load. Thus, the entrance hole in the blast shield lid is slightly offset from the central axis of Z, and debris from the Z-pinch load has no direct line-of-sight (LOS) to the FOA of ZBL (Fig. 6.10(a)). However, there is still the possibility of debris ricocheting up towards it. In the Z-XRTS experiment, the x-ray source is only about 25 mm

from the Z-DMP load, thus the blast shield entrance hole is almost on-axis of Z and there is a direct LOS to the FOA (Fig. 6.10(b)).

Figure 6.11 shows the cross section view of the FOA of ZBL that sits on the Z center section white lid. Inside the FOA is a 30 mm thick fused silica (SiO_2) window that is the final interface between the Z center section under vacuum pressure and the ZBL focusing lens under atmospheric pressure. If debris were to impact the vacuum window, then it might crack and fail, damage the ZBL lens, lead to a vacuum breach and catastrophic venting of the center section into the Z facility. Although such a scenario occurring is remote, but it would severely affect the operation of the Z facility. Thus, a sacrificial 10 mm thick fused silica debris shield is placed below the vacuum window to stop any debris from reaching it. In previous Z-backlighting experiments on Z-pinch loads, while ricocheting debris have impacted and damaged the debris shield, the vacuum window was untouched. However, it is uncertain if the current debris shield would survive direct LOS debris and if the vacuum window would be remain undisturbed.

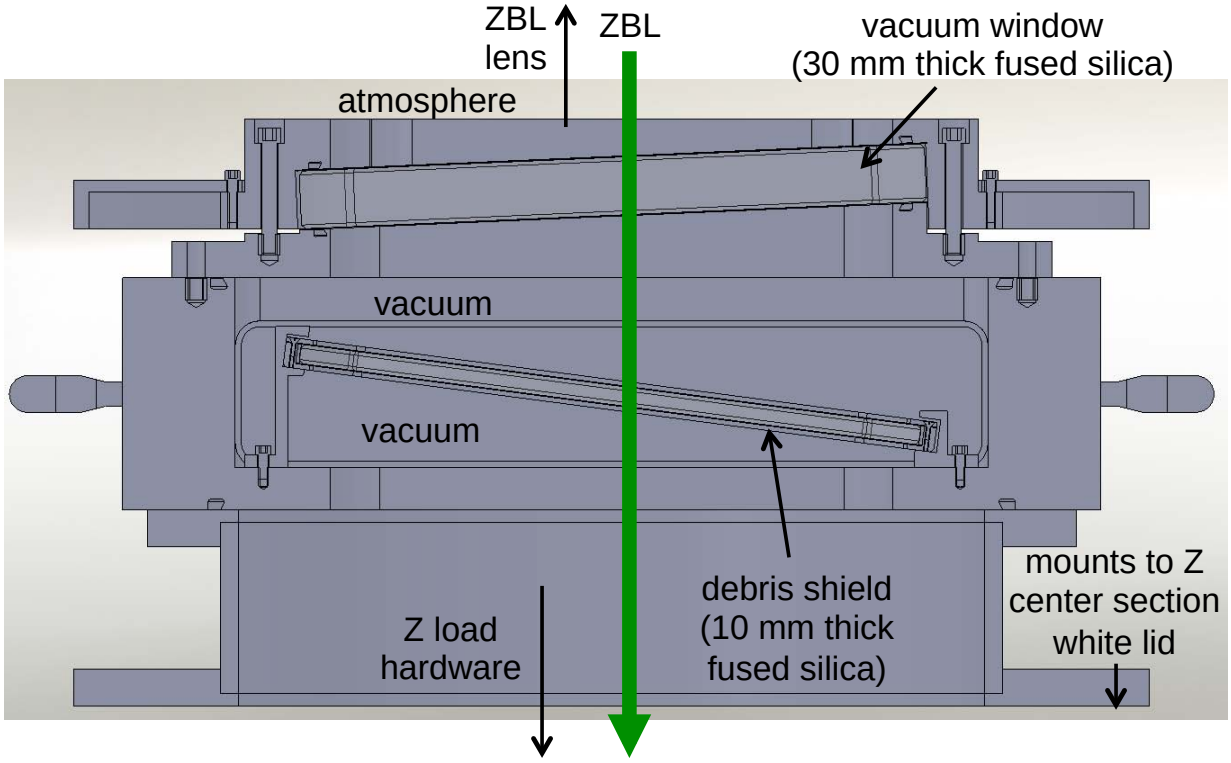

Figure 6.11. Cross section view of the FOA of ZBL.

6.6.1. Z-DMP debris field characterization experiments

An investigation into mitigating the risk of debris damage to the FOA of ZBL, several ride-along tests on Z-DMP experiments were done in CY 2012 to better characterize the debris field. In the first test on shot Z2293, a regular DMP blast shield with a pristine aluminum lid was used to record debris from a Z-DMP coaxial load. Post-shot examination of the blast shield lid show that while there were a few noticeable craters created by the impact of solid fragments, the majority of the debris was spattered molten liquid (Fig. 6.12).

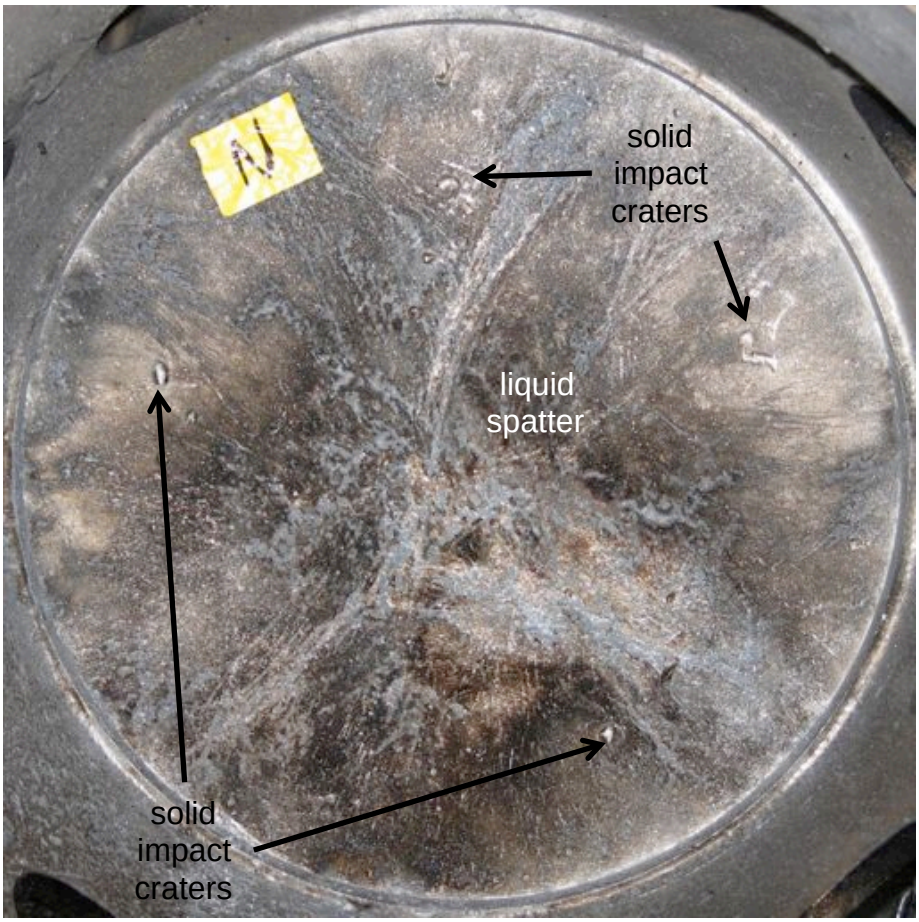

Figure 6.12. Inside view of the load debris recorded on the regular DMP blast shield lid after shot Z2293.

In the next ride along test on shot Z2324, the modified blast shield for XRTS with the entrance hole in its lid was fielded. Inside the XRTS blast shield, baffle plates near the Z-DMP load was designed to limit the amount of debris vertically directed towards the FOA. An aluminum witness plate was installed in place of the 10 mm fused silica debris shield inside the FOA. The witness plate served to record all of the debris that passed through the blast shield baffles and to prevent any debris from reaching the vacuum window.

Inside the XRTS blast shield after shot Z2324 (Fig. 6.13), the debris pattern was similar to those observed on regular DMP blast shield after shot Z2293 (Fig. 6.12). Some cratering from solid fragments occurred on surfaces closest to the load hardware, though most of the debris appeared to have been liquid at time of impact. The baffles remained attached during the shot, though the mounting bolts were slightly deformed. The bottom-most baffle survived the shot intact, though it was somewhat cratered.

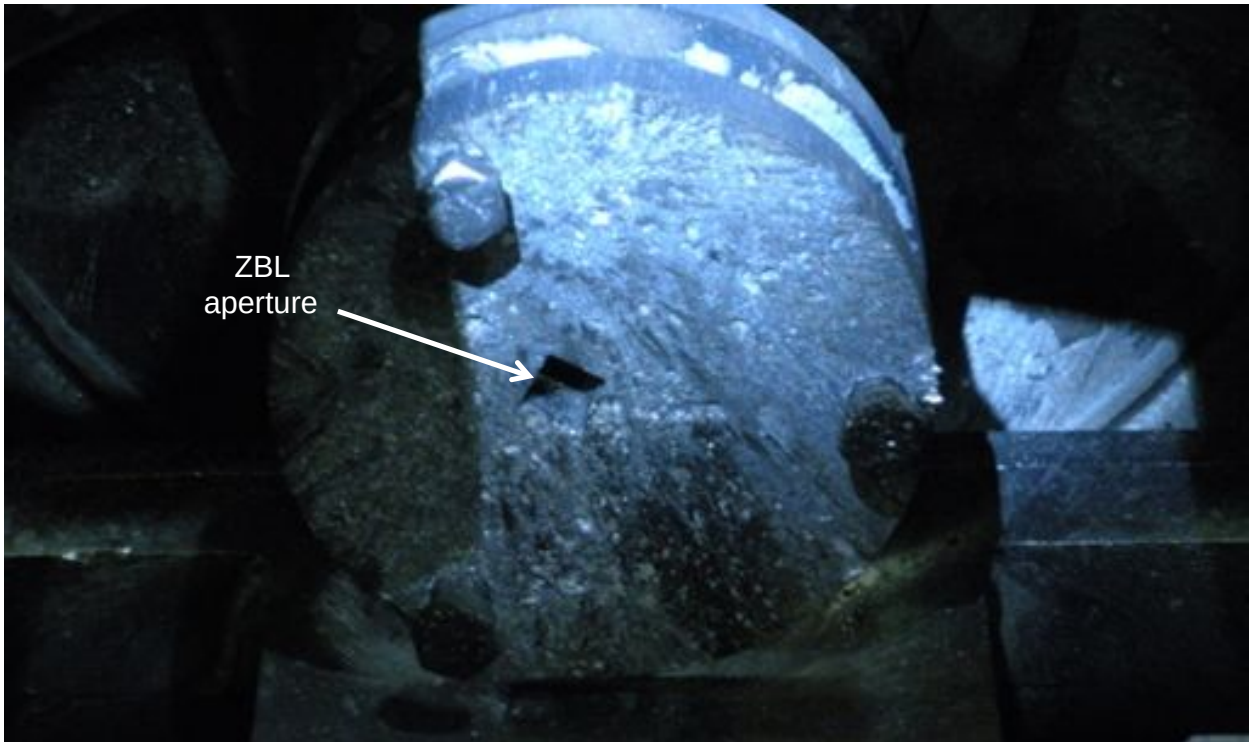

Figure 6.13. Inside view of the XRTS blast shield and baffle plates after shot Z2324.

As observed in shot Z2293, the vertically directed debris of Z2324 that reached the witness plate appeared to have been liquid metal (Fig. 6.14(a)). Many of the droplet "splats" had long "fingers" (Fig. 6.14(b)), which indicates the impinging debris was liquid and moving at relatively high velocities. Most of the metallic splatter was easily wiped off with an alcohol wetted cotton cloth. A brief post cleaning examination revealed that the debris did not perceptibly crater the plate, which was further evidence that the debris is mostly liquid at impact.

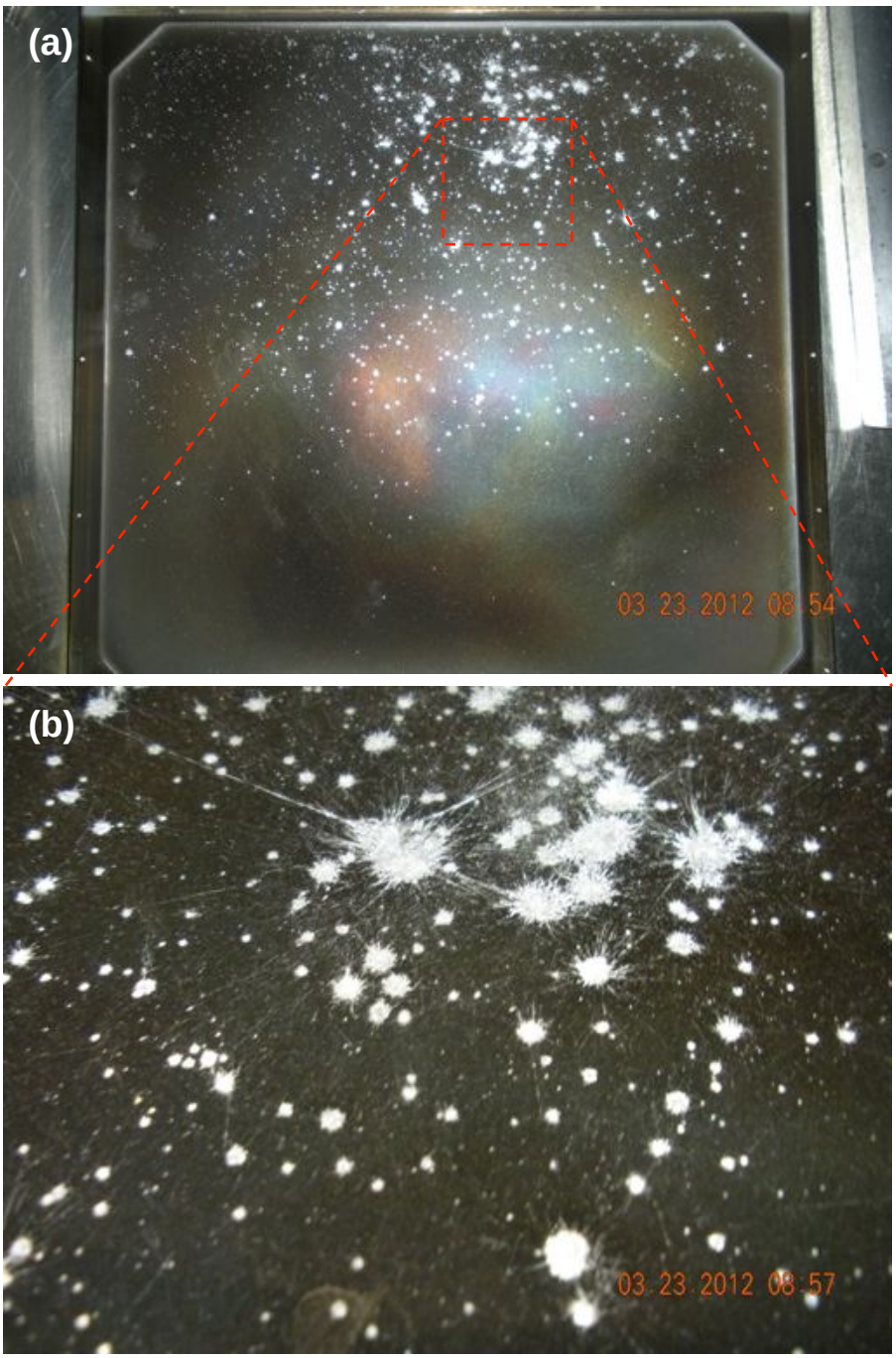

Figure 6.14. Debris recorded after shot Z2324 on the (a) Al witness plate placed at the debris shield location; (b) detail view of the liquid droplet splatter.

6.6.2. Hypervelocity impact models

The issues concerning penetration of the FOA debris shield and vacuum window are similar to the hypervelocity impact problems that spacecrafts are routinely faced with, so there is some guidance in the literature [51-56]. Space and orbital vehicles require the use of windows, such as fused silica glass, tempered glass, and polycarbonate, for means of guidance and navigation, observation and monitoring of external surfaces and activities. Hypervelocity impact tests on these materials under a variety of impact conditions have been investigated in order to define penetration equations that allow assessment of impact damage to windows.

Figure 6.15 (reproduced from Ref. [55]) shows the typical high-velocity impact damage features of glass targets, in which the low tensile strength and brittle nature of glass leads to comparatively extensive internal fracturing and surface spallation with comparatively shallow crater depths. The impact craters generally have a central area of high damage that can appear white in color, surrounded by circular fracture patterns. Internal fracturing can also be observed within glass targets that are below the crater limits, the depth of which is of interest for fracture analysis.

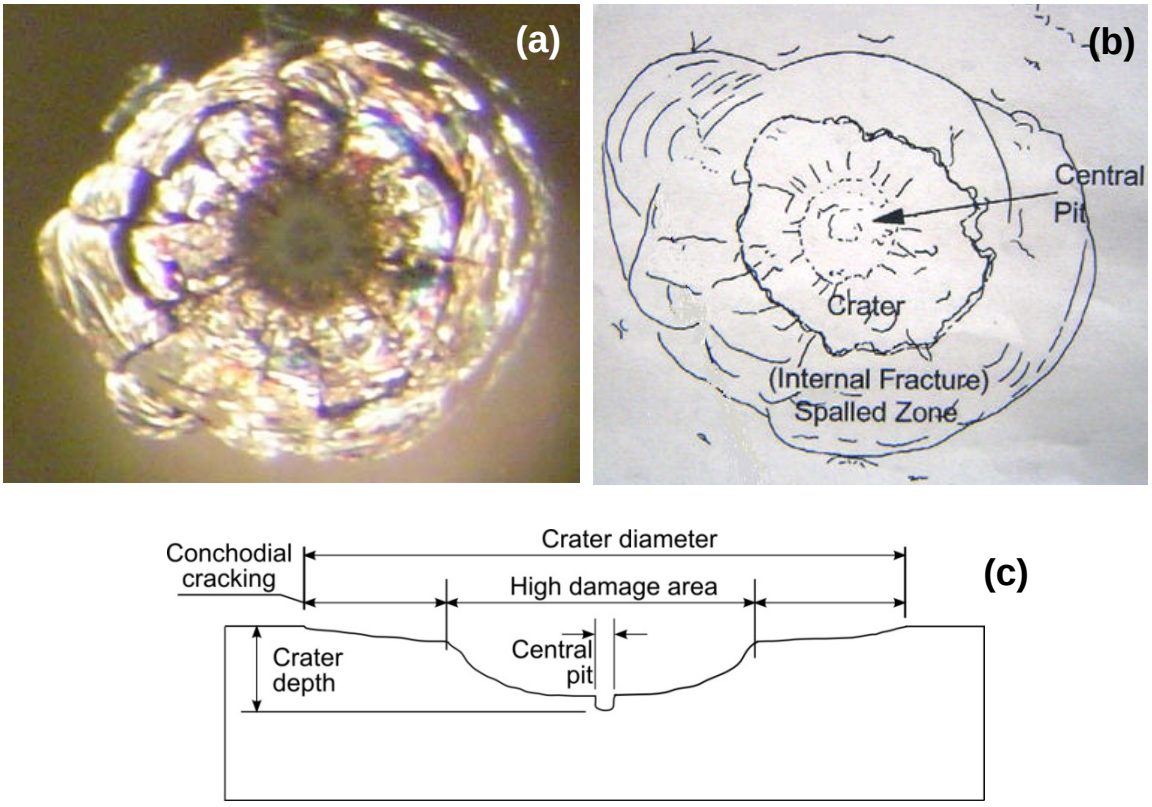

Figure 6.15. Damage characteristics and measurements in glass targets: (a) photograph (front view), (b) schematic (front view), and (c) damage measurement schematic (side view) taken from Ref. [55].

For as semi-infinite fused silica glass, damage equations for the impact crater depth P (cm) were developed by Cour-Palais [51]:

$$P = 0.53\rho_P^{0.5} d_P^{1.06} \left(V\cos\theta\right)^{2/3}, \tag{6.1}$$

and for front surface crater (spall) diameter D (cm) by Edelstein [52]:

$$D = 30.9\rho_P^{0.44} d_P^{1.33} \left(V\cos\theta\right)^{0.44}, \tag{6.2}$$

where ρ_d is the projectile density (g/cm^3), d_P is the projectile diameter (cm), V is the projectile velocity (km/s), and θ is the impact angle. The damage equations were slightly modified to better model newer impact damage data by Burt and Christiansen [53]:

$$P = 0.266\rho_P^{0.595} d_P^{1.05} V^{0.995} \left(\cos\theta\right)^{0.496}, \tag{6.3}$$

and

$$D = 9.656\rho_P^{0.373} d_P^{1.183} V^{0.915} \left(\cos\theta\right)^{0.545}. \tag{6.4}$$

The required shielding thickness t_s can be determined for a test particle depending on the failure mode [56],

(1) to prevent perforation: $t_s \geq 2.0P$, (6.5)

(2) to prevent spallation: $t_s \geq 3.0P$, (6.6)

and (3) to prevent cracking: $t_s \geq 7.0P$. (6.7)

To ensure that the 30 mm thick vacuum window is left untouched by any debris, the design goal is prevent perforation of the 10 mm thick fused silica glass debris shield. Using Eqn. 6.1, a ballistic limit curve for copper particles (8.96 g/cm^3) impacting at normal angle (0°) onto a 10 mm thick fused silica glass target is shown in Fig. 6.16. The red box indicates the region where the model has experimental data. Using the perforation failure mode (Eqn. 6.5), particles with velocities and diameters to the left of the ballistic limit curve will not penetrate the shield (success), while those particles on the right of the curve will penetrate the shield (failure). For example, a 1 cm diameter copper particle moving at 200 m/s will perforate a 10 mm thick glass shield, but it would take 1 mm diameter copper particle with a velocity greater than 7 km/s to perforate it.

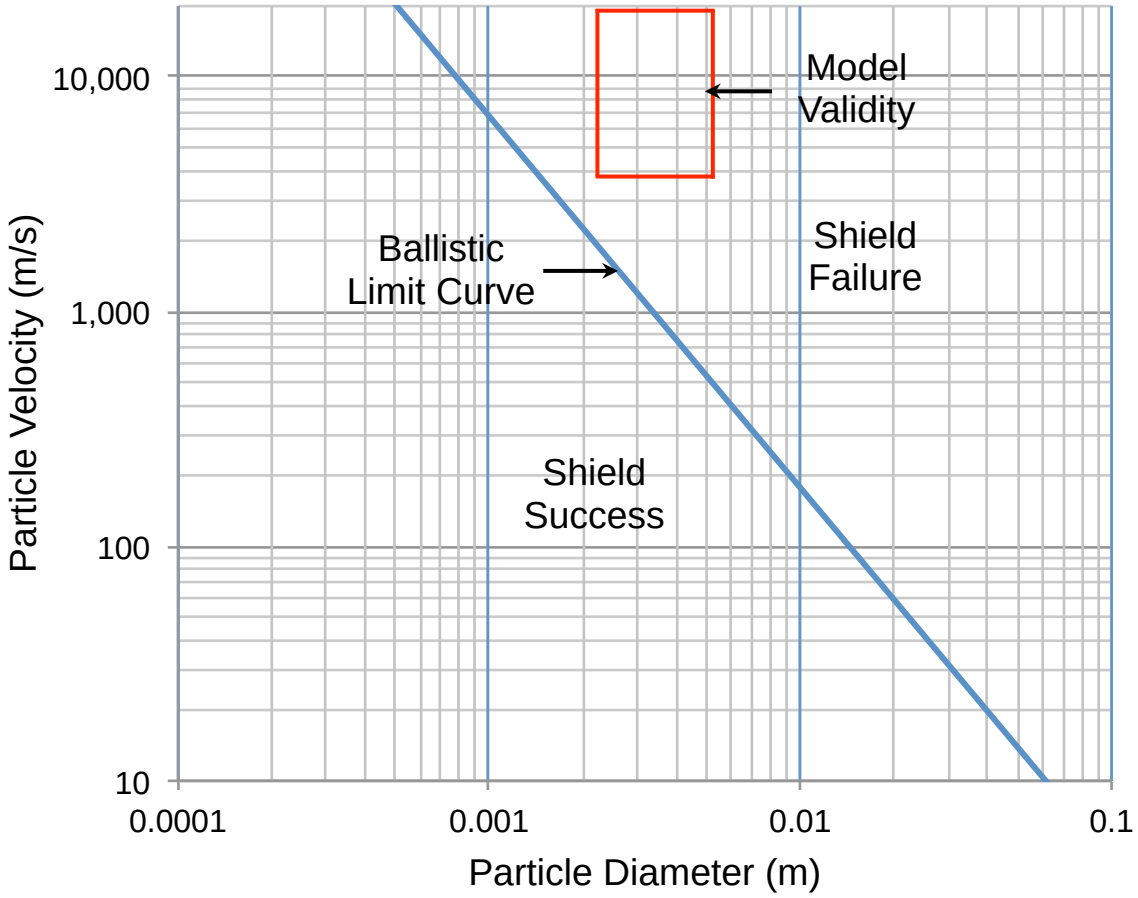

Figure 6.16. Ballistic limit curve for copper particles impacting a 10 mm thick fused silica glass target.

The shield perforation resistance can be improved by modifying the following parameters: (1) increase shield thickness; (2) reduce debris material density; (3) reduce debris velocity; and (4) reduce debris size as shown in Fig. 6.17. The design of the XRTS experiment has considered these parameters in mind to mitigate the risk of damaging the FOA of ZBL.

The first design modification would be to replace the current 10 mm thick glass debris shield with thicker one. This would move the ballistic limit curve up and to the right of Fig. 6.17, thus increasing range of particle velocities and diameters that the shield would be successful. However as the thickness of the glass debris shield is increased, the focusing quality of the ZBL would degrade. Thus, maintaining a well-focused ZBL laser spot the x-ray source target near the load would limit the glass debris shield's thickness to about 30 mm. Nonetheless, to replace the current 10 mm thick glass debris shield with a 30 mm thick one would require a major redesign of the FOA, so that modification would not be available until sometime in the future.

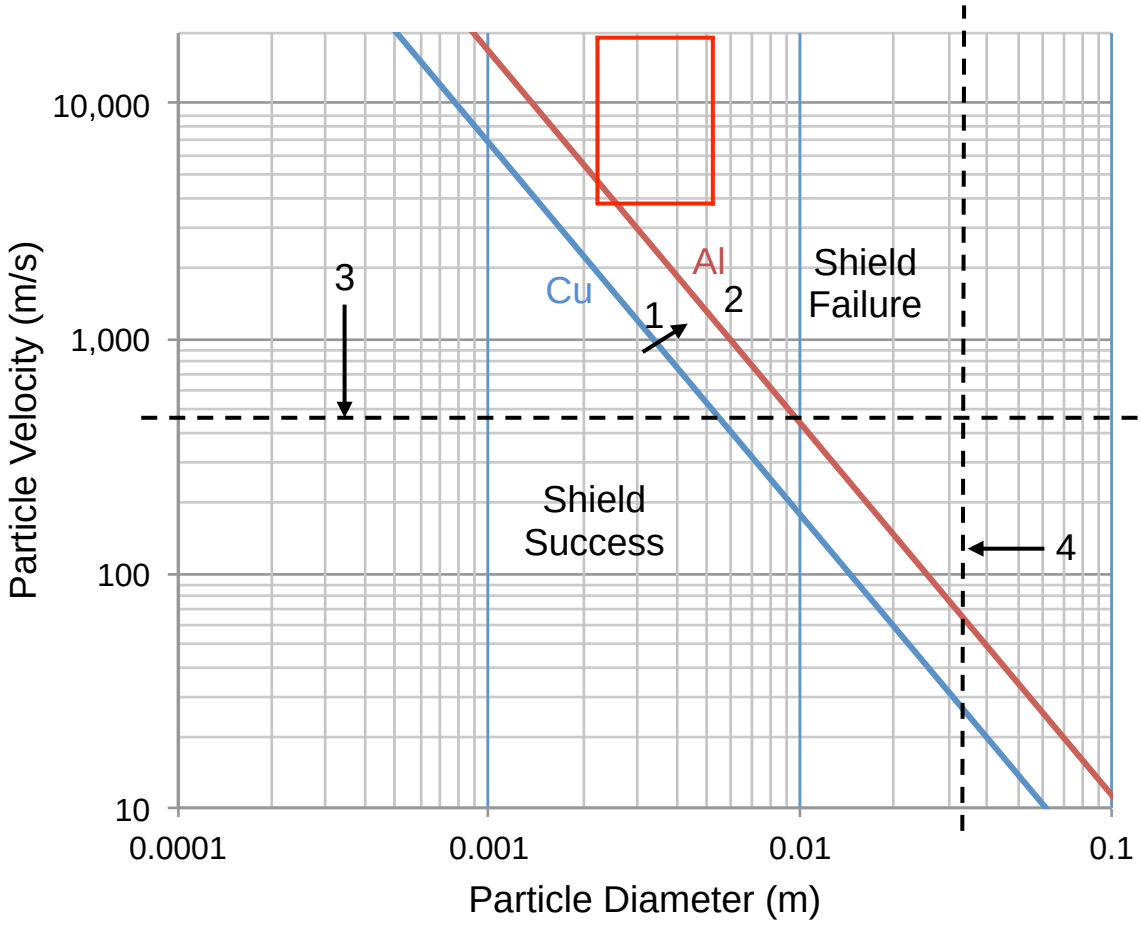

Figure 6.17. Ballistic limit curves for copper and aluminum particles impacting a 10 mm thick fused silica glass target. Perforation performance may be improved by (1) increasing shield thickness, (2) reducing particle material density; (3) reducing particle velocity; and (4) reducing particle size.

The second experimental modification would be to ensure that the Z-DMP load is constructed of low-density materials, which would also move the ballistic limit curve up and to the right Fig. 6.17. For the Z-XRTS experiment, the Z-DMP load will be fabricated almost entirely of aluminum, except for some of the smaller component such as the target frame and x-ray shielding which will be made of tantalum. These small tantalum parts will not be in the direct LOS of the FOA and should be blocked by the baffle plates of the XRTS blast shield.

The third experimental consideration for debris mitigation would be to reduce the maximum velocity of the debris particles. Typically on Z-DMP experiments, the Marx banks are charged at (60 – 82) kV, which deliver (15 – 26) MA current pulses to the load. Reducing the Marx charge voltage will decrease the current pulse at the load, which will limit the velocity of the load debris. For the initial Z-XRTS experiments, a low Marx charge voltage of 54 kV will be used to deliver only 14 MA to the Z-DMP load. As confidence in the debris mitigation scheme to protect the FOA of ZBL increases, the Marx charge voltage will be carefully raised in later Z-XRTS experiments.

The fourth way to improve the perforation performance of the glass debris shield would be to limit the size of the particles reaching the FOA. As described in Section 6.6.1, baffle plates inside the XRTS blast shield does aperture a large amount of the vertically directed debris (see Fig. 6.12 as compared to Fig. 6.14). A designed aperture block with an inner diameter of 6 mm will be located just above the Z-DMP load (Fig. 6.9(a)) to future restrict the debris size able to reach the FOA (Fig. 6.18).

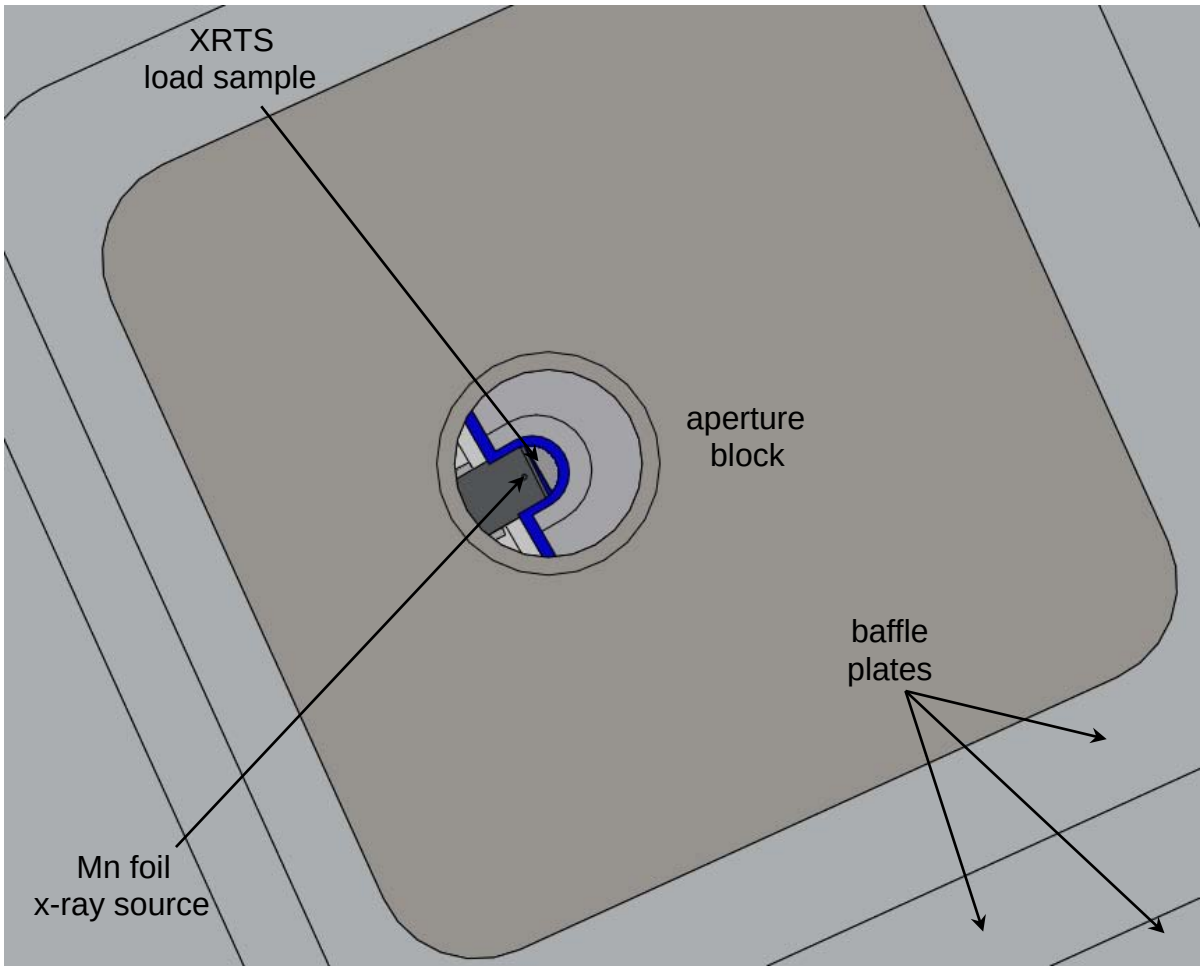

Figure 6.18. Top view of ZBL line-of sight to the Z-XRTS load through the aperture block and baffle plates.

There are several favorable conditions that indicate that mitigation of debris to the FOA would be successful. First, the damage models assume solid projectiles that likely cause more damage to the glass debris shield than liquid droplets. A total of 7 ride along tests on Z-DMP coaxial loads have been performed in CY 2012, which showed that the debris is likely molten. Out of those 7 shots, only one noticeable crater was observed, which had an estimated diameter of ~ 1 mm, and an impact velocity on order of ~ (1 – 3) km/s. In the ride along debris tests on Z-DMP

experiments, only the baffle plates in the XRTS blast shield were used, which had a much larger opening than the current aperture block design (0.56 vs. 0.04 in^2), so about 14× more debris was allowed to escape towards the FOA than would be anticipated with the aperture block in place for the planned Z-XRTS experiment.

Conversely, there are several unfavorable conditions about the debris mitigation scheme. First, the design used the damage models outside of the correlation applicability window where there was hypervelocity impact data. Second, the aperture block design has been untested, but it will be fielded in upcoming ride along Z-DMP experiments. Finally, the low number of debris experiments (N = 7) doesn't capture low probability events such as a high velocity solid projectile coming straight through the aperture block and baffle plates, perforating the glass debris shield and damaging the vacuum window. In any case, a plan of action is being developed in the event that the mitigation strategy fails and there is damage to the FOA and a vacuum breach.

7. A HIGH IMPACT X-RAY SCATTERING EXPERIMENT AT Z

7.1. Introduction

Lithium deuteride or lithium hydride presents an interesting low Z material of interest to our science campaigns, and is the lowest Z crystalline material under ambient conditions, forming the NaCl (rock salt) structure of two interlaced FCC lattices, as shown in Fig. 7.1. Lithium deuteride has a 5 eV band gap, which means that good crystal samples are transparent to visible light, an important consideration for pyrometry measurements.

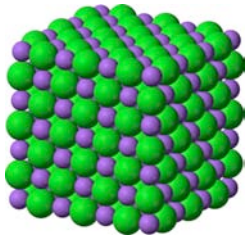

Figure 7.1. The rocksalt crystal structure of lithium hydride.

7.2. Equation of State and Impedance Matching Calculations

Existing equations of state for lithium deuteride differ above the relatively low pressures reached in early gas gun experiments, as seen in Fig. 7.2. Data from explosively driven shock experiments (Ragan) is shown in red.

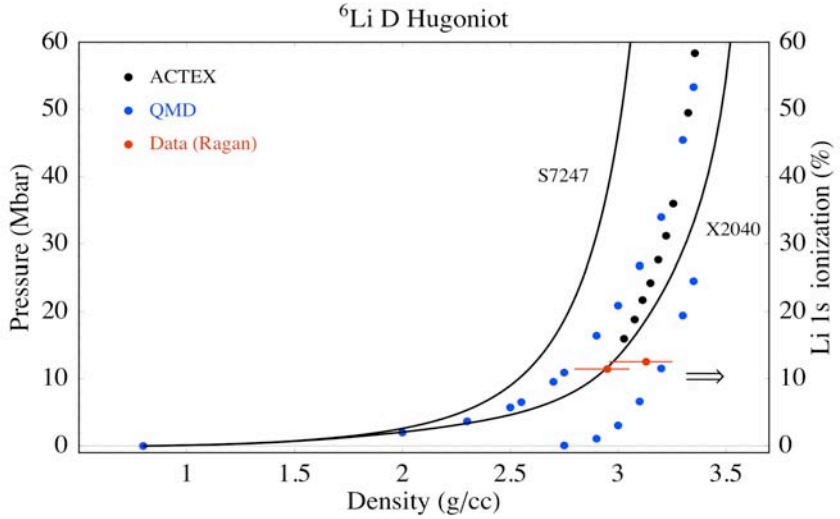

Figure 7.2. The Hugoniot for ^{6}Li D is plotted for two equations of state. Hugoniot results from first-principles quantum molecular dynamics simulations are show with the blue points. Also shown with blue points (right axis) is the ionization degree of the 1s core electrons.

The blue points shown in Fig. 7.2 (left axis) are the results of our quantum molecular dynamics simulations with the VASP code. These points clearly differ from both equations of state beyond a few Mbar in pressure (the range of the early gas gun experiments), but appear to merge with ACTEX calculations above 30 Mbar.

Figure 7.3 illustrates an impedance matching analysis of what might be accessible on the Z machine. Aluminum flyer velocities in excess of 40 km/s have been demonstrated already on Z. Here we show what could be achieved with lithium deuteride using a somewhat conservative flyer velocity of around 35 km/s.

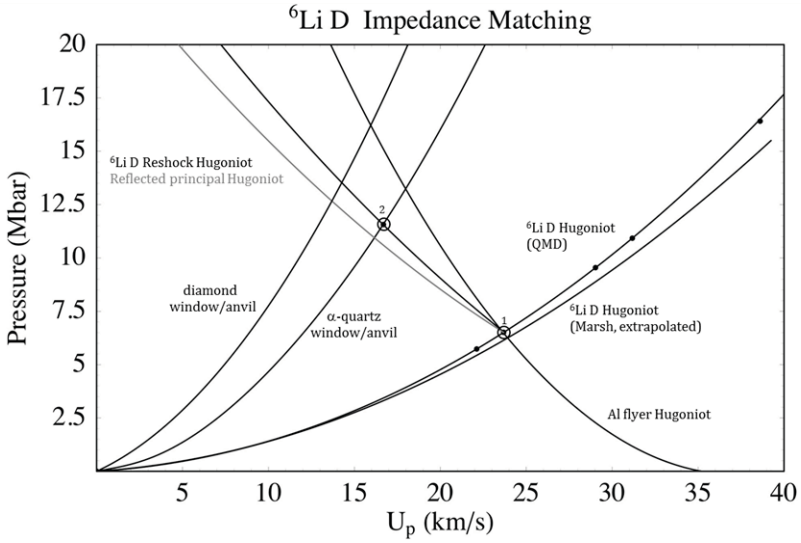

Figure 7.3. Impedance matching analysis for lithium deuteride under experimental conditions achievable on Z.

The point labeled "1" indicates the ~ 6.5 Mbar state reached on the first shock, as predicted for a flyer velocity of 35 km/s and using our calculated QMD Hugoniot. The point labeled "2" indicates the conditions reached on the reflection of that first shock on a quartz window or anvil. Replacing quartz with diamond would further increase the reshock pressure state. It is clear from Fig. 7.3 that Z can reach conditions that would significantly enhance our understanding of LiD and would provide needed data for the next generation equation of state for this material.

Pressure and density are the primary experimental state variables deduced from traditional shock wave experiments analyzed through point VISAR signals. However, temperature measurements place a much-needed constraint on the equation of state. Figure 7.4 shows the principle shock and reshock states along with the calculated temperature in those states.

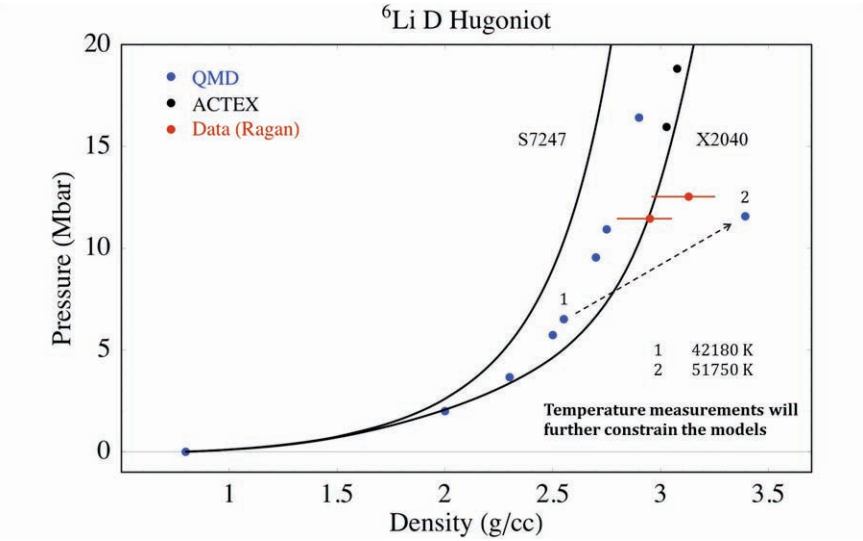

Figure 7.4. A pressure-density plot showing proposed first and second shot states for a Z experiment, along with the predicted temperature.

The predicted temperatures are 42180 K and 51750 K for the first and second shock respectively. These temperatures are in a range where both pyrometry and x-ray Thomson scattering are viable diagnostics. However for good visible light pyrometry data, a transparent or near transparent material is required. To this end we would propose to also perform experiments with single crystal lithium hydride. The use of single crystal lithium hydride will also substantially reduced the error bars on the VISAR analysis as the reflecting shock front of the compressed sample will be directly observable. In the case of powder or cake samples, the shock speed will have to be deduced from transit time analysis. A further benefit will be the measurement of the reflectivity of the shocked material, which can be directly compared to the predictions from the QMD calculations.

7.3. X-Ray Thomson Scattering Considerations

The feasibility of an x-ray Thomson scattering experiment for a given material rests largely on the penetration and scattering depth of the available source photons. Table 7.1 shows calculated photoelectric, coherent (elastic), and incoherent (inelastic) cross sections for the lithium and the deuterium. Note that the coherent scattering will be dominated by the lithium component and the total penetration depth will be dominated by the photoelectric cross section of the lithium component. Assuming a first shock density of 2.5 g/cc in ^{6}LiD, 1.88 g/cc of that material is from the ^{6}Li component, resulting in a 1/e photoelectric absorption depth of 0.74 cm (ignoring the deuterium contribution), and a total 1/e depth of 0.53 cm. These lengths are quite favorable to experiments on Z with typical dynamic materials sample sizes.

Table 7.1. Total cross sections for lithium-6 and deuterium in cm^2/g, assuming 6.2 keV photons. Multiply the lithium figures by 3 for relative scattering amplitudes in bulk ^{6}LiD (6:2 relative mass ratio in bulk).

	Photoelectric	Coherent	Incoherent
Deuterium	0.00685	0.0263	0.157
^{6}Lithium	0.718	0.154	0.124

The basic equations for Thomson scattering analysis are shown below:

$$\frac{d^2\sigma}{d\Omega d\omega} = \left(\frac{d\sigma}{d\Omega}\right)_{Th} \frac{k_1}{k_0} S(k,\omega), \tag{7.1}$$

$$S(k,\omega) = \underbrace{\left|f_I(k)+q(k)\right|^2 S_{ii}(k,\omega)}_{\text{ion term, elastic}} + \overbrace{Z_f S^0_{ee}(k,\omega)}^{\text{free electron term, inelastic}} + \underbrace{Z_b \int \tilde{S}_{ce}(k,\omega-\omega')S_s(k,\omega')d\omega'}_{\text{bound-free term, inelastic}}. \tag{7.2}$$

Under the proposed experimental conditions, the electrons will be degenerate ($T_e < T_{Fermi}$) in both the first and second shock states. Therefore the width of the inelastic Compton feature in the non-collective scattering limit will not reveal the electron temperature, but can be used to infer the free electron density, which when combined with the density of the shocked material from VISAR analysis can give a mean ionization state. Similarly, for collective scattering observation of the plasmon, the thermal energy is significantly less than the plasmon energy, so the upshifted plasmon will not likely be visible, preventing the use of the Bose factor in deducing the electronic temperature. Temperature measurements will therefore rely on the ion term, the elastic scattering feature. The Li-Li structure factor is shown in Fig. 7.5 for the predicted conditions of the first shock (black points). Also shown is the structure factor predicted for 1 eV higher temperature (red points) and 1 eV lower temperature (blue points). Note that in the vicinity of 70° scattering for 6.2 keV photons, there is no predicted dependence. Therefore if two spectrometers are available, this can be used as a reference scattering amplitude. Also shown with thin black lines in Fig. 7.5 are the locations of the first three Bragg reflection peaks of the unshocked FCC lithium lattice. Given that the x-rays in the experiment will likely traverse a region of unshocked ^{6}LiD before encountering the shocked material, it would probably be advantageous to avoid looking along these directions.

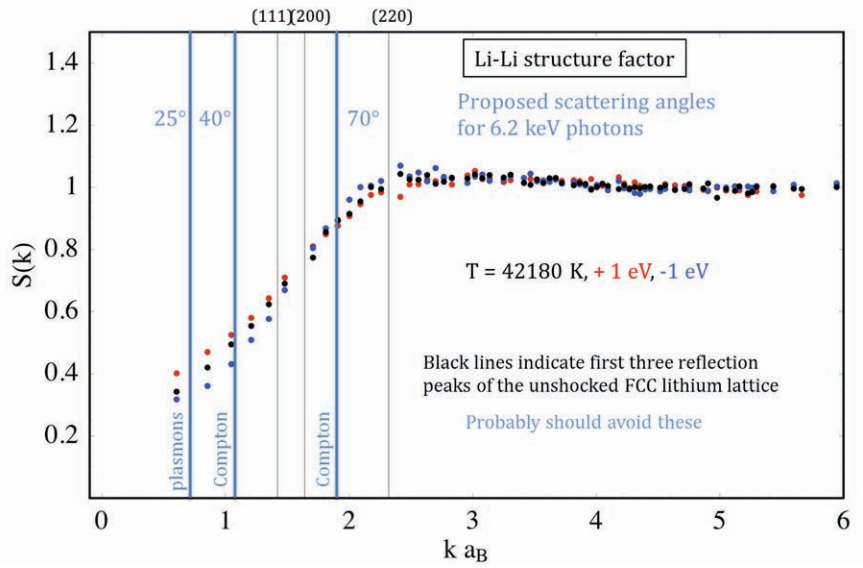

Figure 7.5. The QMD calculated Li-Li structure factor for the lithium component of ^{6}LiD for the predicted conditions of the proposed first shock state. The thin black lines indicate the reflection peaks of the unshocked FCC lithium lattice.

7.4. Lithium Deuteride Material Considerations

Lithium deuteride reacts violently with water and will likely need to be encapsulated. It is also pyrophoric when exposed to humid air, especially when in finely divided or powder form. Samples for use on Z will need to be prepared in an inert environment. Care will be needed in accounting for the encapsulating material in the impedance matching and x-ray Thomson scattering analysis. Handling protocols for lithium deuteride or lithium hydride are well established and will need to be incorporated into the shot planning.

7.5. Load Hardware

Figure 7.6 illustrates a load hardware design by Root and Dalton that could be used for LiD samples, particularly if they are in powdered or cake form. This design permits a degree of compaction on the powdered sample, improving the accuracy with which the reference Hugoniot state will be known.

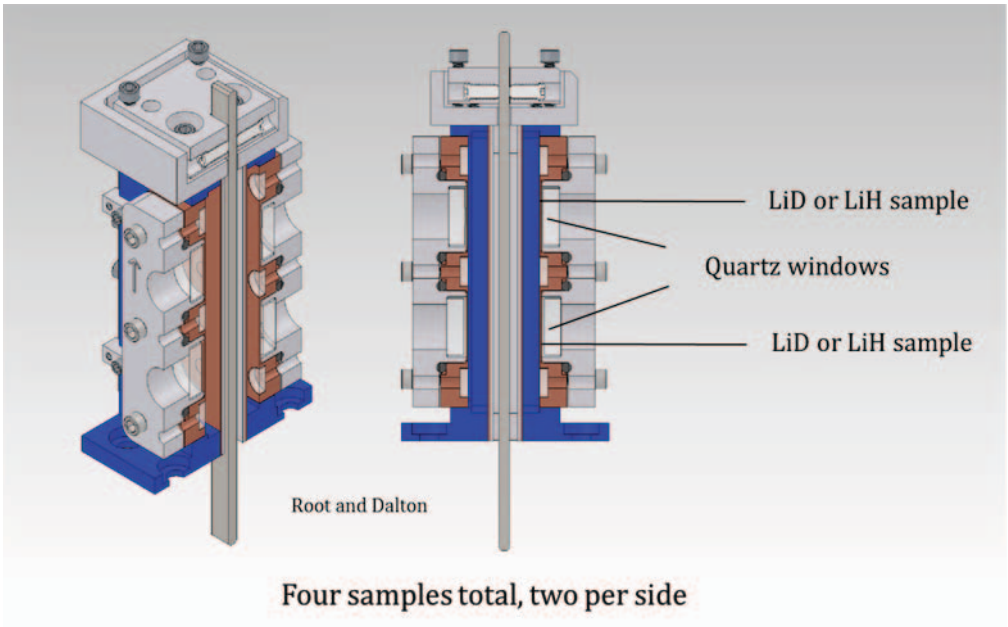

Figure 7.6. A schematic of the proposed load hardware for a LiD experiment on Z.

7.6. Conclusions

Z experiments can access pressures in LiH or LiD that would significantly extend our understanding of the equation of state for this interesting material and stimulate the next generation of EOS refinement. The large sample sizes on Z (in comparison to laser driven XRTS experiments), the uniformity of the shocked material, the expectation of very good pyrometry temperature measurements for the conditions of interest, and the direct observation of the shock velocity for the single crystal material would together combine to provide the high energy density physics community with outstanding reference data and a stringent test for the theoretical analysis of XRTS spectra. In turn, the observation of the elastic scattering amplitude at appropriately chosen angles will provide ion temperature data that can be directly compared to the electronic temperature indicated by the pyrometry measurements. These measurements in turn will provide needed constraints on the equation of state.

8. SUMMARY

This LDRD project was designed to advance warm dense matter (WDM) physics by combining the powerful x-ray Thomson scattering (XRTS) diagnostic with the extreme environments created at the Z facility. The foundation for the new XRTS capability on Z has been established, which will help maintain Sandia's leadership in dynamic materials and radiation science. The key achievements of the LDRD projected are summarized in this section.

A theoretical framework suitable for designing and interpreting Z-XRTS experiments has been developed in-house at Sandia. The new theoretical code, based on quantum mechanical approaches that treat scattering from bound and free electrons on an equal footing, is aimed at going beyond previous scattering calculations that use a chemical picture of the atoms. There are measureable differences between the predictions of the previous models and the new Sandia model, which will be benchmarked on Z-XRTS experiments.

The magnetohydrodynamics code ALEGRA was used to simulate the expected warm dense matter (WDM) states created by Z in the scattering experiments. For the initial Z-XRTS experiment, a Z-DMP (Dynamic Material Properties) coaxial load will be used with the Z Marx banks set to a charge voltage of 54 kV. The shaped current pulse will magnetically launch an Al flyer (16 km/s) to impact a CH_2 foam (0.1 g/cm^3) sample. The shocked CH_2 (0.37 Mbar, 2.6 eV) WDM state will have a large spatial extent (600 μm) and long steady-state duration (20 ns) that will be highly accessible for probing by the XRTS diagnostic.

A new high sensitivity x-ray scattering spherical spectrometer (XRS^3) based on the FSSR (focusing spectrometer with spatial resolution) geometry was designed and fabricated. The XRS^3 spectrometer will enable benchmark quality data because it will measure x-ray scattered signals with both high spatial (~ 75 μm) and spectral ($E/\Delta E$ ~ 1500) resolution. Since it will be fielded inside the Z center section, the XRS^3 spectrometer was designed to withstand damage from the load debris and shield against the x-ray background generated by Z. The quality of several types of spherically bent crystals, including HOPG, HAPG, quartz, germanium and mica, were investigated using the Manson x-ray source. Overall, a spherically bent germanium 422 crystal was shown to have best spatial and spectral resolution and collective efficiency, thus it will be fielded in the Z-XRTS experiments.

Experiments were performed on the Z Beamlet laser (ZBL) facility to investigate a suitable x-ray source for the Z-XRTS experiments. ZBL was optimized (2 kJ, 0.5 ns pre-pulse, 2 ns main pulse) to generate the bright Mn-He-α (6.181 keV) emission from a laser irradiated thin (5μm) Mn foil. In addition, x-ray scattering from ambient CH_2 foam in the ZBL calibration chamber was measured using the XRS^3 spectrometer. The simultaneous measurement of source x-rays and scattered x-rays was successfully demonstrated.

Preparations for the upcoming Z-XRTS experiments in the 4th quarter of CY2012 (November & December) have been completed. Because it will be the first time that ZBL will be fielded with a Z-DMP load, precise synchronization of Z and ZBL for this new configuration will be established with the streaked visible spectrometry (SVS) system. In addition, since ZBL will be

focused on-axis of Z, debris mitigation plans are in place to protect the final optical assembly (FOA) of ZBL. The mitigation strategy involves limiting the size of on-axis debris with a load aperture block and baffle plates, and minimizing the velocity of debris by firing Z at a low charge voltage. Fortunately, experimental data from several Z-DMP experiments have shown that the vertically launched debris are mostly molten droplets, which are less likely to damage the FOA than high velocity solid fragments. Finally, the XRS^3 spectrometer is designed with ample amounts of tungsten plates to shield against the x-ray background of Z. Encouragingly, the average background level (~ 0.01- 0.03 PSL) of Z-DMP experiments was also shown to be much, much lower than typical radiation producing Z-pinch experiments, so a reasonably good signal-to-noise for the Z-XRTS experiment is anticipated.

The initial set of Z-XRTS experiments will demonstrate the capability of x-ray scattering as a much needed temperature diagnostic for opaque WDM samples. The main experimental goal will be to obtain high quality temperature data that will benchmark the equation-of-state (EOS) of materials. Specifically, the temperature measurement from elastic x-ray scattering of shocked single crystal lithium deuteride in CY 2013 experiments will allow EOS completion of a material of high interest. Additionally, the application of XRTS to cryogenic Z-DMP loads will be provide invaluable EOS information for materials of interest to inertial confinement fusion (ICF) and planetary science (e.g. D_2). Beyond being a robust temperature measurement, the XRTS diagnostic will be also developed to provide phase and ionization information of WDM states. For example, future Z-DMP experiments (CY 2014) of shock compressed beryllium coupled with XRTS would allow examination of interesting physical phenomena such as continuum lowering, pressure ionization, and solid-liquid coexistence.

This LDRD project will benefit the Nuclear Weapons SMU and Chief Technology Officer Program with vastly improved ability to characterize materials in WDM and extreme plasma conditions, improve the understanding of underlying physics, and advance predictive capability. It is expected that valuable scientific results will be available within 2 years, and XRTS will be in routine use and maturation within 5 years. A legacy of every improving capability based on tools developed in this LDRD project (e.g. x-ray diffraction) reaching to 15 years is anticipated. The XRTS project will be fully absorbed in the Science Campaign/ICF Program starting in FY2013 and Z resources has been assigned.

9. REFERENCES

1. S. Ichimaru, *Strongly coupled plasmas: high-density classical plasmas and degenerate electron liquids*, Rev. Mod. Phys. **54**, 1017 (1982).
2. M. K. Matzen, M. A. Sweeney, R. G. Adams, J. R. Asay, J. E. Bailey, G. R. Bennett, D. E. Bliss, D. D. Bloomquist, T. A. Brunner, R. B. Campbell, G. A. Chandler, C. A. Coverdale, M. E. Cuneo, J.-P. Davis, C. Deeney, M. P. Desjarlais, G. L. Donovan, C. J. Garasi, T. A. Haill, C. A. Hall, D. L. Hanson, M. J. Hurst, B. Jones, M. D. Knudson, R. J. Leeper, R. W. Lemke, M. G. Mazarakis, D. H. McDaniel, T. A. Mehlhorn, T. J. Nash, C. L. Olson, J. L. Porter, P. K. Rambo, S. E. Rosenthal, G. A. Rochau, L. E. Ruggles, C. L. Ruiz, T. W. L. Sanford, J. F. Seamen, D. B. Sinars, S. A. Slutz, I. C. Smith, K. W. Struve, W. A. Stygar, R. A. Vesey, E. A. Weinbrecht, D. F. Wenger, and E. P. Yu, *Pulsed-power-driven high energy density physics and inertial confinement fusion research*, Phys. Plasmas **12**, 055503 (2005).
3. J. D. Lindl, P. Amendt, R. L, Berger, S. G. Glendinning, S. H. Glenzer, S. W. Haan, R. L. Kauffman, O. L. Landen, and L. J. Sutter, *The physics basis for ignition using indirect-drive targets on the National Ignition Facility*, Phys. Plasmas **11**, 339 (2004).
4. D. Saumon, G. Chabrier, and H. M. Van Horn, Astrophys. *An Equation of State for Low-Mass Stars and Giant Planets*, J. Suppl. Ser. **99**, 713 (1995).
5. T. Guillot, *Interiors of Giant Planets Inside and Outside the Solar System*, Science **286**, 72 (1999).
6. E. I. Moses and C. R. Wuest, *The National Ignition Facility: Laser Performance and First Experiments*, Fusion Sci. Technol. **47**, 314 (2005).
7. T. R. Boehly, D. L. Brown, R. S. Craxton, R. L. Keck, J. P. Knauer, J. H. Kelly, T. J. Kessler, S. A. Kumpan, S. J. Loucks, S. A. Letzring, F. J. Marshall, R. L. McCrory, S. F. B. Morse, W. Seka, J. M. Soures, and C. P. Verdon, *Initial performance results of the OMEGA laser system*, Opt. Commun. **133**, 495 (1997).
8. R. W. Lee, S. J. Moon, H.-K. Chung, W. Rozmus, H. A. Baldis, G. Gregori, R. C. Cauble, O. L. Landen, J. S. Wark, A. Ng, S. J. Rose, C. L. Lewis, D. Riley, J.-C. Gauthier, and P. Audebert, *Finite temperature dense matter studies on next-generation light sources*, J. Opt. Soc. Am. B **20**, 770 (2003).
9. G. W. Collins, L. B. Da Silva, P. Celliers, D. M. Gold, M. E. Foord, R. J. Wallace, A. Ng, S. V. Weber, K. S. Budil, and R. Cauble, *Measurements of the Equation of State of Deuterium at the Fluid Insulator-Metal Transition*, Science **281**, 1178 (1998).
10. M. D. Knudson, R. W. Lemke, D. B. Hayes, C. A. Hall, C. Deeney, and J. R. Asay, *Near-absolute Hugoniot measurements in aluminum to 500 GPa using a magnetically accelerated flyer plate technique*, J. Appl. Phys. **94**, 4420 (2003).
11. O. L. Landen, S. H. Glenzer, M. J. Edwards, R. W. Lee, G. W. Collins, R. C. Cauble, W. W. Hsing, and B. A. Hammel, *Dense matter characterization by X-ray Thomson scattering*, J. Quant. Spectrosc. Radiat. Transf. **71**, 465 (2001).
12. S. H. Glenzer, G. Gregori, R. W. Lee, F. J. Rogers, S. W. Pollaine, and O. L. Landen, *Demonstration of Spectrally Resolved X-Ray Scattering in Dense Plasmas*, Phys. Rev. Lett. **90**, 175002 (2003).
13. S. H. Glenzer, O. L. Landen, P. Neumayer, R. W. Lee, K. Widmann, S. W. Pollaine, and R. J. Wallace, *Observations of Plasmons in Warm Dense Matter*, Phys. Rev. Lett. **98**, 065002 (2007).

14. H. J. Lee, P. Neumayer, J. Castor, T. Döppner, R. W. Falcone, C. Fortmann, B. A. Hammel, A. L. Kritcher, O. L. Landen, R. W. Lee, D. D. Meyerhofer, D. H. Munro, R. Redmer, S. P. Regan, S. Weber, and S. H. Glenzer, *X-Ray Thomson-Scattering Measurements of Density and Temperature in Shock-Compressed Beryllium*, Phys. Rev. Lett. **102**, 115001 (2009).
15. A. L. Kritcher, P. Neumayer, J. Castor, T. Döppner, R. W. Falcone, O. L. Landen, H. J. Lee, R. W. Lee, B. Holst, R. Redmer, E. C. Morse. A. Ng, S. W. Pollaine, D. Price, and S. H. Glenzer, *Ultrafast X-ray Thomson Scattering of Shock-Compressed Matter*, Science **322,** 69 (2008).
16. H. Sawada, S. P. Regan, D. D. Meyerhofer, I. V. Igumenshchev, V. N. Goncharov, T. R. Boehly, R. Epstein, T. C. Sangster, V. A. Smalyuk, B. Yaakobi, G. Gregori, S. H. Glenzer, and O. L. Landen, *Diagnosing direct-drive, shock-heated, and compressed plastic planar foils with noncollective spectrally resolved x-ray scattering*, Phys. Plasmas **14**, 122703 (2007).
17. G. Gregori, S.H. Glenzer, W. Rozmus, R.W. Lee, and O.L. Landen, *Theoretical model of x-ray scattering as a dense matter probe*, PRE **67**, 026412 (2003).
18. G. Gregori, S. H. Glenzer, and O. L Landen, *Generalized x-ray scattering cross section from nonequilibrium plasmas*, Phys. Rev. E **74**, 026402 (2006).
19. S. H. Glenzer and R. Redmer, *X-ray Thomson scattering in high energy density plasmas*, Rev. Mod. Phys. **81**, 1625 (2009).
20. D. A. Liberman, *Self-consistent field model for condensed matter*, Phys. Rev. B **20**, 4981 (1979).
21. B. Wilson, V. Sonnad, P. Sterne, and W. Isaacs, *PURGATORIO—a new implementation of the INFERNO algorithm,* J. Quant. Spectrosc. Radiat. Transf. **99**, 658 (2006).
22. W. R. Johnson, C. Guet, and G. F. Bertsch, *Optical properties of plasmas based on an average-atom model*, J. Quant. Spectrosc. Radiat. Transf. **99**, 327 (2006); W. R. Johnson, *Low-frequency conductivity in the average-atom approximation*, High Energy Density Physics **5**, 61 (2009).
23. S. B. Hansen, A. Ya. Faenov, T. A. Pikuz, K. B. Fournier, R. Shepherd, H. Chen, K. Widmann, S. C. Wilks, Y. Ping, H. K. Chung, A. Niles, J. R. Hunter, G. Dyer, and T. Ditmire, *Temperature determination using Kα spectra from M-shell Ti ions*, Phys. Rev. E **72**, 036408 (2005).
24. J. Chihara, *Difference in X-ray scattering between metallic and non-metallic liquids due to conduction electrons*, J. Phys. F: Met. Phys. **17**, 295 (1987).
25. S. Sahoo, G. F. Gribakin, G. Shabbir Naz, J. Kohanoff, and D. Riley, *Compton scatter profiles for warm dense matter*, PRE **77**, 046402 (2008).
26. P. Eisenberger and P. M. Platzman, *Compton Scattering of X Rays from Bound Electrons,* PRA **2**, 415 (1970).
27. P. M. Platzman and N. Tzoar, *X-Ray Scattering from an Electron Gas*, PR **139**, A410 (1965).
28. Walter Johnson, 2010 private communication.
29. S. B. Hansen, M. P. Desjarlais, J. E. Bailey, and E. C. Harding, WDM 2010.
30. D. A. Baiko, A. D. Kaminker, A. Y. Potekhin, and D. G. Yakovlev, *Ion Structure Factors and Electron Transport in Dense Coulomb Plasmas*, Phys. Rev. Lett. **81**, 5556 (1998)
31. W. Johnson, WDM workshop at IPAM HEDP, (2012).

32. A. C. Robinson, T. A. Brunner, S. Carrol, et al., *"ALEGRA: An arbitrary Lagrangian-Eulerian multimaterial, multiphysics code." 46th AIAA Aerospace Sciences Meeting and Exhibit*, Reno, NV, 2008; AAIAA 2008-1235: p. 1-39.
33. R. W. Lemke, M. D. Knudson, and J-P Davis, *Magnetically driven hyper-velocity launch capability at the Sandia Z accelerator*, Int. J. Impact Engineering **38**, 480 (2011), and references therein.
34. R. W. Lemke, M. D. Knudson, A. C. Robinson, T. A. Haill, K. W. Struve, J. R. Asay, and T. A. Mehlhorn, *Self-consistent, two-dimensional, magnetohydrodynamic simulations of magnetically driven flyer plates*, Phys. Plasmas **10** (5), 1867 (2003), and references therein.
35. R. W. Lemke, M. D. Knudson, D. E. Bliss, K. Cochrane, J.-P. Davis, A. A. Giunta, H. C. Harjes, and S. A. Slutz, *Magnetically accelerated, ultrahigh velocity flyer plates for shock wave experiments*, J. Appl. Phys. **98**, 073530 (2005).
36. E. J. Gamboa, D. S. Montgomery, I. M. Hall, and R. P. Drake, *Imaging X-ray crystal spectrometer for laser-produced plasmas*, J. Instrum. **6**, P04004 (2011).
37. T. A. Pikuz, A. Ya. Faenov, S. A. Pikuz, V. M. Romanova, and T. A. Shelkovenko, *Bragg X-Ray Optics for Imaging Spectroscopy of Plasma Microsources*, J. X-ray Sci. Technology **5**, 323 (1995).
38. B. F. K. Young, A. L. Osterheld, D. F. Price, R. Shepherd, R. E. Stewart, A. Ya. Faenov, A. I. Magunov, T. A. Pikuz, I. Yu. Skobelev, F. Flora, S. Bollanti, P. Di Lazzaro, T. Letardi, A. Grilli, L. Palladino, A. Reale, A. Scafati, and L. Reale, *High-resolution x-ray spectrometer based on spherically bent crystals for investigations of femtosecond laser plasmas*, Rev. Sci. Instrum. **69**, 4049 (1998).
39. D. B. Sinars, G. A. Chandler, J. E. Bailey, R. C. Mancini, G. A. Rochau, D. F. Wenger, R. G. Adams, M. L. Adams, H. A. Scott, A. Ya. Faenov, T. A. Pikuz, and S. A. Pikuz, *Measurements of K-shell Ar spectra from z-pinch dynamic hohlraum experiments made using a focusing spectrometer with spatial resolution*, J. Quant. Spectrosc. Radiat. Transf. **99**, 595 (2006).
40. S. G. Gales and C. D. Bentley, *Image plates as x-ray detectors in plasma physics experiments*, Rev. Sci. Instrum. **75**, 4001 (2004).
41. Y. Amemiya and J. Miyahara, *Imaging plate illuminates many fields*, Nature **336**, 89 (1988).
42. H. Ohuchi and A. Yamadera, *Dependence of fading patterns of photo-stimulated luminescence from imaging plates on radiation, energy, and image reader*, Nucl. Instrum. Methods Phys. Res. A **490**, 573 (2002).
43. A. L. Meadowcroft, C. D. Bentley, and E. N. Scott, *Evaluation of the sensitivity and fading characteristics of an image plate system for x-ray diagnostics*, Rev. Sci. Instrum. **79**, 113102 (2008).
44. B. R. Maddox, H. S. Park, B. A. Remington, N. Izumi, S. Chen, C. Chen, G. Kimminau, Z. Ali, M. J. Haugh, and A. Ma, *High-energy x-ray backlighter spectrum measurements using calibrated image plates*, Rev. Sci. Instrum. **82**, 023111 (2011).
45. P. K. Rambo, I. C. Smith, J. L. Porter, Jr., M. J. Hurst, C. S. Speas, R. G. Adams, A. J. Garcia, E. Dawson, B. D. Thurstron, C. Wakefield, J. W. Kellogg, M. J. Slattery, H. C. Ives III, R. S. Broyles, J. A. Caird, A. C. Erlandson, J. E. Murray, W. C. Behrendt, N. D. Neilsen, and J. M. Narduzzi, *Z-Beamlet: a multikilojoule, terawatt-class laser system*, Appl. Opt. **44**, 2421 (2005).

46. D. B. Sinars, D. F. Wenger, S. A. Pikuz, B. Jones, M. Geissel, S. B. Hansen, C. A. Coverdale, and M. E. Cuneo, *Compact, rugged in-chamber transmission spectrometers (7–28 keV) for the Sandia Z facility*, Rev. Sci. Instrum. **82**, 063113 (2011).
47. D. B. Sinars, M. E. Cuneo, G. R. Bennett, D. F. Wenger, L. E. Ruggles, M. F. Vargas, J. L. Porter, R. G. Adams, D. W. Johnson, K. L. Keller, P. K. Rambo, D. C. Rovang, H. Seamen, W. W. Simpson, I. C. Smith, and S. C. Speas, *Monochromatic x-ray backlighting of wire-array z-pinch plasmas using spherically bent quartz crystals*, Rev. Sci. Instrum. **74**, 2202 (2003).
48. D. B. Sinars, G. R. Bennett, D. F. Wenger, M. E. Cuneo, D. L. Hanson, J. L. Porter, R. G. Adams, P. K. Rambo, D. C. Rovang, and I. C. Smith, *Monochromatic x-ray imaging experiments on the Sandia National Laboratories Z facility (invited)*, Rev. Sci. Instrum **75**, 3672 (2004).
49. D. B. Sinars, D. F. Wenger, K. L. Keller, G. A. Rochau, and J. L. Porter, *Focusing, adjustable spectrometer with temporal resolution for the Sandia Z facility*, Rev. Sci. Instrum. **77**, 10F327 (2006).
50. G. R. Bennett, O. L. Landen, R. F. Adams, J. L. Porter, L. E. Ruggles, W. W. Simpson, and C. Wakefield, *2–20 ns interframe time 2-frame 6.151 keV x-ray imaging on the recently upgraded Z Accelerator: A progress report*, Rev. Sci. Instrum. **72**, 657 (2001).
51. B. G. Cour-Palais, *Hypervelocity Impact Investigations and Meteoroid Shielding Experience Related to Apollo and Skylab*, Orbital Debris Workshop, NASA CP-2360 (pp.247-275), Houston, August 27–29, 1982; B. G. Cour-Palais, *Hypervelocity impact in metals, glass and composites*, Int. J. Impact Engineering **5**, 221 (1999); B. G. Cour-Palais, *A career in applied physics: Apollo through space station*, Int. J. Impact Engineering **23**, 137 (1999).
52. K. S. Edelstein, *Hypervelocity impact damage tolerance of fused silica glass*, 43rd International Astronautical Federation, IAF-92-0334 (1992).
53. R. R. Burt and E. L. Christiansen, *Hypervelocity Impact Testing of Transparent Spacecraft Materials*, Int. J. Impact Engineering **29**, 153 (2003).
54. E. L. Christiansen and J. H. Kerr, *Ballistic limit equations for spacecraft shielding*, Int. J. Impact Engineering **26**, 93 (2001).
55. S. Ryan and E. L. Christiansen, *Micrometeoroid and Orbital Debris (MMOD) Shield Ballistic Limit Analysis Program*, NASA/TM-2009-214789, February 2010.
56. E. L. Christiansen, J. Arnold, B. Corsaro, A. Davis, F. Giovane, J. Hyde, D. Lear, J. C. Liou, F. Lyons, T. Prior, M. Ratliff, S. Ryan, G. Studor, *Handbook for Designing MMOD Protection*, NASA Johnson Space Center, NASA/TM-2009-214785 (2009).

DISTRIBUTION

1 University of Oxford
Attn: G. Gregori
Department of Physics
Clarendon Laboratory
Oxford, OX1 3PU, United Kingdom

5	MS1106	T. Ao	1646
1	MS1186	S. B. Hansen	1644
1	MS1189	M. P. Desjarlais	1640
1	MS1189	D. H. Dolan	1646
1	MS1189	M. Herrmann	1640
1	MS1189	D. G. Flicker	1646
1	MS1189	T. A. Haill	1641
1	MS1189	H. L. Hanshaw	1641
1	MS1189	R. W. Lemke	1641
1	MS1189	M. Martin	1641
1	MS1189	T. Mattsson	1641
1	MS1189	C. T. Seagle	1646
1	MS1189	L. Shulenburger	1641
1	MS1192	J. Reneker	1678
1	MS1193	M. Geissel	1672
1	MS1193	E. C. Harding	1648
1	MS1193	D. B. Sinars	1648
1	MS1193	I. C. Smith	1672
1	MS1195	C. S. Alexander	1646
1	MS1195	J. Brown	1646
1	MS1195	D. Dalton	1646
1	MS1195	J.-P. Davis	1646
1	MS1195	M. D. Furnish	1646
1	MS1195	M. D. Knudson	1646
1	MS1195	D. H. Romero	1646
1	MS1195	S. Root	1646
1	MS1195	J. L. Wise	1646
1	MS1196	G. A. Rochau	1675
5	MS1196	J. E. Bailey	1677

1	MS0899	Technical Library	9536 (electronic copy)
1	MS0359	D. Chavez, LDRD Office	1911

This page intentionally left blank.


Sandia National Laboratories